

©2017

MAOYUN LI

ALL RIGHTS RESERVED

PAVEMENT RESPONSE ANALYSIS AND MODULUS BACK-CALCULATION  
FOR HIGHWAY AND AIRFIELD FLEXIBLE PAVEMENTS

By

MAOYUN LI

A dissertation submitted to the

School of Graduate Studies

Rutgers, The State University of New Jersey

In partial fulfillment of the requirements

For the degree of

Doctor of Philosophy

Graduate Program in Civil and Environmental Engineering

Written under the direction of

Dr. Hao Wang

And approved by

---

---

---

---

New Brunswick, New Jersey

October, 2017

# **ABSTRACT OF THE DISSERTATION**

Pavement Response Analysis and Modulus Back-Calculation for Highway and Airfield

Flexible Pavements

by MAOYUN LI

Dissertation Director:

Dr. Hao Wang

The analysis of pavement responses is important for better understanding of pavement performance and accurate estimation of pavement service life. This dissertation aims to study flexible pavement responses using forward and inverse analysis. The first objective is development of axisymmetric finite element (FE) models that can simulate FWD loading on the pavement system. After that, the backcalculation of pavement layer moduli from FWD testing was studied by means of soft computing techniques such as Artificial Neural Networks (ANNs) and Genetic Algorithms (GA). The axisymmetric FE models were used to generate a synthetic database. The ANN-GA backcalculating program is developed to assess existing pavement condition after the training and verification using the synthetic database. The second objective of this dissertation is to investigate airfield flexible pavement responses under aircraft loading in consideration of the realistic aircraft tire-pavement interaction. An advanced three-dimensional (3-D) finite element (FE) model was developed to simulate heavy aircraft loading with high tire pressure. The aircraft loading was simulated as moving wheels having non-uniform

contact stress distributions. Different tire rolling conditions caused by aircraft ground maneuvering were simulated, including free rolling, full-braking, and turning. The multi-wheel aircraft loading was modeled in two-wheel, four-wheel and six-wheel assembly..

The analysis concludes that FWD deflections were affected by dynamic analysis, temperature gradient, bedrock depth, asphalt layer delamination, viscoelasticity, and unbound material nonlinearity. After validated with the field measurements in the long-term pavement performance program (LTPP) database, the developed ANN-GA program can be used to obtain damaged dynamic moduli of asphalt concrete and evaluate in-situ pavement conditions from structural point of view, which facilitates pavement overlay design procedure using Mechanistic-Empirical Pavement Design Guideline (MEPDG).

The investigation on airfield flexible pavement emphasized the importance of considering non-uniform tire contact stresses and temperature profiles in airfield pavement analysis. For the aircraft ground maneuvering, aircraft braking or turning significantly increases shear failure potential in asphalt layer. The analysis of stress states would facilitate evaluation of the shear failure potential at airfield asphalt pavements. Finally, the investigation on multi-wheel aircraft loading indicates that the six-wheel gear configuration would cause more fatigue cracking and near-surface cracking potential than dual-wheel and four-wheel gears.

## **DEDICATION**

*To My Family, I Love You.*

## **ACKNOWLEDGEMENT**

I would like to start by expressing my most sincere gratitude to my advisor, Dr. Hao Wang, for his continual guidance and support throughout my entire Ph.D. study and at Rutgers, The State University of New Jersey. I am inspired by his high standard and great wisdom in his expertise area. My achievement would be nothing without him as a role model to work with. It is truly an honor to have him as my Ph.D. advisor.

It is my great honor and privilege to have Dr. Nenad Gucunski, Dr. Husam Najm, and Dr. Navneet Garg as the members of my graduate committee. Their encouragements and valuable suggestions during my Ph.D. study go far beyond the completion of my dissertation and defense.

A special gratitude is made hereby to National Airport Pavement Test Facility (NAPTF) of Federal Aviation Administration (FAA) for their support to this study. I would also like to thank the help and support from Mr. Jeffrey Gagnon, Mr. Albert Larkin, Dr. David Brill, and Dr. Richard Ji from NAPTF and Dr. Qiang Li from CSRA International, Inc.

Great appreciation is also made to Dr. Zilong Wang for his help, assistance, and guidance as well as encouragement and friendship throughout my Ph.D. study at Rutgers. I would also like to express my appreciation to the CEE departmental staff: Gina Cullari and Linda Szary and all the members in Dr. Hao Wang's group.

Finally, I am deeply indebted to my family for their endless patience, comprehension, and love, and especially acknowledge the selfless support and encouragement of my Mother, Zaoying Li.

## TABLE OF CONTENTS

<b>ABSTRACT OF THE DISSERTATION .....</b>	<b>ii</b>
<b>DEDICATION.....</b>	<b>iv</b>
<b>ACKNOWLEDGEMENT.....</b>	<b>v</b>
<b>LIST OF FIGURES .....</b>	<b>xi</b>
<b>LIST OF TABLES .....</b>	<b>xvi</b>
<b>CHAPTER 1 INTRODUCTION .....</b>	<b>1</b>
<b>1.1 Introduction.....</b>	<b>1</b>
<b>1.2 Problem Statement.....</b>	<b>2</b>
<b>1.3 Objective and Methodology .....</b>	<b>4</b>
<b>CHAPTER 2 LITERATURE REVIEW .....</b>	<b>6</b>
<b>2.1 Pavement Evaluation with Falling Weight Deflectometer .....</b>	<b>6</b>
<i>2.1.1 Pavement Analysis Using Falling Weight Deflectometer .....</i>	<i>6</i>
<i>2.1.2 Relationship between FWD and Moving Loading .....</i>	<i>7</i>
<b>2.2 Backcalculation of Pavement Layer Modulus.....</b>	<b>9</b>
<i>2.2.1 Iteration-based Approach .....</i>	<i>9</i>
<i>2.2.2 Limitations of Iteration-Based Approach .....</i>	<i>10</i>
<i>2.2.3 Soft Computing Approach.....</i>	<i>11</i>
<i>2.2.4 Backcalculation with Soft Computing Approach .....</i>	<i>12</i>
<b>2.3 Airfield Pavement Design and Analysis.....</b>	<b>14</b>
<i>2.3.1 FAA Rigid and Flexible Iterative Elastic Layered Design (FAARFIELD)..</i>	<i>14</i>
<i>2.3.2 Airfield Pavement Studies at NAPTF.....</i>	<i>15</i>
<i>2.3.3 Boeing and FAA High Tire Pressure Test .....</i>	<i>17</i>
<i>2.3.4 Airbus High Tire Pressure Test .....</i>	<i>18</i>
<b>2.4 Summary.....</b>	<b>19</b>
<b>CHAPTER 3 FINITE ELEMENT MODELING OF FLEXIBLE PAVEMENT</b>	
<b>UNDER FWD LOADING .....</b>	<b>21</b>
<b>3.1 Material Constitutive Models and Analysis Type.....</b>	<b>21</b>
<i>3.1.1 Viscoelastic Model of Asphalt Concrete .....</i>	<i>21</i>
<i>3.1.2 Nonlinear Cross-Anisotropic Model of Unbound Material.....</i>	<i>22</i>

3.1.3 Nonlinear Solving Technique.....	24
3.1.4 Quasi-Static and Dynamic Analysis.....	25
3.1.5 Temperature Distribution .....	26
3.1.6 Interface Modeling.....	27
<b>3.2 Development of Axisymmetric FE Model.....</b>	<b>27</b>
3.2.1 Pavement Structure and Material Parameters .....	27
3.2.2 FE Model Meshes and Boundary Conditions .....	28
3.2.3 Validation with Surface Deflections .....	32
<b>3.3 Parametric Analysis and Results.....</b>	<b>34</b>
3.3.1 Analysis Parameters .....	34
3.3.2 Effect of Dynamic Analysis .....	35
3.3.3 Effect of HMA Viscoelasticity .....	37
3.3.4 Effect of Temperature Gradient .....	39
3.3.5 Effect of Asphalt Layer Delamination.....	41
3.3.6 Effect of Unbound Material Nonlinearity .....	44
3.3.7 Effect of Bedrock Depth.....	47
<b>3.4 Summary.....</b>	<b>48</b>
<b>CHAPTER 4 BACKCALCULATION OF PAVEMENT MODULI USING AN</b>	
<b>ANN-GA MODEL .....</b>	<b>50</b>
<b>4.1 Backcalculation of Pavement Layer Properties .....</b>	<b>50</b>
4.1.1 Overview of The Soft Computing-based Process.....	50
4.1.2 Development of Synthetic Deflection Database.....	51
<b>4.2 Development of ANN-GA Program .....</b>	<b>52</b>
4.2.1 Overview of ANN Architecture .....	52
4.2.2 Outline of Genetic Algorithm Process .....	55
<b>4.3 Training and Verification of ANN-GA Program.....</b>	<b>58</b>
<b>4.4 Validation of ANN-GA Program using Field Testing Data .....</b>	<b>61</b>
4.4.1 Field Testing Sections for Validation .....	61
4.4.2 Validation of Backcalculation Results .....	62
<b>4.5 Assessment of Asphalt Material Deterioration .....</b>	<b>65</b>
4.5.1 Field Sections from LTPP Database.....	65



4.5.2 ANN-GA Program for Evaluation of AC Material Deterioration .....	67
4.5.3 Extensive Validation of ANN-GA Program .....	68
4.5.4 Backcalculation of Damaged Dynamic Modulus .....	72
4.5.5 Comparison with Damaged Modulus Model in MEPDG .....	74
4.5.6 Comparison with LTPP Field Distress Data .....	77
<b>4.6 Assessment of Unbound Material Degradation .....</b>	<b>79</b>
4.6.1 Unbound Material Properties at Field Sections .....	79
4.6.2 Validation of ANN-GA Program for Unbound Material Properties .....	81
4.6.3 Damage in Unbound Material Properties Modulus .....	83
<b>4.7 Summary.....</b>	<b>85</b>
<b>CHAPTER 5 AIRPORT PAVEMENT RESPONSES UNDER HIGH TIRE</b>	
<b>PRESSURE AND AIRCRAFT GROUND MANOVERTING .....</b>	<b>87</b>
<b>5.1 Accelerated Pavement Testing at NAPTF .....</b>	<b>87</b>
5.1.1 Indoor Heated Pavement Sections .....	87
5.1.2 HVS Test Sections .....	90
<b>5.2 Aircraft Tire Contact Stresses .....</b>	<b>96</b>
5.2.1 Tire Contact Stress at Free Rolling Condition .....	96
5.2.2 Tire Contact Stresses at Maneuvering Conditions .....	97
<b>5.3 Development of FE Model for Airfield Pavement .....</b>	<b>101</b>
5.3.1 Material Properties.....	101
5.3.2 Material Parameters of Unbound Layers .....	103
5.3.3 FE Model Meshes and Bounday Conditions.....	104
<b>5.4 Analysis of Pavement Responses with Heated Pavement Sections.....</b>	<b>107</b>
5.4.1 Effect of Tire-Pavement Contact Stresses.....	107
5.4.2 Comparison between Moving and Stationary Loading .....	110
5.4.3 Effect of Temperature Profile .....	112
5.4.4 Effect of Tire Load and Inflation Pressure .....	113
<b>5.5 Analysis of Pavement Responses at HVS Sections.....</b>	<b>114</b>
5.5.1 Effect of High Tire Pressure .....	114
5.5.2 Effect of Non-Linear Behavior of Granular Base.....	115
5.5.3 Comparison between Measured and Calculated Pavement Responses.....	117

<b>5.6 Effect of High Aircraft Tire Pressure on Rutting .....</b>	<b>119</b>
5.6.1 Pavement Rutting Prediction Models .....	119
5.6.2 Calculation of Rutting Depth .....	121
<b>5.7 Failure Criteria for Multi-Axial Stress .....</b>	<b>123</b>
<b>5.8 Effect of Aircraft Maneuvering on Pavement Near-Surface Failure.....</b>	<b>126</b>
5.8.1 Effect of Aircraft Maneuvering on Near-Surface Responses .....	126
5.8.2 Effect of Aircraft Loading on Interface Responses .....	130
5.8.3 Effect of Aircraft Loading on Critical Stress Ratios .....	135
<b>5.9 Summary.....</b>	<b>136</b>
<b>CHAPTER 6 AIRFIELD PAVEMENT RESPONSES UNDER MULTI-WHEEL</b>	
<b>GEAR LOADING .....</b>	<b>139</b>
<b>6.1 Full-Scale Pavement Testing.....</b>	<b>139</b>
6.1.1 Test Sections and Loading Conditions.....	139
6.1.2 H-bar Strain Gauge Responses.....	141
<b>6.2 Multi-Wheel Loading Simulation and Response Analysis .....</b>	<b>142</b>
6.2.1 FE Model Validation for Multi-Wheel Loading.....	142
6.2.2 Multi-Wheel Loading Effect on Fatigue Cracking Potential .....	145
6.2.3 Multi-Wheel Loading Effect on Near-Surface Cracking Potential.....	148
6.2.4 Effect of Loading Magnitude .....	151
6.2.5 Effect of Wheel Speed.....	152
<b>6.3 Fatigue Life Analysis .....</b>	<b>153</b>
6.3.1 Fatigue Models .....	153
6.3.2 Comparison of Calculated Fatigue Life .....	155
<b>6.4 Summary.....</b>	<b>158</b>
<b>CHAPTER 7 CONCLUSIONS AND RECOMMENDATIONS .....</b>	<b>160</b>
<b>7.1 Conclusions.....</b>	<b>160</b>
7.1.1 Finite Element Modeling.....	160
7.1.2 ANN-GA Program for Backcalculation .....	161
7.1.3 Aircraft High Tire Pressure .....	162
7.1.4 Aircraft Ground Maneuvering .....	162
7.1.5 Aircraft Multi-Wheel Loading.....	163

<b>7.2 Recommendations for Future Study .....</b>	<b>163</b>
<b>REFERENCES.....</b>	<b>165</b>

## LIST OF FIGURES

Figure 2.1 Flowchart of modulus backcalculation based on iterative procedure .....	10
Figure 3.1 Thin flexible pavement structure with material properties of different layers	28
Figure 3.2 FE model layout in axisymmetric 2-D domain with infinite boundary and loading area .....	30
Figure 3.3 Sensitivity analysis for (a) central deflection vs. radial length of finite domain; (b) edge deflection vs. radial length of finite domain; (c) central deflection vs. depth of finite domain; and (d) edge deflection vs. depth of finite domain .....	31
Figure 3.4 Validation of FE models with measurements under FWD loading.....	33
Figure 3.5 Validation of FE model with measurement under FWD loading of (a) 53kN; (b) 40kN; and (c) 27kN .....	34
Figure 3.6 Dynamic analysis vs. quasi-static analysis through (a) deflection-time histories; (b) strain-time histories; (c) D0 hysteresis loops; and (d) D900 hysteresis loops .....	37
Figure 3.7 HMA viscoelasticity vs. elasticity through (a) deflection-time histories; (b) strain-time histories; (c) D0 hysteresis loops; and (d) D900 hysteresis loops .....	39
Figure 3.8 Effect of temperature gradient on (a) deflection-time histories at the intermediate temperature; (b) strain-time histories at the intermediate temperature; and (c) deflection-time histories at the high temperature; and (d) strain-time histories at the high temperature.....	41
Figure 3.9 Effects of layer delamination on (a) D0-time history; (b) D900-time history; (c) tensile strain-time history; (d) compressive strain-time history; (e) hysteresis loop of D0; and (f) hysteresis loop of D900.....	43
Figure 3.10 Effect of nonlinear model of aggregate base on (a) D0 and D900; (b) critical strains; (c) hysteresis loop of D0; and (d) hysteresis loop of D900.....	45
Figure 3.11 Effect of nonlinear model of subgrade on (a) D0 and D900; (b) critical strains; (c) hysteresis loop of D0; and (d) hysteresis loop of D900 .....	46
Figure 3.12 FWD deflection variations under multiple loadings considering nonlinear unbound material for (a) D0 and (b) D900 .....	47

Figure 3.13 Effects of bedrock on FWD deflections for (a) D0-time history; (b) D900-time history; (c) sensitivity of D0 to the depth to bedrock; and (d) sensitivity of D900 to the depth to bedrock.....	48
Figure 4.1 Layered structure of feed-forward ANN model .....	54
Figure 4.2 (a) Flowchart of ANN-GA program and (b) GA operators.....	57
Figure 4.3 Illustration of hysteresis loop (load-displacement curve): (a) FWD load and displacement; and (b) three shape indicators .....	59
Figure 4.4 Comparison of outputs ANN-GAA program to synthetic database inputs for (a) sigmoidal curve parameters (21°C); (b) WFL shift factors of asphalt layer; (c) base layer material parameters; and (d) subgrade material parameters .....	61
Figure 4.5 Comparison of outputs from ANN-GA program with measured data from LTPP database by (a) dynamic moduli and (b) WLF function parameters for time-temperature shift factor .....	63
Figure 4.6 Comparison of measured and calculated deflections using the backcalculated material parameters for LTPP sections .....	65
Figure 4.7 FWD deflections in hysteresis loop from LTPP program database .....	67
Figure 4.8 Flowchart of ANN-GA program predicting existing AC moduli .....	68
Figure 4.9 Comparison between LTPP testing and ANN-GA results in: (a) synchronically predicted dynamic moduli; (b) independently predicted dynamic moduli; (c) synchronically predicted WLF shift factor; and (d) independently predicted WLF shift factor .....	70
Figure 4.10 Accuracy of backcalculated dynamic moduli at different frequencies for all sections.....	71
Figure 4.11 FWD hysteresis loops in different stages of pavement life .....	72
Figure 4.12 Compared dynamic moduli in different phases of AC deterioration by ANN-GA program for: (a) 27-1018; (b) 27-6251; (c) 35-1112; and (d) 87-1622.....	74
Figure 4.13 Dynamic moduli in different phases of AC deterioration by MEPDG approach for LTPP section (a) 27-1018; (b) 27-6251; (c) 35-1112; and (d) 87-1622 .....	77
Figure 4.14 Correlation between pavement distresses and damage levels in AC for (a) 27-1018; (b) 27-6251; and (c) 87-1622.....	78

Figure 4.15 Comparison between LTPP testing and ANN-GA backcalculated base aggregate parameters: (a) $k_1$ ; (b) $k_2$ ; and (c) $k_3$ .....	82
Figure 4.16 Comparison between LTPP testing and ANN-GA backcalculated subgrade soil parameters: (a) $k_1$ ; (b) $k_2$ ; and (c) $k_3$ .....	83
Figure 5.1 Modeled pavement: (a) cross-section; (b) two temperature profiles in FE modeling and (c) dynamic modulus curve.....	88
Figure 5.2 Distributions of tire-pavement vertical contact stresses .....	89
Figure 5.3 Rutting depth measured at the indoor heated pavement section .....	90
Figure 5.4 NAPTF (a) Heavy Vehicle Simulator-Airport Version (HVS-A) and (b) pavement instrumentation .....	91
Figure 5.5 Measured (a) longitudinal and (b) transverse strains under different loading Levels .....	94
Figure 5.6 Rutting depth measured under two different pressure levels .....	95
Figure 5.7 Contact stress assumptions of (a) non-uniform, (b) area-based uniform, and (c) pressure-based uniform .....	97
Figure 5.8 Illustration of tire-pavement contact stresses for (a) free rolling; (b) full braking; and (c) turning .....	101
Figure 5.9 Master curve of dynamic modulus at 20°C for (a) PG 64-22 and (b) PG76-22 asphalt mixture.....	103
Figure 5.10 Schematic illustration of FE model layout: (a) 3-D finite with infinite domain and (b) cross-section of trafficking direction.....	105
Figure 5.11 Sensitivity analyses for (a) transverse tensile strain vs. finite domain length; (b) transverse tensile strain vs. finite domain width; (c) longitudinal tensile strain vs. finite domain length; (d) longitudinal tensile strain vs. finite domain width; (e) shear strain vs. finite domain length and (f) shear strain vs. finite domain width .....	106
Figure 5.12 Effect of contact stress patterns on (a) in-depth distribution of compressive strain, (b) in-depth distribution of shear strain, and (c) transverse distribution of transverse tensile strain at the bottom of HMA layer .....	108
Figure 5.13 Vertical modulus distributions (unit: MPa) in base layer using nonlinear anisotropic model at (a) 133kN and (b) 222kN .....	116
Figure 5.14 Calculated tensile strains from FE model.....	118

Figure 5.15 Comparison of tensile strains from Accelerated Pavement Testing and Numerical Modeling using (a) Linear and (b) Non-linear Model for Granular Base	119
Figure 5.16 Comparison of rutting depth increase at high tire pressure for the indoor heated pavement section .....	122
Figure 5.17 Rutting depths from simulation for the HVS test section.....	123
Figure 5.18 Representations of Mohr-Coulomb failure criterion in (a) Mohr's circles and (b) p-q diagram .....	125
Figure 5.19 Temperature profile in the modeled pavement under aircraft maneuvering	127
Figure 5.20 In-depth distributions of maximum shear stresses (a) at transverse direction and (b) along traffic direction .....	128
Figure 5.21 Stress states at pavement near-surface under (a) V-Loading; (b) 3D-Loading; (c) FB-Loading; and (d) THE-Loading.....	130
Figure 5.22 Distributions of (a) transverse shear stress; (b) longitudinal shear stress; and (c) normal stress at the interface along tire contact width .....	132
Figure 5.23 Critical stress paths at interface under (a) V-Loading; (b) 3D-Loading; (c) FB-Loading; and (d) THE-Loading .....	134
Figure 6.1 Accelerated Pavement Testing information: (a) pavement cross-sections and (b) aircraft gear configurations .....	140
Figure 6.2 Pavement instrumentation: (a) layout and (b) protection of asphalt strain gauges .....	141
Figure 6.3 Response testing results from strain gauge at 36-kip loading: (a) LFP-1N under 2-wheel gear configuration; (b) LFP-3N under 2-wheel gear configuration; (c) LFP-1N under 6-wheel gear configuration; and (d) LFP-3N under 6-wheel gear configuration .....	142
Figure 6.4 Illustration of FE model for (a) pavement structure with moving loading pattern; and (b) compressive stresses on pavement surface under six-wheel loading .....	143
Figure 6.5 Validation of FE models with response testing results by 36-kip aircraft loading: (a) LFP-1N under 2-wheel gear configuration; (b) LFP-3N under 2-wheel gear configuration; (c) LFP-1N under 6-wheel gear configuration; and (d) LFP-3N under 6-wheel gear configuration .....	144

Figure 6.6 Validation results for critical tensile strains from 3-D FE models .....	145
Figure 6.7 Time histories of tensile strains at the bottom of asphalt layer: (a) transverse strains in LFP-1N and (b) longitudinal strains in LFP-1N; (c) transverse strains in LFP-3N; and (d) longitudinal strains in LFP-3N .....	147
Figure 6.8 Transverse distributions of tensile strains in LFP-3N: (a) transverse strains and (b) longitudinal strains .....	148
Figure 6.9 Time histories of near-surface shear strains: (a) transverse strains in LFP-1N and (b) longitudinal strains in LFP-1N; (c) transverse strains in LFP-3N; and (d) longitudinal strains in LFP-3N.....	150
Figure 6.10 In-depth distribution of near-surface shear strains in LFP-3N: (a) transverse strains; and (b) longitudinal strains .....	151
Figure 6.11 Effect of loading level on strain responses in asphalt layer: (a) critical tensile strains and (b) critical shear strains.....	152
Figure 6.12 Time histories of critical (a) tensile strains at the bottom of asphalt layer and (b) shear strains at pavement near-surface at different moving speeds .....	153
Figure 6.13 Hysteresis loops for the tensile strains under multi-wheel loading for the section of LFP-3N.....	156



## LIST OF TABLES

Table 4.1 Matrix of Input Variables for the FWD Synthetic Database .....	52
Table 4.2 LTPP On-site Testing Pavement Layer Thickness .....	66
Table 4.3 LTPP On-site Testing Pavement Section Information .....	80
Table 4.4 Unbound Material Parameters for LTPP Sections.....	80
Table 4.5 Degraded Base Material Parameters Backcalculated by ANN-GA Program...	84
Table 4.6 Degraded Subgrade Material Parameters Backcalculated by ANN-GA Program .....	85
Table 5.1 Prony Series and Shift factors for the HMA material.....	89
Table 5.2 Contact Stress Distributions and Contact Areas (Tire load: 234kN).....	97
Table 5.3 Comparison of Critical Pavement Responses under Different Contact Stress Patterns (Tire load 234kN; Tire pressure 1.45MPa).....	109
Table 5.4 (a) In-depth Pulse Time from MEPDG and FE Methods .....	111
Table 5.4 (b) Comparison of Pavement Responses under Moving and Stationary Loading (Tire load 234kN; Tire pressure 1.45MPa).....	112
Table 5.5 Comparisons of Pavement Responses with Different Temperature Profiles..	113
Table 5.6 Comparisons of Critical Pavement Responses under Different Tire Loads and Pressure Levels .....	114
Table 5.7 Comparison of Critical Pavement Responses under Different Tire Loads and Pressure .....	115
Table 5.8 Comparison of Pavement Responses Using Different Models for Aggregate Base Layer .....	117
Table 5.9 Critical Shear Stresses and Stress Ratios at Different Aircraft Loading Conditions .....	136
Table 6.1 Comparison of Critical Input Variables for Fatigue Life .....	156
Table 6.2 Performance Comparison of Calculated Fatigue Life .....	157
Table 6.3 Percentage Change of Calculated Fatigue Life.....	158

## **CHAPTER 1 INTRODUCTION**

### **1.1 Introduction**

Flexible pavement responses under moving tire loading have been investigated intensively in recent years for long-lasting pavement design. The major factors affecting pavement responses and long-term performance include pavement structure, layer material properties, vehicular or aircraft loading, and environmental conditions. For a typical flexible pavement structure, the asphalt layer is to provide structural support and as well as smooth and skid-resistance surface. The unbound material base layer is primarily utilized for purposes of providing support to surface layer, distributing wheel loading, drainage, etc.

With the current trend toward mechanistic pavement design method and the need for more reliable overlay design procedures, the accurate assessment of in-situ pavement condition is critical. The Falling Weight Deflectometer (FWD) has been used as an effective non-destructive testing (NDT) device to evaluate existing pavement condition in a quick manner. The FWD loading system delivers a transient impulse load to the pavement surface and the resulted surface deflections are measured at different offsets. Therefore, the pavement surface deflections measured during FWD testing can be used to evaluate structural capacity and back-calculation of layer modulus.

Accelerated pavement testing (APT) provides an acceptable solution between real field pavement loading and laboratory tests to evaluate the loading and design parameters on pavement damage. During the APT, pavement responses to loading can be measured using pavement instrumentation. The parameters that can be measured include strains, stresses, deflections, moisture, temperature, etc. In-situ measurements of pavement responses allow for understanding the key factor affecting pavement responses and developing accurate performance models for mechanistic-empirical pavement design approaches.

Numerical modeling has become a powerful tool to simulate pavement responses under different loading scenarios. The appropriate utilization of numerical modeling

could reduce the significant efforts that are required for construction of full-scale pavement sections and pavement instrumentation. After the numerical model is calibrated and validated, the computational environment would enable to consider different combinations of material properties, structure designs, loading configurations, and environmental conditions. The numerical modeling results can be also used to check the reliability and accuracy of measurements and predict pavement responses that are difficult to measure in the field. Modeling analysis of pavement can be either based on the multilayer elastic theory (MLE) or finite element model (FEM). The FEM approach is more powerful for pavement analysis because it could simulate realistic tire-pavement interaction and complex material behavior of each pavement layer.

Soft computing techniques, compared to hard computing ones, accommodate tolerance of imprecise solution to nondeterministic polynomial time-complete problems. Machine Learning and Evolutionary Algorithm serve as the typical Artificial Intelligence, one of Soft computing techniques, which otherwise differentiate from numerical analysis and binary logic hard computing. It introduces Artificial Neural Networks (ANNs) and Genetic Algorithms (GAs) whereby pavement community has investigated and applied for decades. ANNs were emphasized mainly due to three merits over traditional backcalculation such as less error, high efficiency, and output uniqueness. To enhance the capability of soft computing for FWD backcalculation, GAs can be applied as an optimization tool to facilitate ANN programs to efficiently optimize solutions.

## **1.2 Problem Statement**

FWD serves as an essential nondestructive tool to obtain pavement layer moduli and structural capacity. Currently available procedures for the analysis of FWD deflection data mainly focus on back-calculation of layer modulus and assessment of in-situ pavement condition from deflection basin parameters. However, it was believed that variations in dynamic analysis approaches, non-uniform temperature profiles, viscoelastic and nonlinear material properties, and interface conditions can lead to analysis

uncertainties of calculating FWD deflections using analytical pavement models. Therefore, more realistic mechanistic models are needed to more accurately capture the pavement behaviors under FWD loading.

Conventional backcalculating procedures were mainly grouped as static and dynamic ones. The static one makes use of merely the peak values of FWD deflections to backcalculate the linear elastic modulus for each layer (Huang 1993). The key portion of static backcalculation relies on iterative procedure with seed layer moduli. The iterative procedure in nature delivers trial and error algorithm to repeatedly comparing calculated and measured deflections. Backcalculating programs such as BISAR and EVERCALC have been developed and employed in the pavement sections of Minnesota testing (Mateos and Snyder 2002). Dynamic procedure otherwise considers the full time histories of FWD deflections related to complex moduli in time/frequency domain. Therefore, the complex moduli were processed in a forward procedure to iteratively search for the best matched FWD deflections in fitted frequency domain or time domain (Uzan 1994). Limitations were found for the conventional FWD backcalculation of accuracy instability, computational inefficiency, and result non-uniqueness.

Traditional pavement analysis usually assumed that the contact stresses at the tire-pavement interface was equal to the inflation pressure and was uniformly distributed in a circular or rectangular contact area. However, this assumption was not consistent with the realistic tire loading condition because field measurements have clearly shown that the vertical contact pressure at the tire-pavement interface should be non-uniformly distributed depending on tire load, inflation pressure, and rolling condition (Howell et al. 1986; Tielking 1989; Daugherty 2003; Rolland 2009). It has been found that the discrepancy between the uniform and non-uniform distribution of tire-pavement contact stresses was enlarged when the applied tire inflation pressure was increased. Compared to heavy-weight truck, aircraft tires actually carry much greater wheel loads with the higher tire inflation pressure. Accordingly, highly potential rutting distress was caused with the increase of the wheel-loading stresses. And the near-surface shear failure can also be raised as a typical distress in the thick flexible pavement as served in airport.

Airfield pavements are experiencing heavy aircraft tire loading. As the new generation of aircraft becomes larger and heavier, aircraft manufacturers intend to increase tire pressure in order to increase pay load or add more wheels in order to keep the load limited on the individual wheel. Therefore, it is important to understand if high tire pressure or more wheels can cause accelerated pavement failure.

On the other hand, frequent aircraft ground maneuvering operations in the movement area of airport, such as taxiing, braking during landing, acceleration during takeoff, and turning between runways and taxiways. It is expected that these maneuvering operations could cause high shear stresses at the pavement near-surface, particularly in high-speed taxiway and in areas of push-back operations with lateral wheel slip. A slippage failure in the Newark Liberty International Airport runway was observed at the interface of the first and second layer of asphalt in the keel section approaching high-speed taxiway (Bognacki et al. 2007; Cook et al. 2016). Runway distresses such as shoving and tearing were evidently observed at the landing areas as well as high-speed exit taxiway in an investigation of before pavement rehabilitation at the Houston George Bush International Airport (Jones et al. 2013; Wang et al. 2017).

### **1.3 Objective and Methodology**

The study aims to conduct forward and inverse analysis of pavement responses for highway and airfield pavements. Finite element (FE) models was developed and validated that can predict pavement response under the impulsive FWD loading and moving tire loading. Soft computing technique combining ANNs and GAs was developed to backcalculate pavement layer properties. The effect of aircraft loading condition and perpetual pavement design in the airfield are investigated using FE simulation results as compared to instrumentation measurements at the National Airport Pavement Testing Facility (NAPTF).

The following analysis tasks are conducted to achieve the study objective:

- 1) Develop and validate FE models for simulation of FWD testing and build synthetic database of pavement responses for various pavement materials and structures.
- 2) Develop an ANN-GA model to backcalculate layer moduli of flexible pavement using surface deflections of FWD testing, respectively, for viscoelastic parameters of asphalt concrete and nonlinear parameters of unbound materials.
- 3) Develop and validate FE models to simulate flexible pavement responses under aircraft loading and investigate the effects of high tire pressure and ground maneuvering operations on airfield pavement responses.
- 4) Investigate in-depth strain distributions in the flexible pavement and evaluate perpetual pavement design criteria for airfield pavements using simulation data from FE models and experimental data from the NAPTF.

## CHAPTER 2 LITERATURE REVIEW

### 2.1 Pavement Evaluation with Falling Weight Deflectometer

#### 2.1.1 Pavement Analysis Using Falling Weight Deflectometer

The FWD is designed to impart a load pulse to the pavement surface by dropping a large weight, which is transmitted to pavement surface through a circular load plate 300 mm in diameter. A load cell mounted on top of the load plate measures the load imparted to the pavement surface. Typically, the load for road testing ranges from 40 to 71kN for FWD, and 53 to 160kN for Heavy Weight Deflectometer (HWD), delivering variations of pressures under the load plates. The measured deflections from FWD testing can indicate the structural capacity of in-service pavement structure; and can be further used to evaluate the remaining service life of pavement based on empirical or mechanistic-empirical method.

Many studies are conducted on the simulation of FWD to interpret its mechanism and investigate affecting factors on the backcalculation. The dynamic analysis approach was incorporated into the viscoelastic Hot Mix Asphalt (HMA) layer to simulate the FWD deflections as well as wave propagation by means of varying temperatures and load frequencies (Al-Qadi et al. 2010; Xu and Prozzi 2013; Chen et al. 2016; Li et al. 2017). The simulation results along with the dynamic analysis were shown in better matching the field FWD measurements as compared to non-dynamic analysis or elastic HMA layer. The dynamic behavior of FWD can be magnified with the existence of bedrock as a rigid layer underlying the subgrade (Mera 1995; Broutin 2010). The correlation of asphalt concrete (AC) layer moduli to the temperatures along different layer depth was studied (Salem et al. 2004). The result indicated that the mid-depth temperature can be considered representing the in-depth distributed temperature for the prediction of elastic HMA modulus from Long-Term Pavement Performance (LTPP) database. An investigation on several newly constructed asphalt pavements was implemented to signify the debonded behavior of the HMA interlayer in the backcalculating process (Hakim et al. 2000). The FWD testing results were also found affected by the base layer and

subgrade underneath the HMA layer. It was reported that removing nonlinear of linear unbound material properties incurring substantial errors in calculating the responses of flexible pavement (Schwartz 2002).

Deflection basin parameters (DBPs), which are derived from FWD deflection measurements, are established to indicate layer properties and pavement conditions. The most widely used and effective DBPs were identified: AREA, area under pavement profile (AUPP), surface curvature index (SCI), base curvature index (BCI), and base damage index (BDI). Connections between selected DBPs and critical responses as well as layer moduli have been developed by many researchers, and acceptable agreement with measured data was achieved to validate the proposed condition indicators and predictive models. Xu et al. (2002) developed an assessment program to analyze the relationship between the FWD deflections and pavement structure and temperature. A correction was carried out on the predictive models to better estimate the pavement conditions. Park et al. (2005) produced a simplified program to assess the flexible pavement conditions by means of multi-load FWD deflections. In this study, the DBPs were used as indicators to calculate critical responses under pavement surface for each layer. Losa et al. (2008) has proposed a statistics-based model to directly evaluate the critical strains in use of FWD deflections. It showed a helpful method of assessing the remaining service life in pavement.

### *2.1.2 Relationship between FWD and Moving Loading*

The FWD loading is a stationary dynamic loading that is different from the moving loading caused by rolling tires. The discrepancies caused by stationary and moving loading patterns could be present in loading periods (pulse durations) and magnitudes of pavement responses (stress, strain, and deflection). The pulse duration under FWD loading was generally accepted as constant of 0.033sec, but loading duration under truck was found as a function of pavement depth and vehicular velocity through filed testing (Loulizi et al. 2002). Moreover, critical responses induced by FWD loading were found well related to the ones by truck loading (Qin 2010; Leiva-Villacorta and Timm 2013; Wang



and Li 2016). What is more important is that asphalt pavement responses under moving loading vary at different locations, speeds, and temperatures. Thus, it is highly necessary to study the loading equivalency between FWD and moving vehicular loading in terms of pavement responses along with stress pulse durations.

Although it is usually assumed that FWD testing simulates truck loading at high speeds, it is not clear if the stationary impulse loading applied during FWD test can induce pavement responses that are equivalent to traffic loading at typical highway speeds. The FWD loading is a stationary dynamic loading that is different from the moving loading caused by rolling tires. The discrepancies caused by stationary and moving loading patterns could be present in loading periods (pulse durations) and magnitudes of pavement responses (stress, strain, and deflection).

A number of studies have been conducted to measure the pulse durations under traffic loading and compare the pulse durations under FWD and moving vehicular loading. The moving loading duration was found as a function of pavement depth and vehicular velocity from the truck testing on Virginia Smart Road (Loulizi et al. 2002). Recently, the analysis based on the Mechanistic-Empirical Pavement Design (MEPDG) found that the traffic loading duration in the asphalt pavement is influenced by the moduli ratio between the neighbor layers and the loading wave shape in addition to vehicle speeds and the depth below pavement surface (Hu et al. 2010). Furthermore, the transverse tensile strains were found more responsible for the fatigue cracking compared to longitudinal ones in terms of the magnitude and pulse duration (Garcia and Thompson 2008).

Another study conducted in Ohio test track found that the critical tensile strains under FWD loading, compared to other velocities, behaved much closer to the ones produced by moving loading at the speed around 55 mph (Qin 2010). Testing program conducted at the National Center for Asphalt Technology (NCAT) found that FWD equivalent velocities above 120 mph to the moving truck loading were investigated based on the pulse duration of compressive stress at the bottom of asphalt layer (Leiva-Villacorta and Timm 2013). Theoretical analysis documented that the loading time had a

more significant impact on pavement responses in the summer and the loading time could influence the dynamic response of flexible pavements significantly (Yin et al. 2008). However, few studies have investigated the loading equivalency between FWD and moving vehicular loading in terms of pavement responses along with stress pulse durations. The problem is complex because asphalt pavement responses under moving loading vary at different locations, speeds, and temperatures.

## **2.2 Backcalculation of Pavement Layer Modulus**

### *2.2.1 Iteration-based Approach*

Backcalculation problems were usually solved through an optimization process performed to obtain inverse mapping of a known relationship established by discrete or continuous data points. The back-calculation of pavement layer properties primarily involves two steps: 1) simulate pavement surface deflections under FWD loading; 2) determine layer properties from inverse analysis by minimizing the differences between calculated deflections and FWD measurements. In practice, the thickness of existing layer was usually known from construction records or survey using ground penetrating radar (GPR), while the Poisson's ratio was usually assumed for typical materials. Therefore, the existing layer moduli were the unknown parameters that need to be back-calculated.

Elasticity theory has been used for many years by engineers to analyze pavement responses subjected to traffic loading due to its simplicity and cost effectiveness. Therefore, by using the multilayered elastic theory, a theoretical deflection basin can be fitted to a measured deflection basin by adjusting the modulus of each layer using an adapted iterative searching technique. This iterative method is the most commonly used back-calculation method and a number of software programs are available (such as MODULUS, ELMOD, EVERCALC, BAKFAA). Figure 2.1 shows the typical flowchart of the iterative back-calculation process. It should be mentioned that the inverse process

can be performed by several techniques, such as least-square approaches, gradient descent methods, and database searching algorithms.

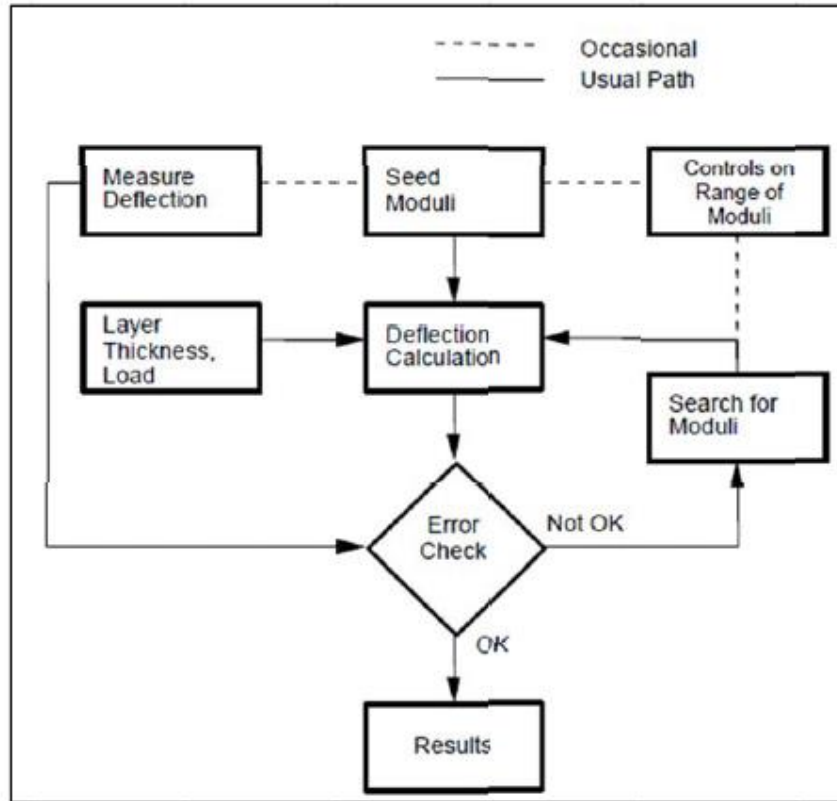


Figure 2.1 Flowchart of modulus backcalculation based on iterative procedure (after the EVERCALC user manual)

### 2.2.2 Limitations of Iteration-Based Approach

Many programs assumed linear elastic behavior of pavement layers and few considers the non-linear anisotropic behavior of unbound material and viscoelastic behavior of asphalt mixture. For example, if the viscoelasticity was not considered, the backcalculated elastic modulus only captured the behavior of asphalt material at a specific temperature and loading frequency and thus cannot be used to accurately predict pavement responses at a wide range of temperature and vehicle speed. Another disadvantage of current backcalculating practice was using static analysis, whereas the

applied load in the FWD is a dynamic load in nature. Previous studies have shown that for the unbound layer under asphalt surface, the ratios between the backcalculated moduli from standard procedures and the laboratory-measured values ranged from 0.35 to 0.62 due to the dynamic effect (Von Quintus and Killingsworth 1998).

Conventional backcalculating processes can be mainly grouped as static and dynamic ones. The static one makes use of merely the peak values of FWD deflections to backcalculate the linear elastic modulus for each layer (Huang 1993). The key portion of static backcalculation relies on iterative procedure with seed layer moduli. The iterative procedure in nature delivers trial and error algorithm to repeatedly comparing calculated and measured deflections. The static backcalculation techniques were not computationally robust and may cause divergence in some scenarios. The starting modulus (seed modulus) should be adjusted based on the user's experience and judgment to arrive at a reasonable modulus with the desired root mean square error (RMSE). This makes the backcalculation process dependent on the user's experience and sometimes the seed modulus can lead to a local solution rather than a global one to the problems. In addition, dynamic procedure otherwise considers the full time histories of FWD deflections related to complex moduli in time/frequency domain. Therefore, the complex moduli were processed in a forward procedure to iteratively search for the best matched FWD deflections in fitted frequency domain or time domain. (Uzan 1994). Some limitations were found in the dynamic backcalculation such as time-consuming and much more accurately measured deflection-time history.

### *2.2.3 Soft Computing Approach*

Soft computing techniques, compared to hard computing ones, accommodate tolerance of imprecise solutions to nondeterministic polynomial time-complete problems of interests. Machine Learning and Evolutionary Algorithms are the ones that serve as typical Artificial Intelligence (AI) techniques from Soft computing techniques. Machine Learning and Evolutionary Algorithms have introduced ANNs and GAs, respectively,

into pavement community where people have investigated and practiced ANNs and GAs for decades (Meier 1995; Fwa et al. 1997; Lee et al. 1998; Tutumluer et al. 2009).

In Machine Learning, ANNs are a family of models inspired by biological neural networks (the central nervous systems of animals, in particular the brain) and were used to estimate functions that can depend on a large number of inputs and are generally unknown. ANNs were generally presented as systems of interconnected "neurons" which exchange messages between each other. The connections have numeric weights that can be tuned based on experience, making neural nets adaptive to inputs and capable of learning. ANN is naturally utilized for collecting information to generate computational models resembling human mind, because it is capable of searching the most approximate solutions to nonlinear problems for arbitrary input and output variables.

Genetic Algorithms (GAs) are originally derived from the evolutionary algorithms which mimic the key procedure in the nature and dominate the evolution of species on the earth.. GAs are search-heuristic that optimizes the process of natural selection. GAs can perform as a searching technique to help prevent problem-solving program from dropping into local minima. GAs can generate solutions to optimization problems using techniques inspired by natural evolution, such as inheritance, mutation, selection, and crossover.

#### *2.2.4 Backcalculation with Soft Computing Approach*

Soft computing techniques have been applied in pavement community in recent years. One soft computing technique used for FWD backcalculation is Artificial Neural Networks (ANNs). ANNs were recommended mainly due to three merits over traditional backcalculation such as less error, high efficiency, and output uniqueness. Meier (1995) conducted research on backcalculating pavement-layer moduli through on-site tested FWD deflections using an ANN-based approach. The method was initiated by training a feedforward backpropagation networking structure. Then the trained ANN was validated with field measurements to prove the soundness of this method. Lee et al. (1998) developed an ANN-based model that used deflection basin parameters (DBPs) to

backcalculate the Young's moduli in asphalt and unbound material layers. To obtain computationally efficient results, two ANN models were trained and tested to estimate the layer moduli by means of layer thicknesses and DBPs.

Ceylan et al. (2007) established an ILLI-PAVE FE program-based solution database to develop three ANN-based models that considered modulus linearity in asphalt layer and nonlinearity in unbound layers. Mun and Kim (2009) used two different approaches for estimating the nonlinear coefficients in stress- and strain-dependent subgrade models by using ANN-based models. Gopalakrishnan et al. (2014) developed an ANN-based process to estimate dynamic moduli of asphalt concrete from single-drop FWD deflection-time history. However, field validation showed that the current accuracy level of existing models can hardly reach the requirement of practical application.

To enhance the capability of soft computing for backcalculation, Genetic Algorithms (GAs) can serve as an optimization tool. GAs can facilitate ANN programs to optimize solutions faster. Fwa et al. (1997) developed a GA-based program NUSGABACK to backcalculate pavement layer moduli. The results successfully eliminated the local minima and were validated with field testing data and compared to different backcalculating programs. To address the limitation that conventional backcalculating programs were applied for not more than five layers, Alkasawneh (2007) developed a novel GA-based program (BackGenetic3d) that can accommodate an arbitrary number of pavement layers.

Tutumluer et al. (2009) developed a program SOFTSYS by employing GAs as a search tool in the ANN-based inverse modeling. The database that the developed model relied on was assembled from a forward procedure from nonlinear FE solutions using ILLI-PAVE. Zaabar et al. (2014) developed DYNABACK-VE program that combined viscoelastic dynamic solutions in the time domain and genetic algorithm for backcalculation analysis. Varma and Kutay (2016) developed a backcalculating program (BACKLAVAN) in which linear viscoelastic and nonlinear elastic parameters in asphalt and aggregate base layers were calculated using a quasi-static analysis approach.

## 2.3 Airfield Pavement Design and Analysis

### 2.3.1 FAA Rigid and Flexible Iterative Elastic Layered Design (FAARFIELD)

In the field of airport pavement, the loading level and pavement layer thickness differ from the ones in the highway pavement community. However, the failure mechanisms that serve for pavement design and analysis are similar to each other. The FAA Rigid and Flexible Iterative Elastic Layered Design (FAARFIELD) software is developed for design of airfield pavement layer thickness. It has been updated since the first released version and the latest version is FAARFIELD 1.41 according to AC 150/6320-6F (FAA 2016). The FAARFIELD software possesses mechanistic analysis of stresses and strains within elastic layered pavement structure using empirically-based performance models to process a design. It incorporates the iterative elastic layered design into rigid and flexible pavements in consideration of responses to aircraft tire loading by 3D FE program. The HMA surfacing layer was assumed as linear elastic model. And the unbound layers were also in assumption of linear elastic model. The specification standards of the layer materials were denoted in the way different than in highway pavement ones, such as P-401 or P-403 for different dense-graded asphalt course, P-501 for concrete pavement, P-208 or P-209 for non-crushed or crushed aggregate base course, P-154 or P-301 for subbase course, and P-212 or P-213 for shell or sand clay base course (FAA 2014). The aircraft loading was assumed as uniformly stresses-distributed in a rectangular tire footprint.

In FAARFIELD program, the thickness design for fatigue failure is in the form of a cumulative damage factor (CDF) using Miner's rule. CDF represents the value of structural fatigue life of pavement in design. The fatigue life is indicated in terms of the ratio of applied load repetitions to allowable load repetitions to failure. An introductive example is given here for a single airplane along with constant annual departures, as shown in Equation 2-1 (FAA 2009). When the CDF value is more than one, it means that the pavement exceeds its fatigue life. The SCI is developed from pavement condition index (PCI) and SCI is also provided in the FAARFIELD. It ranges from a maximum

rating of 100 to a lowest of 0. The condition of existing pavement can also be described in the FAARFIELD by the cumulative damage factor used (CDFU). It signifies the amount of life that has been used up to as required for overlay, as shown in Equations 2-2 and 2-3. The derivation of the revised flexible pavement failure model in FAARFIELD 1.41 was described in an FAA technical report (Brill and Kawa, 2016). Compared to the previous failure model, the new models are defined in Equation 2-4 and 2-5. There is a transition point (at 1000 coverages), whereas the new model is smooth and continuous.

$$CDF = \frac{\text{number of applied load repetitions}}{\text{number of allowable load repetitions to failure}} \quad (2-1)$$

$$CDFU = \frac{L_U}{0.75L_D} \quad \text{when } L_U < 0.75L_D \quad (2-2)$$

$$CDFU = 1 \quad \text{when } L_U > 0.75L_D \quad (2-3)$$

Where,

$L_U$  = number of years of operation of the existing pavement until overlay; and

$L_D$  = design life of the existing pavement in years.

$$\log_{10}(C) = (-0.1638 + 185.19\varepsilon_v)^{-0.60586} \quad (C > 1000 \text{ coverages}) \quad (2-4)$$

$$C = \left( \frac{0.004141}{\varepsilon_v} \right)^{8.1} \quad (C \leq 1000 \text{ coverages}) \quad (2-5)$$

Where,

$C$  = the coverage level calculated at the top of the subgrade; and

$\varepsilon_v$  = the vertical strain, also at the top of the subgrade calculated by LEAF.

### 2.3.2 Airfield Pavement Studies at NAPTF

Full-scale tests have been conducted at the National Airport Pavement Test Facility (NAPTF) to evaluate pavement responses under aircraft loading. APT at the NAPTF showed that the rutting and upheaval in a conventional flexible pavement on medium-



strength subgrade were mainly attributed to shear failure in the base, subbase and subgrade (Garg 2001; Hayhoe and Garg 2002). Garg and Hayhoe (2001) found that the asphalt concrete strain responses were strongly affected by the pavement temperature and loading speed. Through an APT research, Fabre et al. (2010) emphasized the importance of considering non-uniform contact stress distribution in the analysis of high tire pressure effect on pavement responses. Gomez-Ramirez and Thompson (2002) presented the presence of nonlinearity of layer material at NAPTF through investigation of the compression of each layer from multi-depth deflectometer (MDD) records. Some studies were conducted in collaboration of NAPTF and Center of Excellence for Airport Technology (CEAT) to incorporate the multiple-wheel heavy gear load (MWHGL) aircraft into the ILLI-PAVE program (Garg et al., 1998; Thompson and Garg, 1999). Recently, an instrumented full-scale airport pavement testing was implemented at the NAPTF to monitor the cracking development under an accelerated loading and significant temperature cycling (Yin 2014).

In recent years, to practically and efficiently investigate the prevention of rutting and surface initiated fatigue cracking in asphalt concrete due to slow moving aircrafts, thick asphalt pavements were constructed at NAPTF to improve airport pavement service life. Shen and Carpenter (2007) conducted the study of a fatigue endurance limit showing that by applying the validated relationship between plateau value (PV) and fatigue life ( $N_f$ ), it is of no necessity to implement millions of loading cycles for extremely long fatigue life under low strain–damage condition. Kim et al. (2009) have found that the rutting development in the thick base layer is significant due to the shear stress caused by the moving load at NAPTF, conducting the computer simulation of multiple wheel loading of aircraft to investigate stress states in unbound material layer. A method for estimating the allowable strain in the asphalt layers of flexible airfield perpetual pavements was applied and validated by NAPTF tensile strain data determine the strain at the critical pass for each pavement section (Mehta 2015). Tire-pavement interaction has lacked of experimentally documented due to the limitations of conventional pavement instrumentation technology. A research related to Construction Cycle 6 (CC6) was

conducted to assess the damage mechanism of airfield rigid pavement, and an HWD testing was carried out on the test sections to backcalculate the stiffness of the layers (Cunliffe et al. 2016). A project for construction cycle 7 (CC7) was implemented, five flexible pavements constructed. Garg et al. (2014) proposed an experimental investigation of near-surface strains induced under Heavy Weight Deflectometer (HWD) as well as aircraft tires by using an innovative instrumentation system based on fiber optic sensors. Li et al. (2016) developed flexible perpetual pavement design criterion and validated and modified the fatigue model for asphalt concrete. The effects of traffic speed, gear configuration, and wheel load on the asphalt concrete strain were investigated based on CC7.

### *2.3.3 Boeing and FAA High Tire Pressure Test*

A series of full-scale tests have been conducted at the National Airport Pavement Test Facility (NAPTF) to evaluate pavement responses under aircraft loading with high tire pressure. The first high tire pressure test was initiated in 2005 by Boeing (Roginski 2007). Three sections with different asphalt surface thicknesses (2, 4, and 6 inches) were loaded by a single wheel at 2.5 mph. The loading cycles were applied by increasing the load from 40,000 to 50,000 lbs and the tire pressure from 140 to 240 psi. The results showed that higher tire pressure with maximum single wheel load of 55,000 lbs can produce increasing rutting depth or extensive cracks to pavement failure. The testing was stopped when the rutting depth reached 0.5-0.75 inches or extensive cracking was observed. The pavement temperature during testing is in the range of 70-80°F. It was found that the rutting in the asphalt layer was the main failure mode under heavy aircraft loading, and high tire pressure had no adverse effect on flexible pavements that have stable asphalt layers and meet thickness requirement.

A second series of high tire pressure testing was conducted in 2009 on heated pavement sections (Song 2010). The purpose was to duplicate the worst-case conditions for pavement rutting likely to be encountered in the field. Two different heating methods, hydronic heating system with hot water pipes and electrically heated wire mesh system,

were used in the initial test sections. The test sections were rebuilt with the strengthened pavement structure that included a 5-inch asphalt surface layer and a 17-inch Econocrete base layer placed on the DuPont clay subgrade. Two asphalt binder grades (PG 64-22 and PG 76-22) were used. The hydronic heating system was finally used since it was proven to be more reliable than the electrical heating system. The pavement temperature was kept between 100-110°F during the cyclic loading process. Dual tires with 54-inch (137.2-cm) spacing were used by using different levels of inflation pressure (210 and 245 psi) for each tire. The applied wheel loads were 52,500 and 61,300 lbs with three different wandering locations. The loads were applied in one direction only with a trafficking speed of 1 ft/s. The primary, secondary, and tertiary phases of rutting development were observed as the loading cycles increased. It was found that the observed differences in rutting depth were in the range 0 to 4 % due to the tire pressure effect.

#### *2.3.4 Airbus High Tire Pressure Test*

A series of high tire pressure tests were carried out in Toulouse, France by Airbus and French STAC (Civil Aviation Technical Service) in 2010 to evaluate pavement performance under multi-wheel loading of heavy aircraft (Airbus 2010). The Airbus Heavy Traffic Simulator (HTS) was used in the test, which has full-scale landing gear with modular assembly up to five bogies and had the capacity of generating up to 70,500 lbs for each single wheel with a maximum speed of 5 mph. The simulator was equipped with A340 tires and the tire inflation pressure could be adjusted to simulate other aircraft tires. Four dual-wheel assemblies were used to apply different levels of wheel load and tire pressure that were sufficiently spaced enough to prevent any interaction between multiple wheels.

Seven test sections were designed according to the French airport pavement design method for 10,000 passes of B747-400 gear. The pavement sections had a 10-inch asphalt layers with different thickness combination of surface and base asphalt layers and a 15-inch subbase layer of untreated graded aggregate supported by a foundation. The loading

configurations used in the test included two load levels (57,400 and 66,400 lbs) and two pressure levels (218 and 254 psi). The loading was applied on pavement up to 10,000 passes to cause the rutting depth of 0.5 to 0.75 inches, which is considered a medium severity rutting for airport pavement remediation. The average temperatures of asphalt surface layer were 68-86°F in the initial configurations and then increased to 104-122°F. The full-scale test results showed that rutting depth differences ranged from 0.075 to 0.2 inches that varied depending on the magnitude of wheel loading. This indicated that the increase of tire pressure from 218 to 254 psi would not have critical impact on the rutting development in the asphalt layer. The rutting initiation appeared more affected by the average temperature in the asphalt layer than the traffic condition or loading level.

## **2.4 Summary**

The FWD is designed to impart a load pulse to the pavement surface by dropping a large weight. Many studies are conducted on the simulation of FWD to interpret its mechanism and investigate affecting factors on the backcalculation. Deflection basin parameters (DBPs), which are derived from FWD deflection measurements, are established to indicate layer properties and pavement conditions. The discrepancies caused by stationary and moving loading patterns could be present in loading periods (pulse durations) and magnitudes of pavement responses (stress, strain, and deflection). A number of studies have been conducted to measure the pulse durations under traffic loading and compare the pulse durations under FWD and moving vehicular loading.

Backcalculation problems were usually solved through an optimization process performed to obtain inverse mapping of a known relationship established by discrete or continuous data points. Many programs assumed linear elastic behavior of pavement layers and few considers the non-linear anisotropic behavior of unbound material and viscoelastic behavior of asphalt mixture. Conventional backcalculating processes can be mainly grouped as static and dynamic ones. Soft computing techniques, compared to hard computing ones, accommodate tolerance of imprecise solutions to nondeterministic

polynomial time-complete problems of interests. Soft computing techniques have been applied in pavement community in recent years.

In the field of airport pavement, the loading level and pavement layer thickness differ from the ones in the highway pavement community. However, the failure mechanisms that serve for pavement design and analysis are similar to each other. A series of full-scale tests have been conducted at NAPTF to evaluate pavement responses under aircraft loading with high tire pressure. In recent years, to practically and efficiently investigate the prevention of rutting and surface initiated fatigue cracking in asphalt concrete due to slow moving aircrafts, thick asphalt pavements were constructed at NAPTF to improve airport pavement service life.

## CHAPTER 3 FINITE ELEMENT MODELING OF FLEXIBLE PAVEMENT UNDER FWD LOADING

### 3.1 Material Constitutive Models and Analysis Type

#### 3.1.1 Viscoelastic Model of Asphalt Concrete

Constitutive models of each pavement layer are important for mechanistic analysis of pavement responses. The relaxation modulus of asphalt mixture was modeled as a generalized Maxwell solid model in terms of Prony series, as shown in Equation 3-1 (Park and Schapery 1999). The relaxation modulus can be obtained from the complex modulus components (Equations 3-2 and 3-3) based on the interconversion theory. The dynamic modulus were measured in the laboratory using frequency-sweep test at different temperatures and the sigmoidal master curve can expressed using Equation 3-4. The temperature dependency of AC modulus is characterized by time-temperature superposition principle. The relationship between the shift factor and the temperature can be approximated by the Williams-Landell-Ferry (WLF) function, as show in Equation 3-5 (ABAQUS 2010).

$$E(t_r) = E_0 \left( 1 - \sum_{i=1}^N E_i \left( 1 - e^{\frac{-t_r}{\tau_i}} \right) \right) \quad (3-1)$$

$$E'(\omega) = E_\infty + \sum_{i=1}^n \frac{\omega^2 \tau_i^2 E_i}{1 + \omega^2 \tau_i^2} \quad (3-2)$$

$$E''(\omega) = \sum_{i=1}^n \frac{\omega \tau_i E_i}{1 + \omega^2 \tau_i^2} \quad (3-3)$$

Where,

$E_0$  is instantaneous elastic modulus;

$E_i$  and  $\tau_i$  are Prony series parameters;

$t_r$  is reduced time;

$E'(\omega)$  is real part of dynamic modulus;

$E''(\omega)$  is imaginary part of dynamic modulus;

$E_{\infty}$  is equilibrium relaxation modulus at infinite time; and  
 $\omega$  is angular frequency.

$$\log(|E^*(\omega)|) = c_1 + \frac{c_2}{1 + e^{(c_3 + c_4 \log(t_r))}} \quad (3-4)$$

$$\log a_T = -\frac{C_1(T - T_R)}{C_2 + (T - T_R)} \quad (3-5)$$

Where,

$c_i$  are sigmoid coefficients;

$a_T$  is shift factor and  $t_R = t / a_T$

$T_R$  is reference temperature (21.1°C in this study); and

$C_1$  are regression coefficients.

### 3.1.2 Nonlinear Cross-Anisotropic Model of Unbound Material

The importance of including the nonlinearity and cross anisotropy of unbound material resilient modulus in the base layer and subgrade has been increasingly pronounced. Schwartz (2002) demonstrated that excluding nonlinear unbound material properties produced substantial errors in responses of flexible pavements. Park and Lyton (2004) applied stress-dependent isotropic models to consider resilient modulus and Poisson's ratio of unbound layer materials to predict responses in flexible pavements. Masad et al. (2006) presented the advantage of considering aggregate anisotropic behaviors to analyze measured pavement surface deflections under vehicular loading. Al-Qadi et al. (2010) found that the assumption of isotropic linear behavior for base material resulted in an overestimation of predicting pavement service life. Kim et al (2009) concluded that different responses in flexible pavements were found using isotropic and cross-anisotropic modulus of base layer. Recently, Wang and Al-Qadi (2013) emphasized the importance to consider the viscoelasticity of the asphalt layer and the moving load for

accurately capturing the nonlinear granular base modulus in the mechanistic pavement analysis.

The resilient modulus of granular material is defined as the ratio of the deviator stress to the recoverable part of the axial strain from the repeated-load triaxial tests, as shown in Equation 3-6. A generalized model is adopted in the Mechanistic-Empirical Pavement Design Guide (MEPDG) (now Pavement ME), as expressed in Equations 3-7 to 3-9 (ARA 2004). In this Equation 3-7, for example, the first stress invariant or bulk stress term considers the hardening effect due to positive values of  $k_1$  and  $k_2$ , while the octahedral shear stress term considers the softening behavior with respect to the negative values of  $k_3$ .

$$M_r = \frac{\sigma_d}{\varepsilon_r} \quad (3-6)$$

Where,

$\sigma_d$  is deviator stress; and

$\varepsilon_r$  is recoverable strain.

$$M_r^v = k_1 p_a \left( \frac{\theta}{p_a} \right)^{k_2} \left( \frac{\tau_{oct}}{p_a} + 1 \right)^{k_3} \quad (3-7)$$

$$M_r^h = k_4 p_a \left( \frac{\theta}{p_a} \right)^{k_5} \left( \frac{\tau_{oct}}{p_a} + 1 \right)^{k_6} \quad (3-8)$$

$$G_r = k_7 p_a \left( \frac{\theta}{p_a} \right)^{k_8} \left( \frac{\tau_{oct}}{p_a} + 1 \right)^{k_9} \quad (3-9)$$

$$\text{with } \theta = \sigma_1 + \sigma_2 + \sigma_3 \text{ and } \tau_{oct} = \frac{1}{3} \sqrt{(\sigma_1 - \sigma_2)^2 + (\sigma_2 - \sigma_3)^2 + (\sigma_1 - \sigma_3)^2}$$

Where,

$M_r^v$  is vertical resilient modulus (kPa) ;

$M_r^h$  is horizontal resilient modulus (kPa) ;

$G_r$  is shear resilient modulus (kPa) ;

$\theta$  is bulk stress (kPa);



$\tau_{oct}$  is octahedral shear stress (kPa);

$\sigma_1$ ,  $\sigma_2$ , and  $\sigma_3$  are maximum, middle, and minimum principal stresses;

$k_1 - k_9$  are exponent parameters; and

$p_a$  is atmospheric pressure (100kPa).

The aggregate base layer was modeled as a nonlinear cross-anisotropic material and the vertical modulus was described using the generalized model in Equation 3-1. For the anisotropic modulus, the horizontal and shear modulus ratios ( $n$  and  $m$ ) were used, as shown in Equation 3-10 and 3-11. Equations 3-7, 3-10, and 3-11 are in the simplified form as compared to Equations 3-7 to 3-9. Previous research has found that horizontal modulus ratios and shear modulus ratios had a relatively small range of variation (Tutumluer and Thompson 1997). The modulus ratios were assumed constant as 0.15 for  $n$  and 0.34 for  $m$  in this study to observe the effect of aggregate properties on the nonlinear modulus parameters. The stress dependency of Poisson's ratios was not included and the in-plane and out-of-plane Poisson's ratios were separately assumed constant. The subgrade was assumed as linear elastic material. The resilient modulus of subgrade was estimated to be 53MPa from its CBR value (ARA 2004).

$$n = M_r^h / M_r^v \quad (3-10)$$

$$m = G_r / M_r^v \quad (3-11)$$

Where,

$M_r^v$  is vertical resilient modulus (kPa);

$M_r^h$  is horizontal resilient modulus (kPa); and

$G_r$  is shear resilient modulus (kPa);

### 3.1.3 Nonlinear Solving Technique

ABAQUS/Standard uses the iterative Newton-Raphson method to solve nonlinear equations. The applied load in this method is augmented incrementally, and at each

increment the program solves a system of equations through iterations. The iterations continue on the basis of the previous solutions until it reaches a reasonable convergence (ABAQUS 2010). Because the modulus of the granular material is a function of the total stress states, a modified Newton-Raphson approach with secant stiffness was used in this study and implemented in a user material subroutine (UMAT).

The user material subroutine program requires three exponent parameters ( $k_1, k_2, k_3$ ) with two modulus ratios and two Poisson's ratios for calculating the nonlinear cross-anisotropic modulus. In addition, the initial vertical stress is calculated as the overburden stress that results from the density and thickness of the material above the point of interest. The initial horizontal stress depends on the material properties, over-consolidation history, and the residual stress caused by compaction. A coefficient of horizontal stress (1.0) is defined as the ratio of horizontal stress to overburden stress. To prevent unreasonable values, a cutoff value (30MPa) is used for the minimum resilient modulus at low stress levels. More details on the UMAT and solution scheme could be found elsewhere (Wang and Al-Qadi 2013).

### 3.1.4 Quasi-Static and Dynamic Analysis

Static, quasi-static, and dynamic analysis have been employed in many studies on pavement analysis and only dynamic analysis can better match the field FWD measurement results (Xu and Prozzi 2013). Dynamic transient analysis allows for the inertia associated with the FWD loading and the dependency of the material properties on the loading frequency. For a nonlinear dynamic analysis problem, the direct integration method is commonly employed; thus the implicit dynamic analysis was selected in this study, because it provides better numerical stability than explicit analysis and is generally efficient for structural dynamic problems (Bathe 1982). The equation of motion of a multiple degree of freedom system with viscous damping is shown in Equation 3-12. The Rayleigh damping was used for unbound materials in this study with  $\alpha$  as 0.02 and  $\beta$  as 0.06, as shown in Equation 3-13.

$$[M]\{\ddot{U}\} + [C]\{\dot{U}\} + [K]\{U\} = \{P\} \quad (3-12)$$

Where,

$[M]$  is mass matrix;

$[C]$  is damping matrix;

$[K]$  is stiffness matrix;

$\{\ddot{U}\}$  is acceleration vector;

$\{\dot{U}\}$  is velocity vector;

$\{U\}$  is displacement vector; and

$\{P\}$  is displacement vector.

$$[C] = \alpha[M] + \beta[K] \quad (3-13)$$

Where,

$\alpha$  is mass proportional Rayleigh damping coefficient; and

$\beta$  is stiffness proportional Rayleigh damping coefficient.

### 3.1.5 Temperature Distribution

The temperature dependency of AC modulus is characterized by time-temperature superposition principle. This behavior introduces the horizontal shifting of the material property to form a single characteristic master curve as a function of reduced time (or frequency) at a desired reference temperature. The relationship between the shift factor and the temperature can be approximated by the WLF (Williams-Landell-Ferry) function (ABAQUS 2010).

The BELLS3 equation, which was validated with measurements from field sections, was used in this study to predict temperatures within asphalt layer, as shown in Equation 3-14 (FHWA 2000). Compared to other temperature prediction models such as Huber (Huber 1994) and Park (Park et al. 2001), the BELLS3 equation predicted the distributed temperatures that were closest to the measured ones (Gedafa et al. 2013).

$$T_d = 0.95 + 0.892IR + [\log(d) - 1.25][-0.448IR + 0.621(1 - \text{day}) + 1.83 \sin(hr_{18} - 15.5)] + 0.042IR \cdot \text{Sin}(hr_{18} - 13.5) \quad (3-14)$$

where:

$T_d$  is pavement temperature at depth  $d$ , °C;

$IR$  is pavement surface temperature, °C;

$d$  is depth at which mat temperature is to be predicted, mm;

$1 - \text{day}$  is average air temperature the day before testing, °C;

$\text{Sin}$  is sine function on an 18-hr clock system, with  $2\pi$  radians equal to a 18-hr cycle; and

$hr_{18}$  is time of day, in a 24-hr clock system, but calculated using an 18-hr AC temperature rise-and-fall time cycle.

### 3.1.6 Interface Modeling

Contact conditions at layer interfaces are important parameters that could significantly affect pavement responses to vehicular loading. It is expected that the layers within the pavement structure remains in contact with no gap-opening since the contact area is very large and high compressive loading is applied by vehicles. In addition, it is assumed that both relative and absolute motions of contacting surfaces at layer interfaces are small. In this study, the Coulomb friction model with a friction coefficient of 1.0 was used at the HMA-Base interface and 0.3 for Base-subgrade interface (Romanoschi and Metcalf 2001).

## 3.2 Development of Axisymmetric FE Model

### 3.2.1 Pavement Structure and Material Parameters

The modeled pavement structure was constructed with three functional layers as shown in Figure 3.1. A 150-mm (6-in.) asphalt pavement is followed by a 300-mm (12-in.) aggregate base layer over a subgrade. Dynamic modulus in form of sigmoidal function is plotted by using the asphalt binder PG 64-22. The Prony series of the

relaxation modulus of asphalt layer is presented as well as the temperature shift factors. The nonlinear model parameters for base aggregate were referenced from the three dominant properties out of six significant aggregate properties (Wang and Li 2015). And extensive subgrade soil properties from Mississippi State were incorporated into the LTPP empirical equation to calculate the nonlinear subgrade model parameters (George 2004). Thus it is believed that the selected ranges of both unbound materials in Figure 3.1 are capable of representing sufficient variations of the nonlinear resilient moduli.

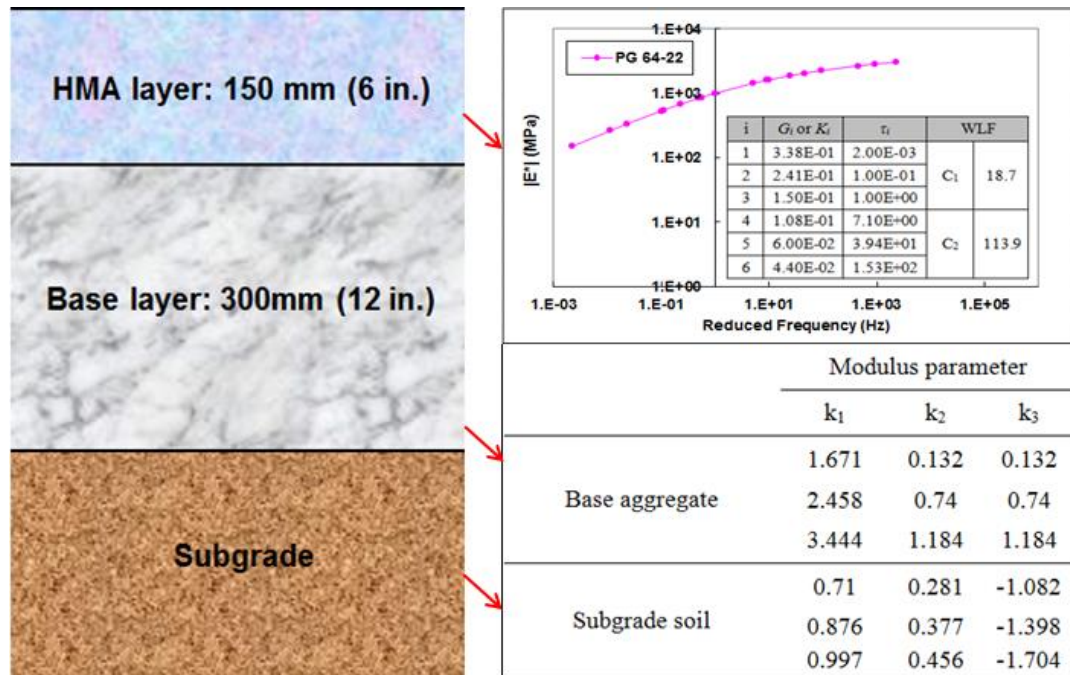


Figure 3.1 Thin flexible pavement structure with material properties of different layers

### 3.2.2 FE Model Meshes and Boundary Conditions

An axisymmetric 2-D FE model of the thin asphalt pavement was developed by applying the general-purpose software ABAQUS. The 2-D FE model is more appropriate for simulating the FWD testing in comparison to the 3-D FE model. It can better emulate a real circular load on the FWD-pavement interface, because the axisymmetric elements are capable of shaping an absolute circular load other than the elements in 3-D FE model. In this study, four-node bilinear axisymmetric solid elements were used in the finite

domain; while axisymmetric infinite elements were applied to reduce a large number of far-field elements without significant loss of accuracy and then to build a “silent” boundary for the dynamic analysis.

Figure 3.2 presents an axisymmetric 2-D FE model that discretizes the pavement structure. The FWD loading was represented by a circular impulse loading applied on the surface of asphalt layer. The FE mesh is refined around the circular loading area; instead a relatively coarse mesh is applied far away from the loading area. The length of elements within the loading area is selected at 12.7mm in the radial direction. The element thickness is selected to be 8.5mm for the asphalt layer. The selection for the element sizes is based on a mesh convergence study (Wang 2011).

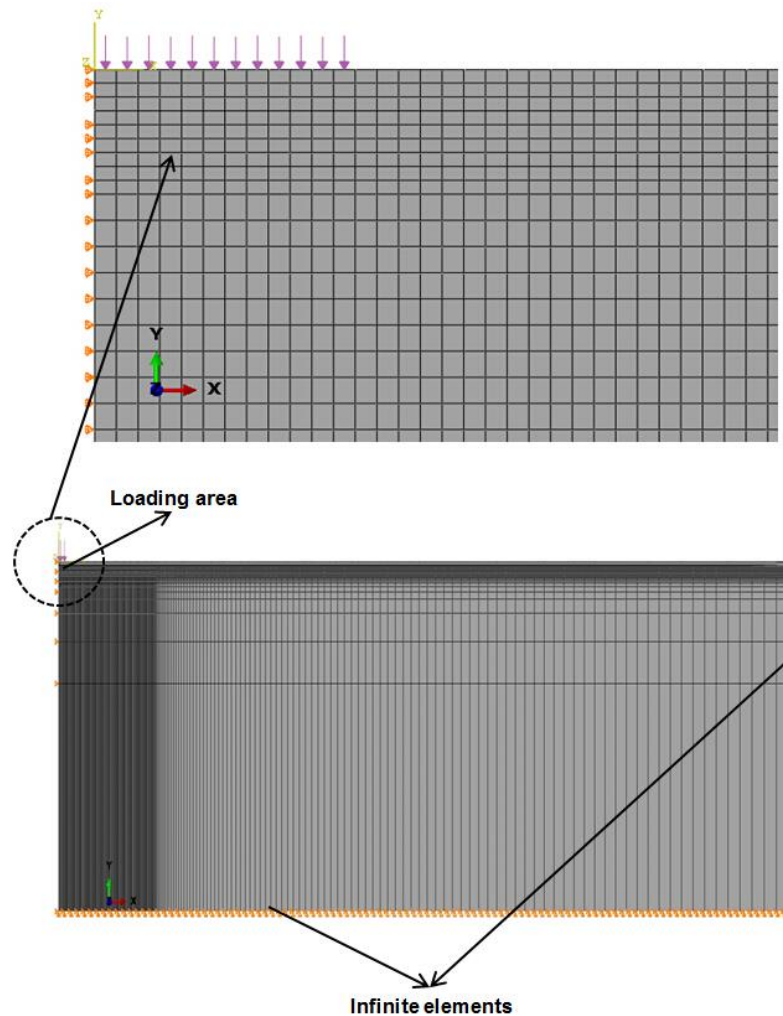


Figure 3.2 FE model layout in axisymmetric 2-D domain with infinite boundary and loading area

In this study, a sensitivity analysis was performed to define the infinite boundary in both radial and vertical directions, as shown in Figure 3.3. After comparing the maximum central and edge deflections in the asphalt layer, the locations of the infinite boundary in the two directions from the loading center are needed to be greater than 2.2m and 7.5m in order to obtain a stable solution (less than 5% changes). The eventual selected domain size as an axisymmetric 2-D model (finite + infinite) has to be of 2.5×8m to achieve the balance between computation cost and accuracy.

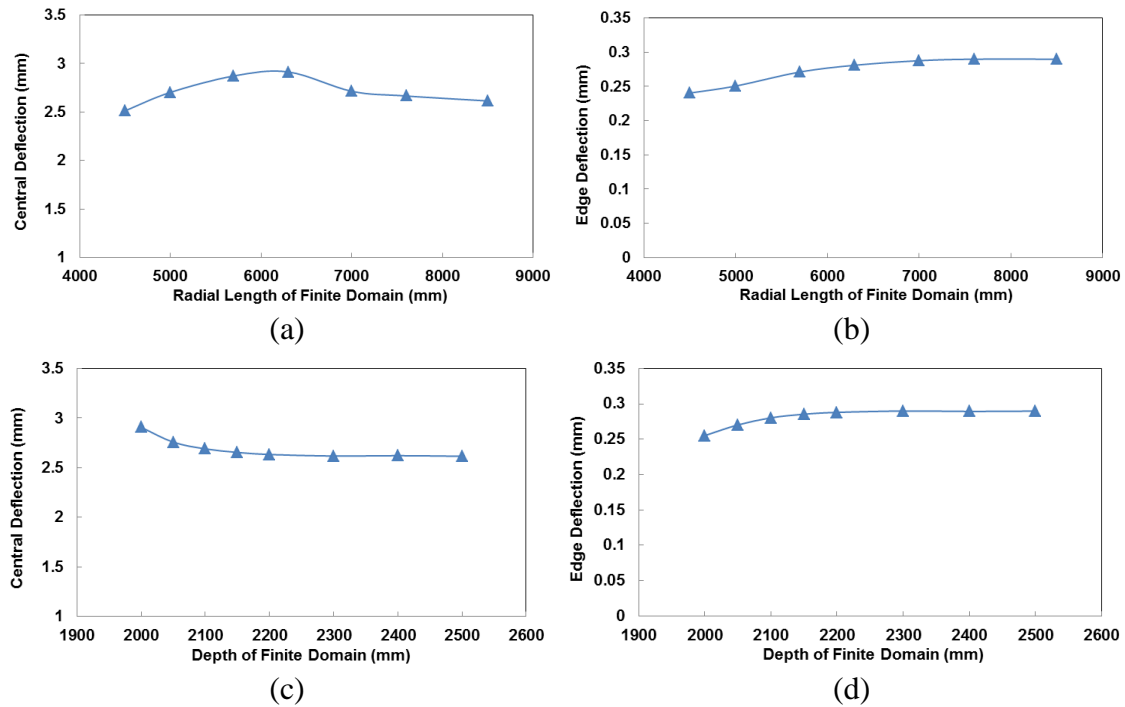


Figure 3.3 Sensitivity analysis for (a) central deflection vs. radial length of finite domain; (b) edge deflection vs. radial length of finite domain; (c) central deflection vs. depth of finite domain; and (d) edge deflection vs. depth of finite domain

Contact conditions at layer interfaces are important parameters that could significantly affect pavement responses under FWD loading. It is expected that the layers within the pavement structure remains in contact with no gap-opening since the contact area is very large and compressive loading due to gravity and traffic loading. Therefore, it is reasonable to assume that both relative and absolute motions of contacting surfaces at layer interfaces are small. In this study, the Coulomb friction model with a friction coefficient of 1.0 was used at the HMA-Base interface and 0.3 for base-subgrade interface (Romanoschi and Metcalf 2001).



### *3.2.3 Validation with Surface Deflections*

A validation study for the developed FE model was conducted with field testing results reported in the literature. The asphalt pavement section consists of an asphalt layer of 267mm and a base layer of 356mm, as shown in Figure 3.4 (a). Material properties were obtained from laboratory testing and pavement temperature profiles were recorded in the asphalt layer (Tarefder et al. 2014). The measured and predicted surface deflections at three different temperature profiles were compared, as shown in Figure 3.4 (b). The results show that with the FE models results have good agreements with the field measurements.

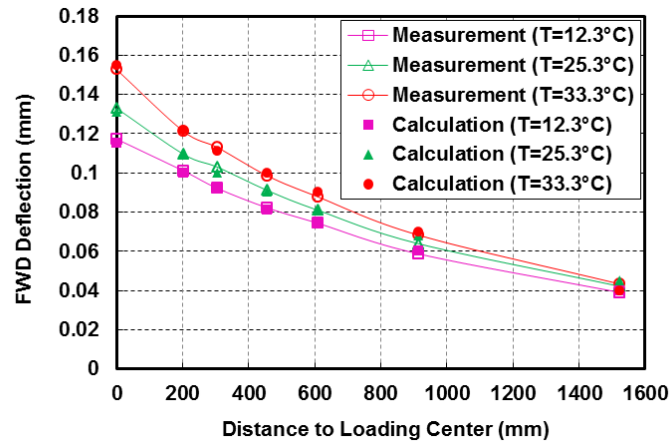
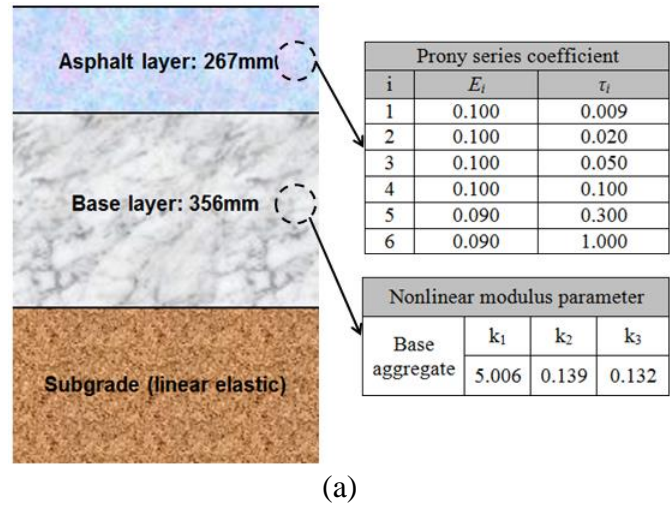


Figure 3.4 Validation of FE models with measurements under FWD loading

A validation for the developed axisymmetric 2-D FE model was conducted with field measurement results by using the pavement structure and layer material properties corresponding to the in-site condition (Kwon 2007). A 127-mm (5-in.) asphalt pavement with a 300-mm (12-in.) aggregate base layer was in consideration. And the temperature gradient was generated by applying the BELLS3 equation with surface temperature of 25°C (77°F) and air temperature of 20°C (68°F). The material properties were obtained from laboratory testing (Park and Kim 1999; Kwon 2007). Figure 3.5 compares the measured and predicted surface deflections under three different loading levels. The

results show that with the FE model results have good agreements with the in-site measurement. The Root Mean Squared Errors (RMSE) between the measured and predicted surface deflections are smaller than 0.1 mm for all deflections at different sensors.

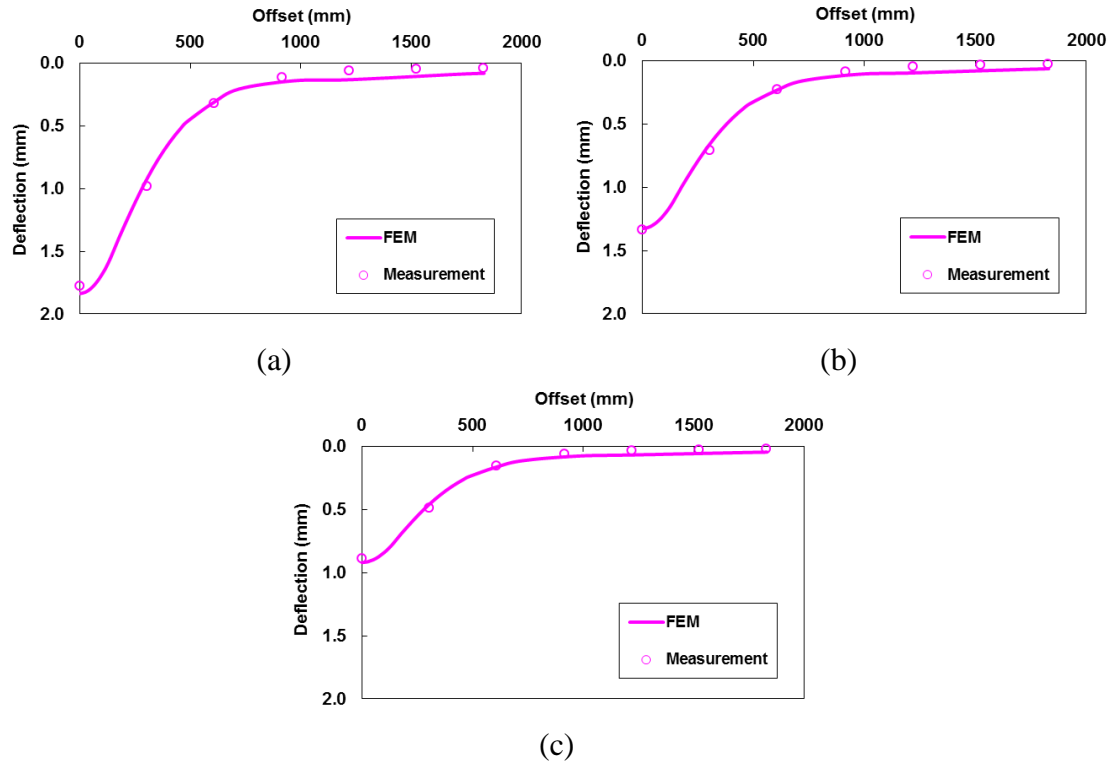


Figure 3.5 Validation of FE model with measurement under FWD loading of (a) 53kN; (b) 40kN; and (c) 27kN

### 3.3 Parametric Analysis and Results

#### 3.3.1 Analysis Parameters

The effects of primary factors on pavement responses under FWD loading were investigated using the developed FE model. Both the surface deflections and critical strains were considered in the analysis. Two specific deflection indicators D0 (deflection under central load) and D900 (deflection 900mm away from central load) were primarily used in the analysis. The two typical deflections can represent structure behavior of the

entire pavement system and the subgrade, respectively (Huang 1993). The critical strains analyzed included tensile strains at the bottom of HMA layer, compressive strains on the top of subgrade. It has been widely accepted that critical tensile strains in HMA layer are related to bottom-up fatigue cracking distress and compressive strains in subgrade are attributed to rutting failure. In addition, the load-deflection curve was used to indicate the energy dissipation of pavement system in terms of the hysteresis loop. The hysteresis loop was focused on the FWD loading-deflection (vertical displacement) rather than stress-strain loop, because the deflection can better represent the integrity of the pavement system than the critical strains (Ghuzlan and Carpenter 2000).

### 3.3.2 Effect of Dynamic Analysis

Figure 3.6 shows the comparisons between dynamic analysis and quasi-static analysis through the deflection-time and strain-time histories as well as the hysteresis loops of D0 and D900. The *IR* and 1-day were referenced as 23.5°C (74.3°F) and 14.2°C (57.6°F), respectively. And Equation 3-1 was used to model the in-depth temperature distribution. The load-time history is plotted to indicate the time shift between the applied load and resulting responses. It is believed that the time lag here is due to the viscoelastic and damping behaviors as well as the stress wave propagation from loading center. As expected, all the response-time history curves in Figure 3.6 (a) and (b) resemble the shape of the load-time history. It was found that the time lags to the load-time history were obvious in the D0- or D900-time histories under the dynamic analysis as compared to quasi-static analysis. Moreover, the magnitudes of D0 or D900 under dynamic analysis are larger than the ones under quasi-static analysis. It is worth mentioning that the D900 has a longer time lag than D0 in the displacement-time history. As mentioned before, the D0 represents the behavior of the entire pavement structure but D900 is uniquely attributed to the subgrade behavior. Therefore, the different time lags imply that the stress wave propagation plays a dominating role in addition to the viscoelastic behavior of asphalt layer and the damping effect of unbound layers.

On the other hand, as shown in Figure 3.6 (b), no time lags were observed for critical strains under both analysis approaches. However, the critical strains under dynamic analysis are slightly greater than the ones under quasi-static analysis. However, the discrepancies of strains under two analysis methods were not as significant as the deflections. This indicates that the difference of both analysis approaches casts more effect on the back-calculation of the layer moduli through FWD deflections rather than on the assessment of pavement performance through critical responses.

Figures 3.6 (c) and (d) show the hysteresis loops in terms of D0 and D900 to indicate the energy dissipation resulted from the FWD loading. If the loading and unloading paths coincide, it means that all the strain energy caused by the load is recovered after unloading. If not, the area between the loading and unloading curves indicates the dissipated energy due to the viscoelasticity, damping, or material damage. Figure 3.6 (c) shows that the dissipated energy in D0 using dynamic analysis is higher than the one using quasi-static analysis. It reveals that more energy is dissipated under the dynamic loading because of the damping behavior. The energy dissipation under quasi-static analysis can be attributed to the viscoelasticity of asphalt layer. In the case of Figure 3.6 (d) shows that the discrepancy of energy dissipation using two analysis methods is more significant for D900. These findings emphasize that the influence of dynamic analysis cannot be ignored for FWD loading.

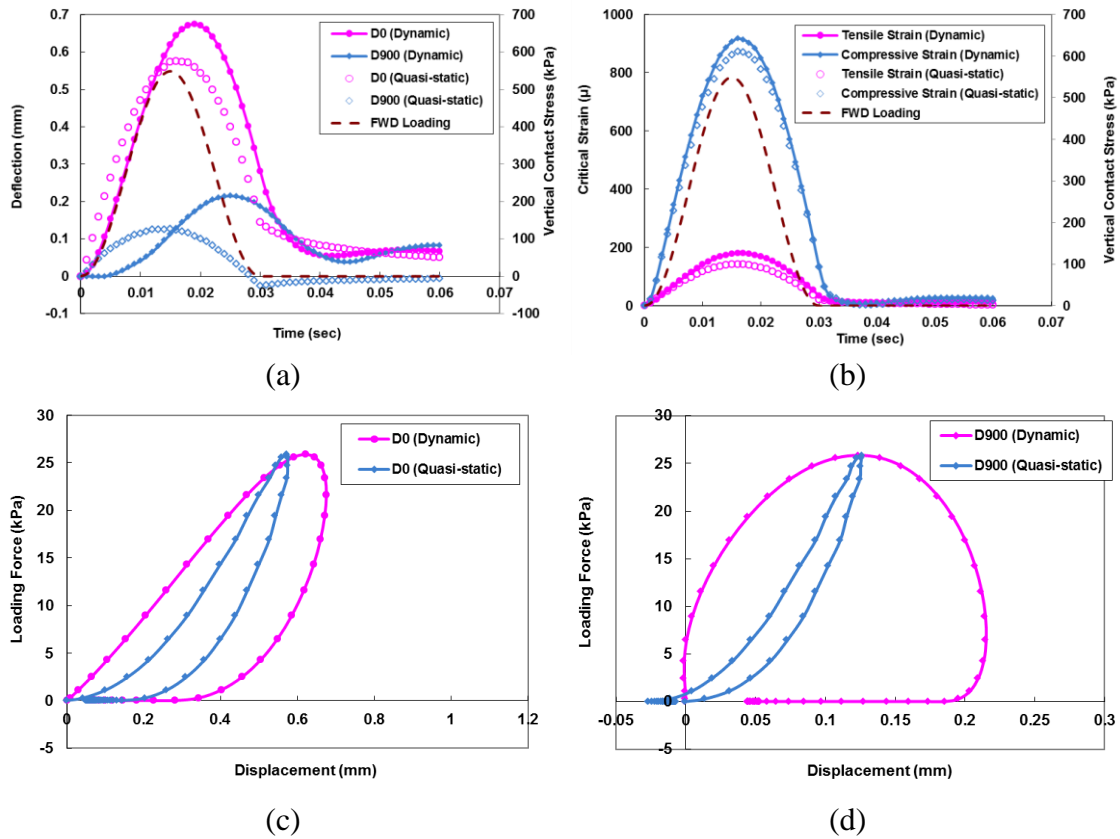


Figure 3.6 Dynamic analysis vs. quasi-static analysis through (a) deflection-time histories; (b) strain-time histories; (c) D0 hysteresis loops; and (d) D900 hysteresis loops

### 3.3.3 Effect of HMA Viscoelasticity

Figure 3.7 shows the comparisons between the viscoelastic asphalt material and elastic asphalt material through the deflection- and strain-time histories as well as hysteresis loops of D0 and D900. The elastic modulus of asphalt layer was selected according to the dynamic modulus at the loading frequency of 30.3 Hz that is calculated from the pulse duration of FWD loading. The *IR* and 1-day were referenced as 23.5°C (74.3°F) and 14.2°C (57.6°F), respectively. And Equation 3-10 was used to model the in-depth temperature distribution. In Figure 3.7 (a), the longer time lag and greater magnitude of D0 were observed for viscoelastic material; while the time lag and magnitude of D900 were similar using both material models. As shown in Figure 3.7 (b),

no time lags were found for critical strains using both material models, although the magnitudes of critical strains in the elastic asphalt material are greater than the ones in the viscoelastic one. It is noted that the assumption of elastic asphalt layer may underestimate or overestimate pavement responses, depending on the selection of loading frequency; therefore, it cannot capture the frequency-dependent response of viscoelastic material.

Figures 3.7 (c) and (d) show the hysteresis loops in terms of  $D_0$  and  $D_{900}$ . It shows that the dissipated energy of  $D_0$  in the viscoelastic asphalt material is higher than the ones in the elastic asphalt material, while the discrepancy between the two material models in terms of  $D_{900}$  is negligible. This is reasonable since more energy is dissipated in the case of viscoelastic asphalt material due to the “dashpots” in the generalized Maxwell solid model (Equations 3-1).

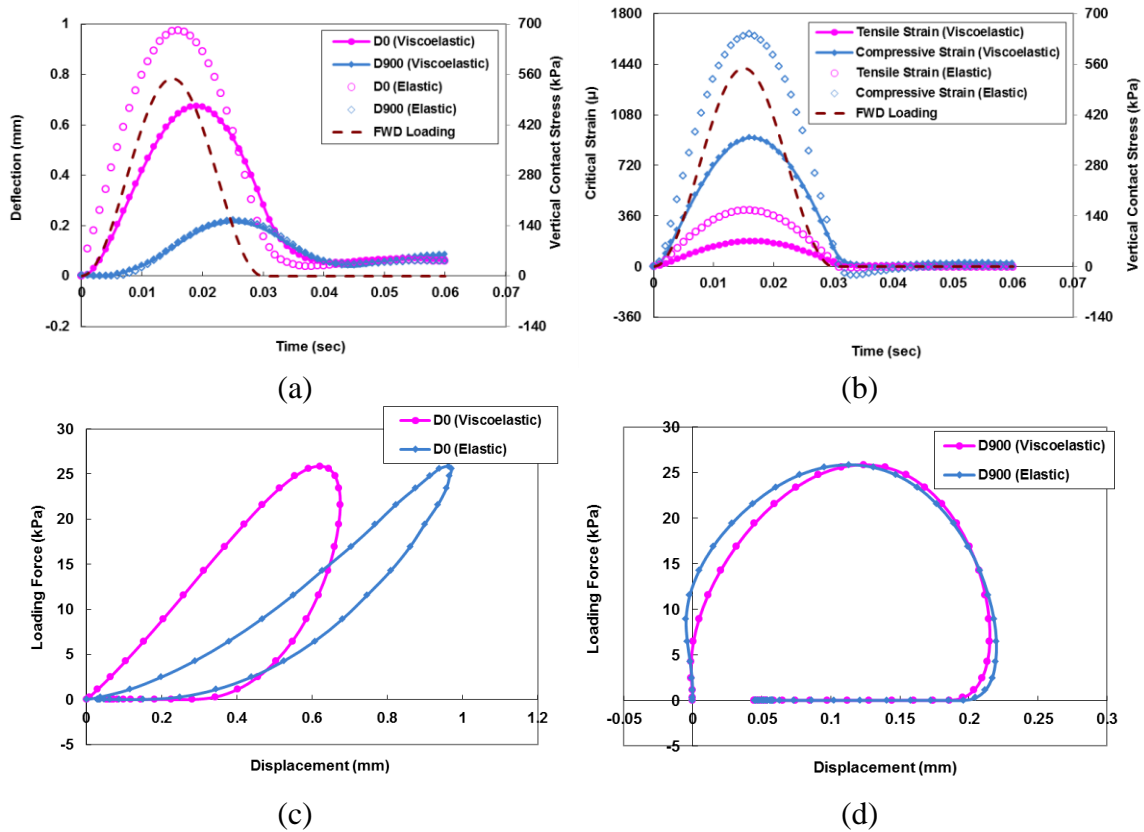


Figure 3.7 HMA viscoelasticity vs. elasticity through (a) deflection-time histories; (b) strain-time histories; (c) D0 hysteresis loops; and (d) D900 hysteresis loops

### 3.3.4 Effect of Temperature Gradient

The assumption of temperature profiles in the asphalt layer can also affect viscoelastic modulus of asphalt layer and accordingly pavement responses. Pavement temperature profiles were characterized using the BELLS model and the climate data extracted from the LTPP database (FHWA 2016). Two temperature conditions were considered to evaluate the effect of in-depth nonlinear temperature gradient on pavement deflections and critical strains as compared to the constant temperature gradient using average temperature. The pavement surface temperature and average air temperature in Equation 3-1 were selected as 23.5°C (74.3°F) and 14.2°C (57.6°F) for the intermediate temperature case and 37.5°C (99.5°F) and 25.2°C (77.4°F) for the high temperature case, respectively.



Figure 3.8 illustrates the comparisons of the deflection-time and strain-time histories using the different temperature gradients and the relevant average constant temperatures. In Figure 3.8 (a), the magnitudes of D0 or D900 under different temperature gradients were found close to each other. As shown in Figure 3.8 (b), for the compressive strains on the top of subgrade, no discrepancy of the amplitudes is found with regard to the temperature gradients. However, tensile strains at the bottom of asphalt layer under the constant average temperature gradient was found greater than the ones under the nonlinear temperature gradient. This is because the average temperature at the HMA bottom is higher than the nonlinear one at the same location. It is expected that the discrepancy of tensile strains might be enlarged as the temperature increases in summer time. As shown in Figure 3.8 (c) no difference was found for the targeted deflections. As anticipated, however, the critical strains in Figure 3.8 (d) are shown more sensitive to the temperature entering the higher level. Enlarged tensile strains are located between the different temperature distributions. This indicates that the nonlinear temperature gradient has a strong effect on the failure potential of bottom-up fatigue cracking for the relatively thin asphalt pavement.

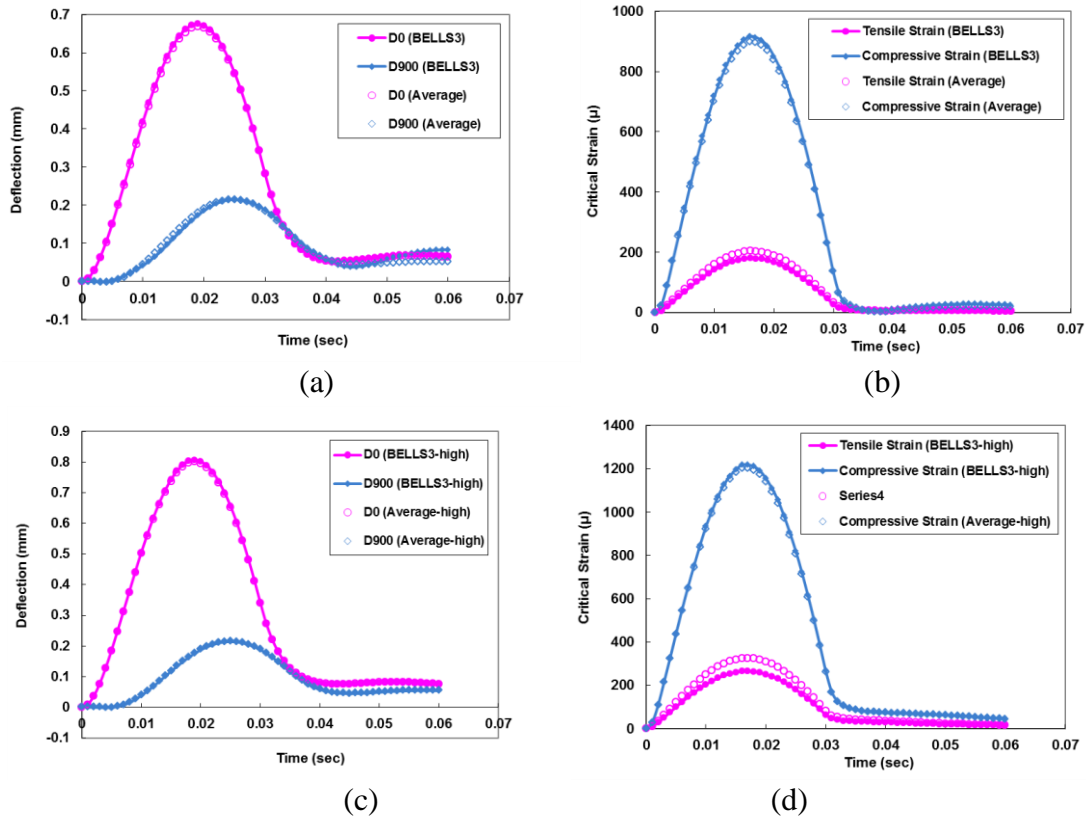


Figure 3.8 Effect of temperature gradient on (a) deflection-time histories at the intermediate temperature; (b) strain-time histories at the intermediate temperature; and (c) deflection-time histories at the high temperature; and (d) strain-time histories at the high temperature

### 3.3.5 Effect of Asphalt Layer Delamination

Although the asphalt layer is designed to be full-bonded, layer delamination could happen in the field due to poor construction quality. Figure 3.9 illustrates the effect of layer delamination within the asphalt layer on deflection- and strain-time histories as well as hysteresis loops. The debonded behavior was defined in the FE model by dividing the asphalt layer into two sub-layers (upper and lower) with frictional interaction at the mid-depth of 75 mm. As expected, Figure 3.9 (a) shows that deflection-time histories of D0 with fully-bonded asphalt layer are much smaller than the ones with debonded asphalt layer. However, Figure 3.9 (b) indicates that no difference can be found in D900 between

the two assumptions of bonding. It is reasonable because D0 represents the entire pavement behavior so that the layer debonding causes the larger magnitude of D0.

Figure 3.9 (c) shows the tensile strain-time histories under two bonding assumptions of the asphalt layer. Four scenarios are focused on investigating the delamination effect in terms of HMA upper/lower bottoms along with debonded/fully bonded asphalt layers. The critical tensile strain at the bottom of upper layer with the deboned asphalt layer has the maximum magnitude among all scenarios. As expected, the strains at the bottom of upper layer with the fully-boned asphalt layer are around zero or have small compressions. This can be attributed to the reasons that the bottom of upper layer with the debonded asphalt layer bears the most flexural deformation; while the bottom of upper layer with the fully-bonded asphalt layer experiences approximately zero strain on the neutral axis of bending. The layer debonding also reduces the tensile strain at the bottom of lower layer as compared to the fully bonded case. Figure 3.9 (d) presents that the compressive strains in the debonded case are much greater compared to the fully bonded case. Therefore, the delamination behavior can induce premature failure in fatigue cracking initiating at the bottom of asphalt upper layer or the permanent deformation in the subgrade. These observations signify that the asphalt layer bonding condition should be considered in FE modeling.

Figures 3.9 (e) and (f) show the hysteresis loops in terms of D0 and D900 in consideration of the asphalt layer delamination. It shows that the energy dissipation of D0 in the full-bonded case is different from the one in the debonded case. However, the energy dissipation of D900 in both cases keeps approximately similar to each other. In general, the results indicate that the layer debonding could be detected through both the magnitude and energy dissipation of D0 if in-situ testing data are available.

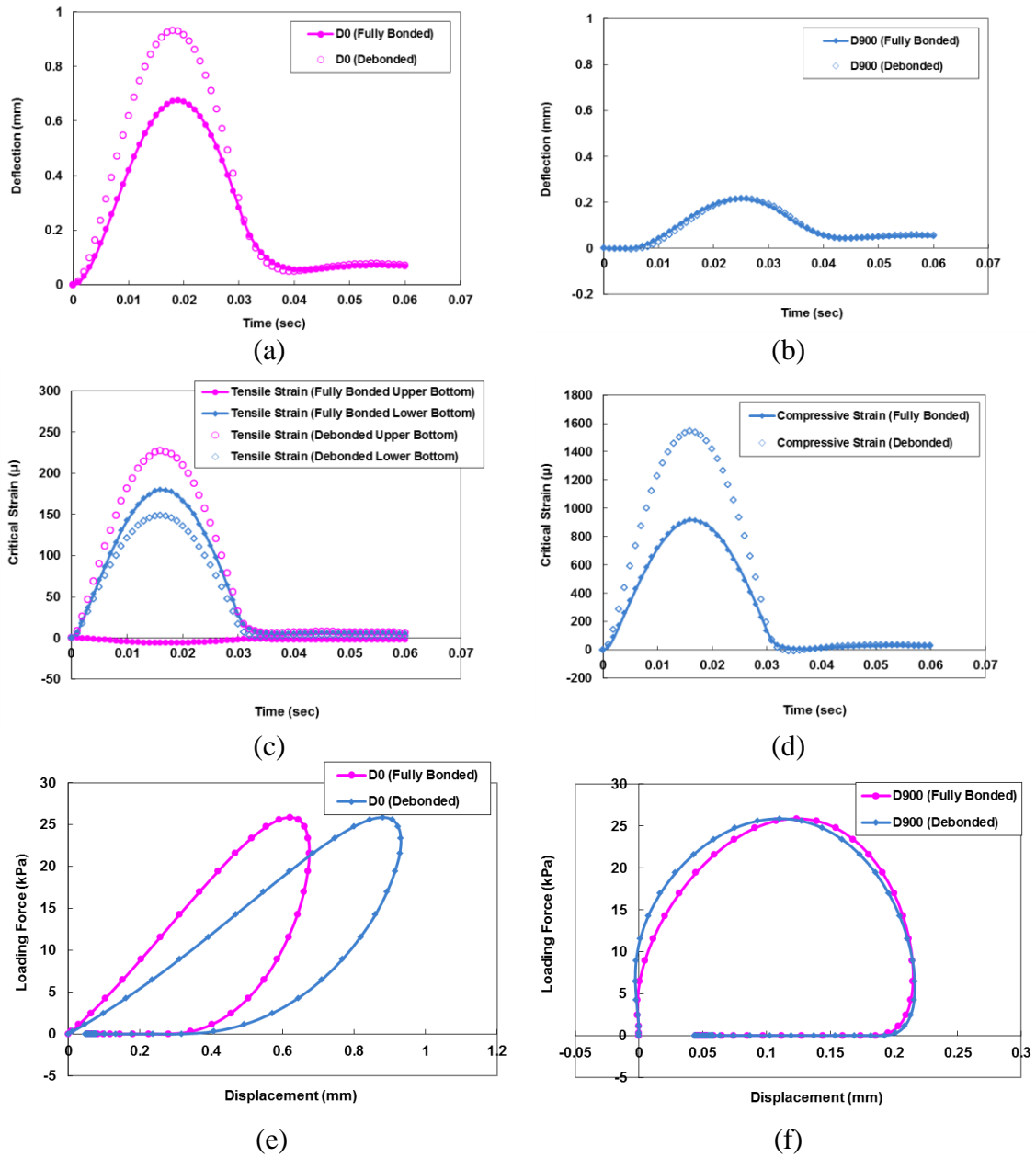


Figure 3.9 Effects of layer delamination on (a) D0-time history; (b) D900-time history; (c) tensile strain-time history; (d) compressive strain-time history; (e) hysteresis loop of D0; and (f) hysteresis loop of D900

### 3.3.6 Effect of Unbound Material Nonlinearity

Figure 3.10 and Figure 3.11 show the comparison of different unbound material models through the deflections and critical strains as well as hysteresis loops of D0 and D900. In the reference case, the linear elastic moduli for both base aggregate layer and subgrade were calculated as the average moduli from the modulus distribution throughout the base layer and subgrade, respectively. As shown in Figures 3.10 (a) and (b), the linear and nonlinear isotropic models for base aggregate underestimated the deflections and critical strains in comparison to the nonlinear cross-anisotropic model. This trend is similar for the effect of nonlinear subgrade model, as shown in Figures 3.11 (a) and (b). Therefore, it is concluded that ignoring the nonlinearity of the unbound materials can lead to adverse effects on the modulus back-calculation and pavement performance assessment.

Figures 3.10 and Figures 3.11 (c) and (d) present the hysteresis loops using different unbound material models in terms of D0 and D900. The dissipated energy of D0 and D900 in the linear model is the lowest in general. It was found that the dissipated energy of D0 was mainly affected by the nonlinear model of aggregate base; while the dissipated energy of D900 was mainly affected by the nonlinear model of subgrade. Therefore, the linearity assumption for both unbound materials might result in obvious error if energy dissipation is used as an analysis indicator.

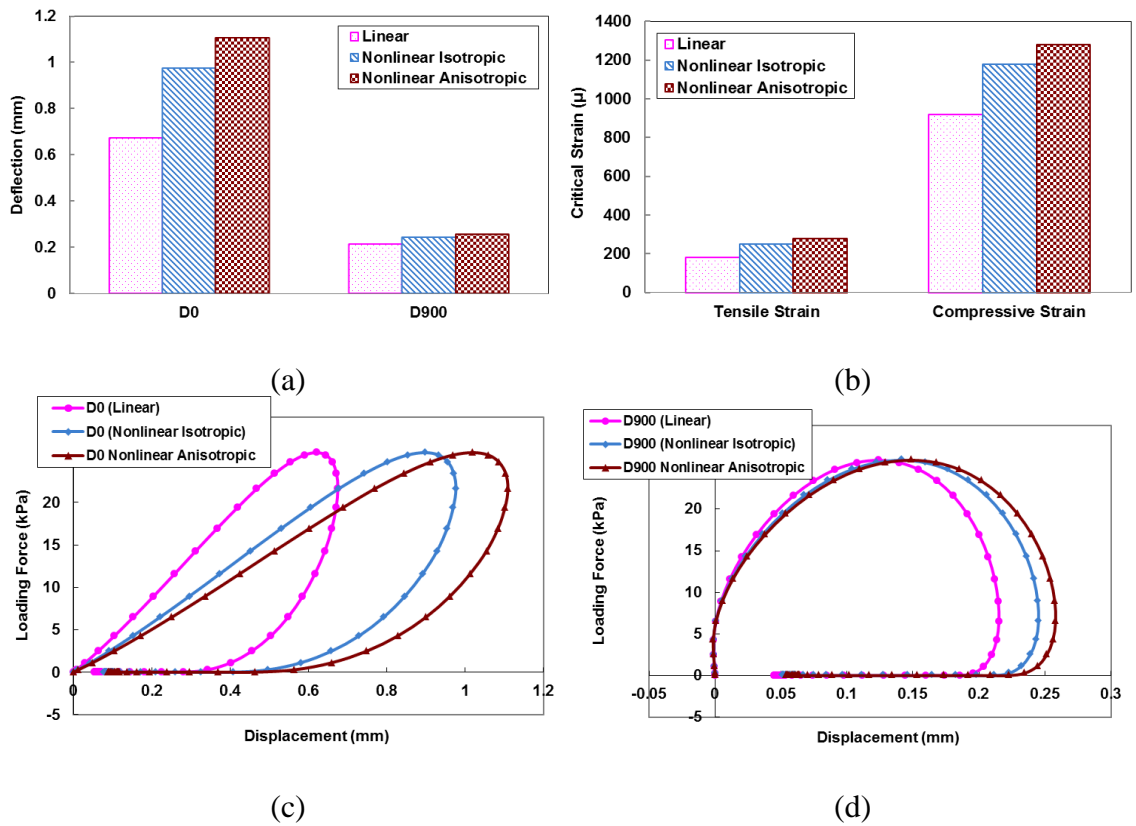


Figure 3.10 Effect of nonlinear model of aggregate base on (a) D0 and D900; (b) critical strains; (c) hysteresis loop of D0; and (d) hysteresis loop of D900

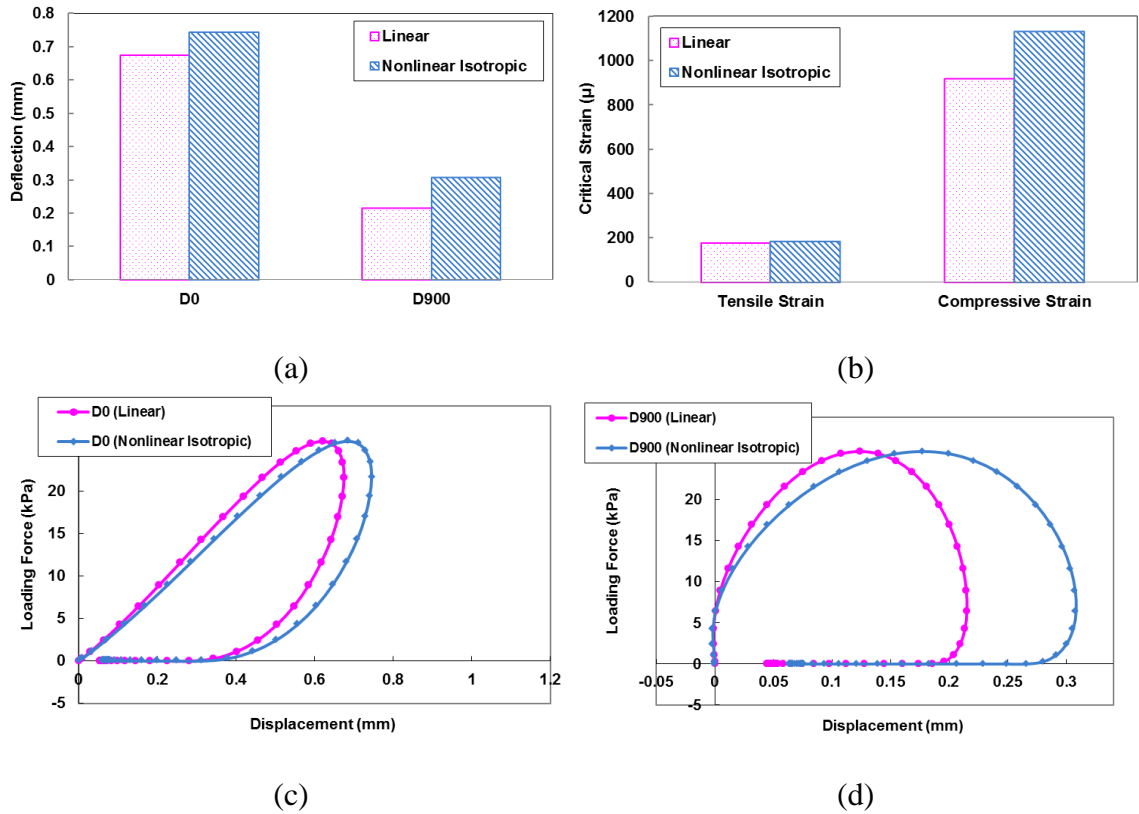


Figure 3.11 Effect of nonlinear model of subgrade on (a) D0 and D900; (b) critical strains; (c) hysteresis loop of D0; and (d) hysteresis loop of D900

In order to investigate the stress-dependent behavior of unbound material, multiple loading levels were considered in the FE analysis. The stiffness sensitivity analysis to the loading levels was conducted using the ratio of loading to deflection (D0 and D900), as shown in Figure 3.12. This ratio would be equal to one if the linear material properties are used in the FE model. The positive slope indicates that the nonlinear stress hardening behavior is dominant, while the negative slope indicates that the stress softening behavior of subgrade is dominant. However, the negative slope explains the stress softening behavior in the subgrade. The results indicate that D0 is equally affected by the nonlinearity in base layer and subgrade. However, D900 is mainly governed by the nonlinearity in subgrade that shows significant stress-softening behavior.

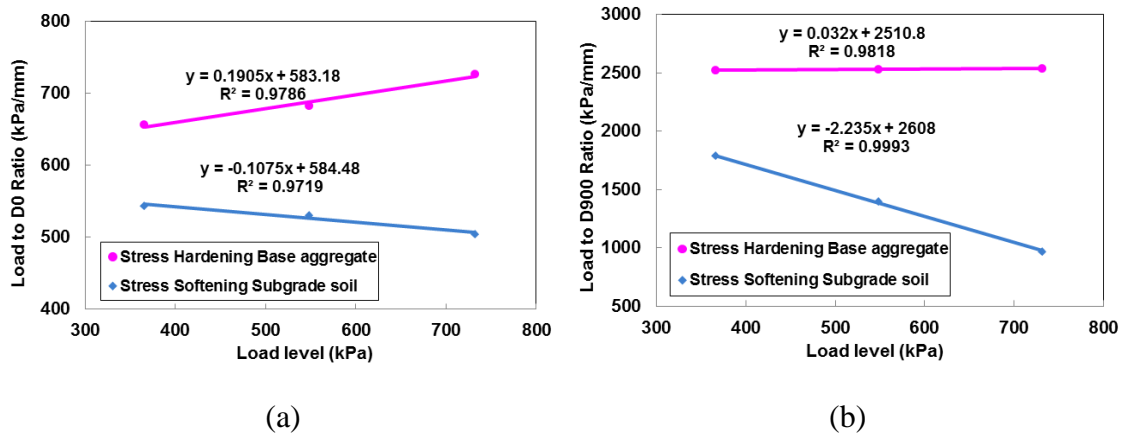


Figure 3.12 FWD deflection variations under multiple loadings considering nonlinear unbound material for (a) D0 and (b) D900

### 3.3.7 Effect of Bedrock Depth

Figure 3.13 shows effect of stiff layer (bedrock) underlying subgrade on surface deflections through the deflection-time histories and the sensitivity of D0 and D900 to the depth to bedrock. The selected stiffness of bedrock is based on typical rock properties with an elastic modulus of 7000 MPa and a Poisson's ratio of 0.2. As shown in Figures 3.13 (a) and (b), deflection-time histories of D0 and D900 sharply decreased if the bedrock exists at the depth of 3000 mm from pavement surface. It is noted that the variations of strain-time histories for tensile and compressive strains are insignificant (difference smaller than 3%); therefore they were not plotted here due to the reason of brevity. It indicates that the existence of bedrock casts more effect on the back-calculation of layer moduli through FWD deflections than on the assessment of pavement performance through critical strains.

Figures 3.13 (c) and (d) show the sensitivity of D0 and D900 to the depth to bedrock. It shows that the D0 is increased gradually as the location bedrock becomes deeper; and the variation of the D0 becomes stable (variation smaller than 5%) as the depth goes beyond 8000 mm from pavement surface. However, the stability for the D900 variation was not obtained until the depth reached to 10000 mm. Given that the bedrock is closer to



and then has more effect on the subgrade behavior, this helps explain that the D900 is more sensitive than the D0 to the change in the depth to bedrock. The threshold range of 8000 mm and 10000 mm obtained from the sensitivity analysis were consistent with previous findings using field measured deflections (Mera 1995; Broutin 2010).

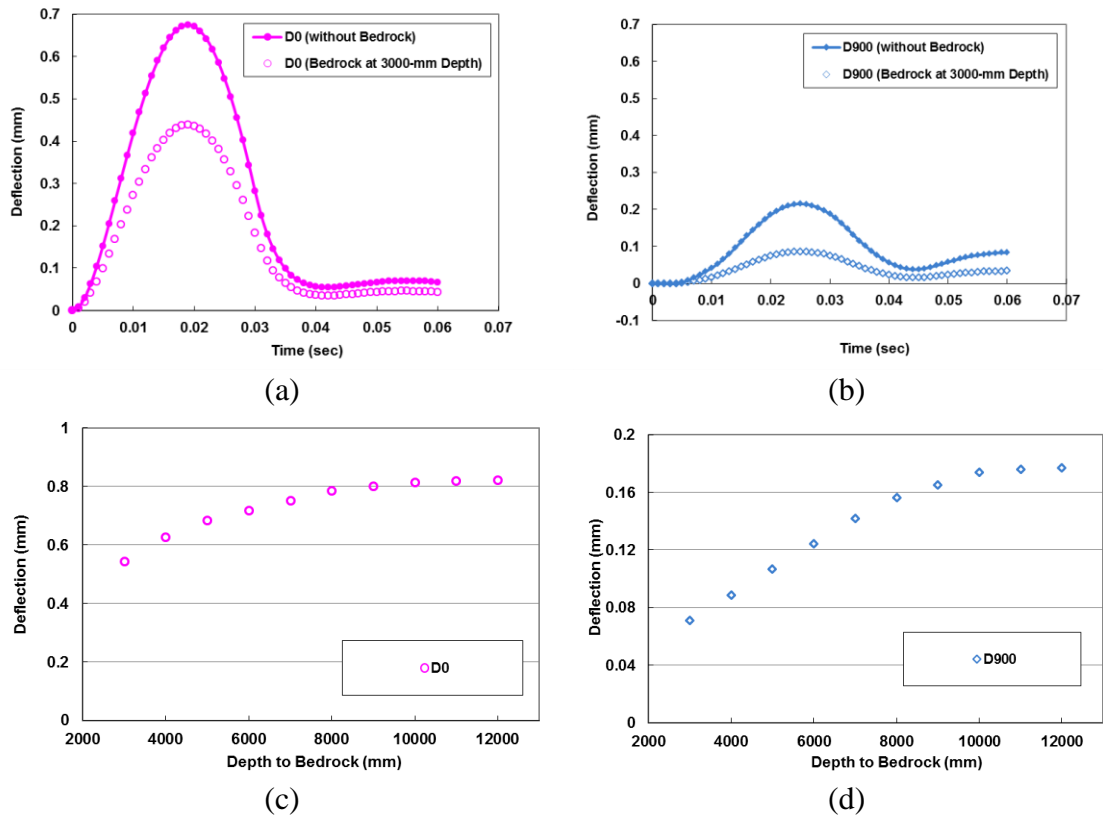


Figure 3.13 Effects of bedrock on FWD deflections for (a) D0-time history; (b) D900-time history; (c) sensitivity of D0 to the depth to bedrock; and (d) sensitivity of D900 to the depth to bedrock

### 3.4 Summary

In this study, finite element modeling is used to simulate impulsive loading on the multi-layered pavement system and analyze the primary factors affecting analysis results, including dynamic analysis, temperature gradient, bedrock depth, asphalt layer

delamination, viscoelasticity of asphalt layer, and nonlinearity of unbound materials. The developed axisymmetric FE models successfully capture the distinctive constitutive model for each pavement layer and the interaction between different layers and boundary conditions.

The dynamic analysis causes the greater time lag and magnitude of deflection-time history as well as more energy dissipation, as compared to quasi-static analysis. The assumption of elastic asphalt layer may underestimate or overestimate pavement responses, depending on the selection of loading frequency; therefore, it cannot capture the frequency-dependent response of viscoelastic material. Similarly, ignoring the nonlinearity of the unbound materials can lead to adverse effects on the modulus back-calculation and pavement performance assessment.

The effect of nonlinear temperature gradient on surface deflections and critical strains becomes significant at the high temperature. The delamination in asphalt layer can induce the greater surface deflections at loading center and critical strains in the pavement. The stiff layer underlying subgrade can significantly affect back-calculation of layer moduli through FWD deflections. A threshold range of 8000 mm and 10000 mm was found for neglecting the effect of bedrock.

With the proper development of finite element models, further research will be conducted for back-calculation of layer moduli using the combination of synthetic database from forward FEM analysis and artificial intelligence techniques.

## **CHAPTER 4 BACKCALCULATION OF PAVEMENT MODULI USING AN ANN-GA MODEL**

### **4.1 Backcalculation of Pavement Layer Properties**

#### *4.1.1 Overview of The Soft Computing-based Process*

An Artificial Neural Network (ANN)-based backcalculating program combined with a Genetic Algorithm (GA) optimization algorithm was developed for backcalculation of layer moduli from Falling Weight Deflectometer (FWD) testing. Axisymmetric finite element (FE) models were developed considering dynamic loading of FWD drops and viscoelastic and nonlinear material parameters for pavement layers. The FE models were used to generate the synthetic database that covers the variations in material parameters, pavement structures, temperatures, and loading levels. The ANN-GA program was trained and verified using the synthetic database. The accuracy of backcalculation was evaluated with measured data from two field testing sections. The ANN-GA program was found having acceptable accuracy through the verification and validation processes. The input variables of the ANN-GA program are available from FWD testing including the deflections at different offsets, layer thicknesses, loading magnitudes, and air and surface temperatures. The ANN-GA possesses some advantages over traditional iteration-based backcalculating program such as the elimination of seed moduli and consideration of complex material properties. More importantly, the backcalculated pavement layer parameters can be directly used for M-E design of pavement overlays. A broader synthetic database should be incorporated into the training process to enhance the interpolating capability of the ANN-GA program. In addition, deflection-time history parameters may be considered as inputs in the future work to limit the variation of viscoelastic parameters of asphalt layer.

#### *4.1.2 Development of Synthetic Deflection Database*

The developed FE models were utilized to generate an assembled synthetic database for training of the ANN-GA program. The matrix of input variables for the FE model is summarized in Table 4.1. The ranges of the variables are based on previous studies and selected to be applicable for typical flexible pavements with granular base. The master curve of dynamic modulus and temperature shift factors were obtained from the prediction model that was developed from the LTPP study using the asphalt binder type and air void content (Kim et al. 2011). The considered asphalt binder types include PG 52-22, PG 64-22, and PG 76-22. The range of air voids considered is 4%, 5%, and 6%. The material parameters for base aggregate and soil subgrade were obtained from the laboratory-developed empirical equations that related the physical properties of unbound material to nonlinear modulus parameters (George 2004; Xiao and Tutumluer 2012; Wang and Li 2015). The total number of cases is 10,368 for the range of material parameters considered in this study.

Table 4.1 Matrix of Input Variables for the FWD Synthetic Database

Category	Variable	Range
FWD Loading	Load Level (kN)	26.7~53.3
Temperature	Air Temperature (°C)	9.2~30.4
	Surface Temperature (°C)	14~46
Asphalt Layer	Layer Thickness (mm)	102~203
	Asphalt Binder (PG)	52-22~76-22
	Sigmoidal Curve Parameter $c_1$	2.90~3.92
	Sigmoidal Curve Parameter $c_2$	2.69~3.91
	Sigmoidal Curve Parameter $c_3$	-1.74~-0.65
	Sigmoidal Curve Parameter $c_4$	0.33~0.52
	WLF Function Parameter $C_1$	11.59~49.30
	WLF Function Parameter $C_2$	62.35~364.17
	Poisson's ratio	0.35
Aggregate Base Layer	Layer Thickness (mm)	203~406
	Non-linear Parameter $k_1$	1.061~3.115
	Non-linear Parameter $k_2$	0.132~0740
	Non-linear Parameter $k_3$	-2.970~-0.597
	Poisson's ratio	0.35
Subgrade	Non-linear Parameter $k_1$	0.71~1.015
	Non-linear Parameter $k_2$	0.281~0.456
	Non-linear Parameter $k_3$	-1.704~-1.192
	Poisson's ratio	0.40

## 4.2 Development of ANN-GA Program

### 4.2.1 Overview of ANN Architecture

Artificial Neural Network (ANN) is naturally utilized for collecting information to generate computational models resembling human mind, because it is capable of searching the most approximate solutions to nonlinear problems for arbitrary input and output variables. As shown in Figure 4.1, a typical feed-forward neural network structure with multilayer is comprised of input layer, hidden layers, and output layer. The integral element among all layers is the unit denoted as neuron. The individual neuron is primarily employed in each layer to execute the transfer functions, as shown in Equation 4-1. The transfer function builds on the weights and biases to implicitly connect information in the feed-forward procedure from inputs to outputs. Meanwhile, an error

backpropagation mechanism takes place, whereby the neural network can update the weights and biases from outputs to inputs via performance functions such as Root Mean Square Error (RMSE) and Gradient Descent, as shown in Equation 4-2 and 4-3.

$$a = f(\sum (w_i p_i + b)) \quad (4-1)$$

Where,

$a$  is scalar output of individual neuron;

$p_i$  is scalar input of individual neuron;

$b$  is scalar bias; and

$w_i$  is scalar weight.

$$y_{rms} = \sqrt{\frac{1}{n} \sum (\frac{y_i - y_m}{y_m})^2} \quad (4-2)$$

Where,

$y_{rms}$  is root mean square error (RMSE) between calculated and measured results;

$y_i$  is calculated results;

$y_m$  is measured results; and

$n$  is number of measured points.

$$x_{k+1}^I = x_k^I - \alpha_k g_k^I \quad (4-3)$$

Where,

$x_k^I$  is a vector of current weights and biases as shown in Equation 4-1;

$x_{k+1}^I$  is a vector of weights and biases right after the current ones;

$g_k^I$  is current gradient; and

$\alpha_k$  is learning rate.

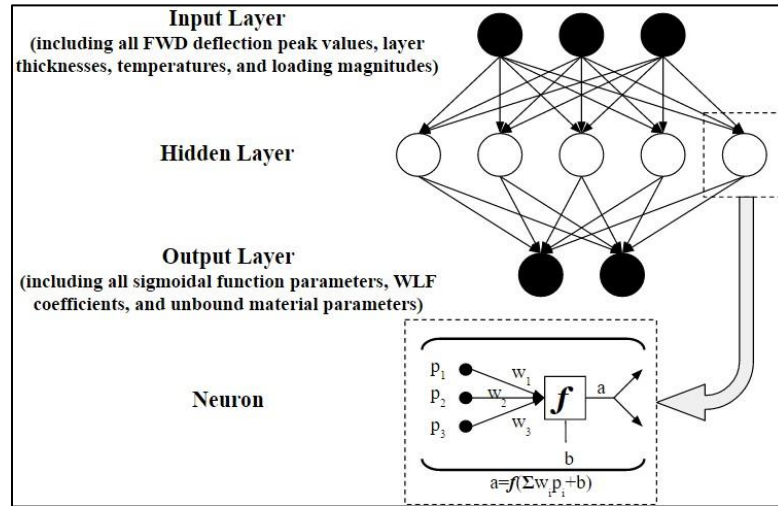


Figure 4.1 Layered structure of feed-forward ANN model

Before the application of the ANN procedure, a training process is needed to use a synthetic database to train the weights and biases in the constructed ANN model. The training process has three steps to fulfill the fitting procedure. The first step is to determine the number of working layers. The neural network contains at least three layers: one input layer, one hidden layer, and one output layer. The number of hidden layers can vary to adjust and enhance the learning capacity of the neural network. Previous study has showed that one hidden layer is applicable to establish a robust neural network to predict material parameters from FWD deflections (Meier 1995).

The next step is to set up the number of neurons in each layer. The number of neurons in the input and output layer in this study are in accordance with the number of FWD deflection inputs and the number of layer material parameter outputs, respectively. A twenty-neuron hidden layer was chosen here on basis of trial process and the recommendations from previous studies (Meier 1995; Gopalakrishnan et al. 2014).

The third step includes selecting transfer functions and configuring operational parameters in the ANN model. In this part, the transfer functions for the input layer include a log-sigmoid curve to scale the input range into  $[0, 1]$ , then a linear function to linearly map the transferred input to the data in the hidden layer, and finally a tan-

sigmoid function to generate the pre-output data into the range of  $[-1, 1]$ . The performance function parameters were set herein as  $10^{-3}$  and  $10^{-5}$  for RMSE and Gradient Descent, respectively. The training epoch for the number of iterations was limited to no more than 2000 and the learning rate was set as 0.1. Other setting parameters for the ANN remained as defaults in the MATLAB and can be found elsewhere for details (Beale et al. 2015).

#### *4.2.2 Outline of Genetic Algorithm Process*

Genetic Algorithms (GAs) are originally derived from the evolutionary algorithms which mimic the key procedure in the nature and dominate the evolution of species on the earth. GAs can perform as a searching technique to help prevent problem-solving program from dropping into local minima. It has advantages over traditional optimization tools such as less error, unique solution, and high efficiency (Goldberg 1989).

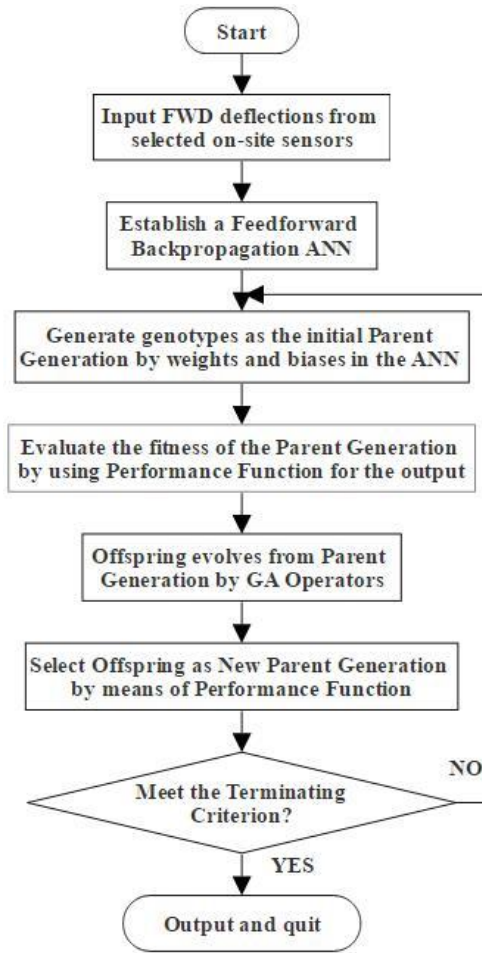
The GAs is used to facilitate the ANN structure to better map the FWD deflection inputs to the outputs of layer material parameter. The GA operation was implemented on the weights and biases from the ANN process. Figure 4.2 (a) shows the flowchart of the developed ANN-GA program. The first parent generation of weights and biases is directly created from the established ANN process. And then the evolution of the first parent generation can produce the first offspring generation through operators of GAs. The fitness evaluation by means of the performance function is capable of helping select the second parent generation out of both the first parent and offspring generations. At the end of each process of one generation, the formed offspring pool will be evaluated by the terminating criteria such as condition of improvement and number of iterations.

The schematic of cross-over and mutation of data string in the GA is illustrated in Figure 4.2 (b). The primary operators are grouped as initialization, evaluation, selection, cross-over, and mutation. It is worth mentioning that the GAs can take effect in population of solutions rather than in a single one. For example, the parameters in the

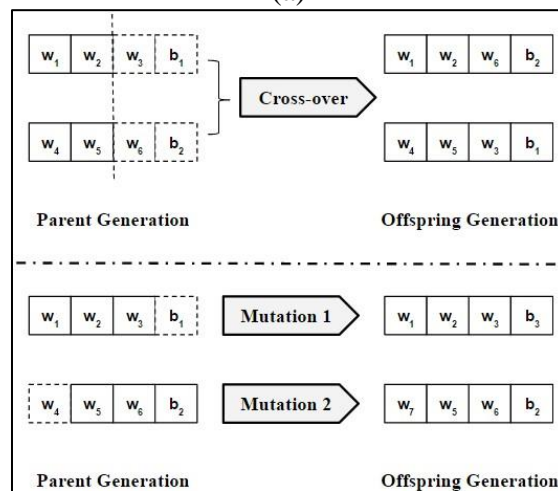


performance function of ANN model can be employed to sufficiently process the fitness evaluation for the offspring selection.

To fulfill the GA process, the first data string was randomly initiated as parent generation. This step has no effect on the final result by GAs (Fwa et al. 1997). In the second step, after the operators of cross-over and mutation, the fitness evaluation is implemented to the generated offspring pool by means of the performance function. The selection in the third step is processed according to fitness results to screen the offspring to form the new parent generation. The three-step GA process keeps repeated until the pre-set terminating criterion is obtained. In this study, the convergence condition for the estimated parameters was  $10^{-3}$ ; and the cross-over and mutation operations were 0.85 and 0.15 (Fwa et al. 1997). The number of generations in the GA process was 50, which means that after the 50 generations the GA process is automatically terminated.



(a)



(b)

Figure 4.2 (a) Flowchart of ANN-GA program and (b) GA operators

### 4.3 Training and Verification of ANN-GA Program

After the initial development of the ANN-GA program, a training process with a large volume of data was needed to determine model parameters. As mentioned before, the synthetic database was built using the forward calculation of FE model. The peak values of FWD deflections at different offsets, loading magnitudes (drop load), hysteresis loop (load-displacement curve) indicators, pavement structure parameters (asphalt and unbound layer thickness), and temperatures (air temperature and pavement surface temperature) served as the inputs of the ANN-GA program.

In order to better backcalculate the viscoelastic parameters and the WLF parameters of time-temperature shift factor for asphalt surface layer, the hysteresis loop formed by the load-displacement curve was used as pavement response inputs in addition to the peak deflection values. The hysteresis loop can capture the effect of viscoelasticity on pavement surface deflections, because it represents the energy dissipation in FWD test as the drop load does the work with the displacement at pavement surface. The pavement deflection at loading center was used for hysteresis loop analysis since it is affected by the composite modulus of pavement layers including the viscoelastic asphalt surface layer. Figure 4.3 (a) shows the time history processes of FWD load and the deflection at loading center. Figure 4.3 (b) shows the hysteresis loop characterized by three shape indicators, namely the slope of major axis ( $k$ ), the length of major axis ( $m$ ), and the length of minor axis ( $n$ ). The major axis is defined as material stiffness, while the minor axis is defined as energy dissipation.

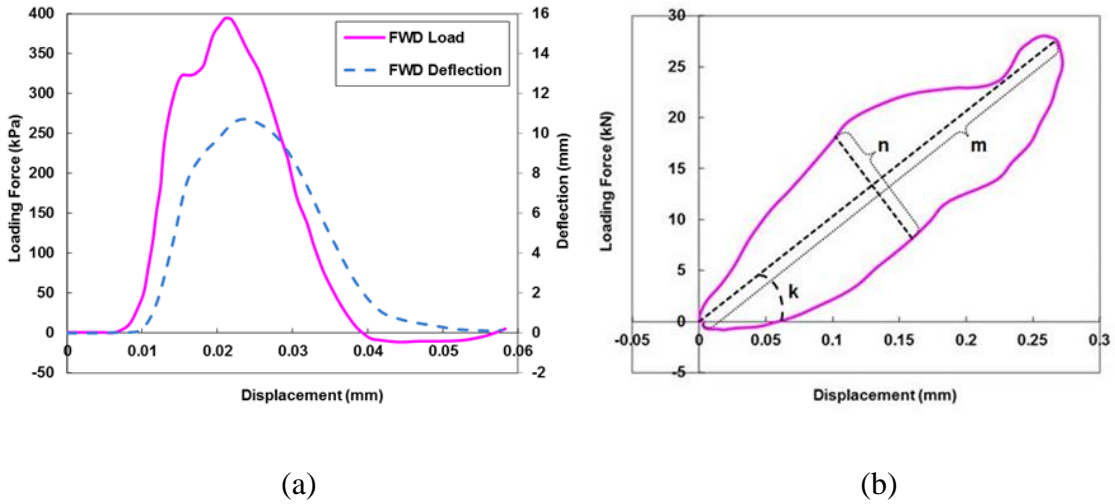


Figure 4.3 Illustration of hysteresis loop (load-displacement curve): (a) FWD load and displacement; and (b) three shape indicators

On the other hand, the material parameters of each pavement layer were backcalculation outputs. Therefore, the number of neurons of the input layer is 17; and the number of outputs is 12 for asphalt surface layer, granular base layer, and subgrade. It is noted that the output of dynamic modulus from the ANN-GA program is the modulus master curve at 21°C, since this is the reference temperature used in the FE models. However, the calculated WLF parameters can be used to obtain the time-temperature shift factor and dynamic modulus at any temperature. Therefore, the ANN-GA program is able to backcalculate viscoelastic parameters of asphalt layer and nonlinear parameters of unbound layers.

In the synthetic database, 85% of the data were selected for training of ANN-GA program, while the remaining 15% for model verification. In the training process, the initial 85% was of importance to build up the ANN architecture to shape the original weights and biases as the first generation for GA process. The remaining 15% was used to verify the soundness of the established ANN structure by means of GA process. Therefore, the 15% of the data used for verification were not employed in the training process for the purpose of independent check.

Figure 4.4 shows the calculated results in the verification process as compared to the original inputs in the synthetic database, respectively, for the sigmoidal curve parameters (21°C), the WLF function factors of asphalt layer, and the non-linear material parameters of the base layer and subgrade. The results show that the calculated results match well with the synthetic parameters. Although some outliers are found around the reference fitting line, the regression coefficients for Figures 4.4 (a), (b), (c), and (d) are as high as more than 0.96. It indicates that the training of ANN-GA program is successful.

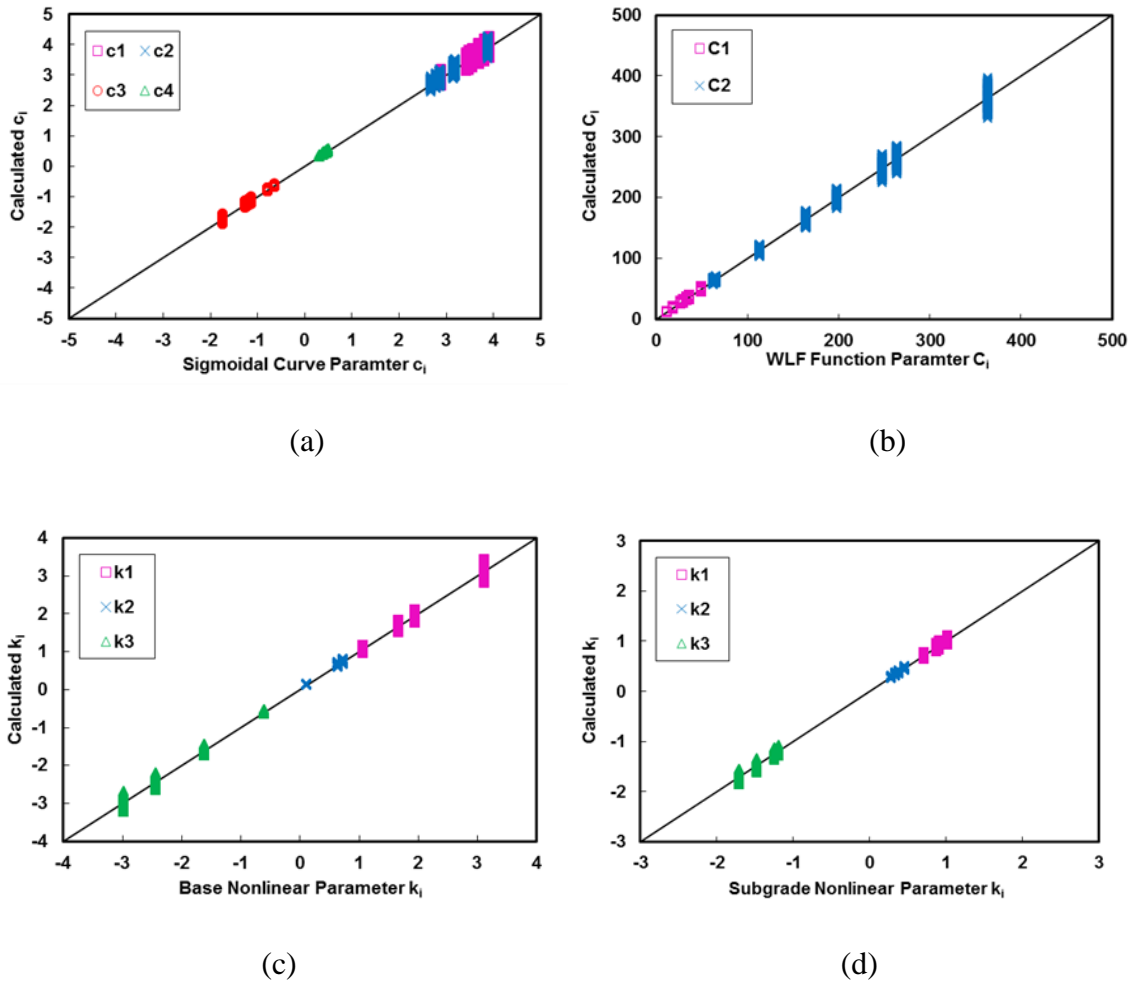


Figure 4.4 Comparison of outputs ANN-GAA program to synthetic database inputs for (a) sigmoidal curve parameters (21°C); (b) WLF shift factors of asphalt layer; (c) base layer material parameters; and (d) subgrade material parameters

## 4.4 Validation of ANN-GA Program using Field Testing Data

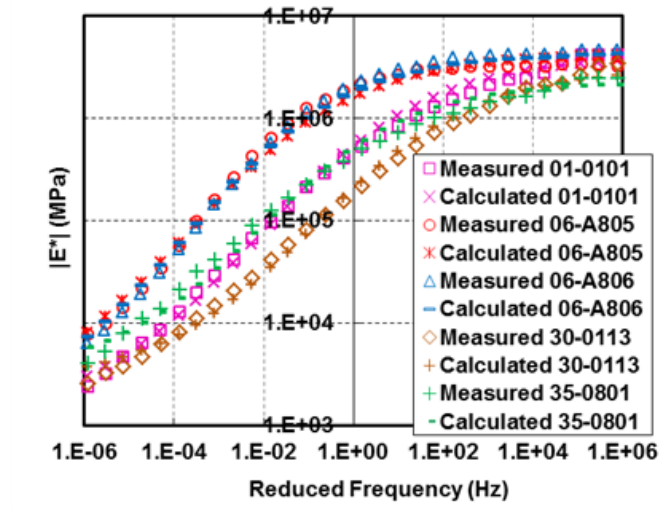
### 4.4.1 Field Testing Sections for Validation

To validate the ANN-GA program with field data, five pavement sections from different projects were used. The sections were completely selected from the Long-Term Pavement Performance (LTPP) database (State 01, Section 0101; State 06, Section A805;

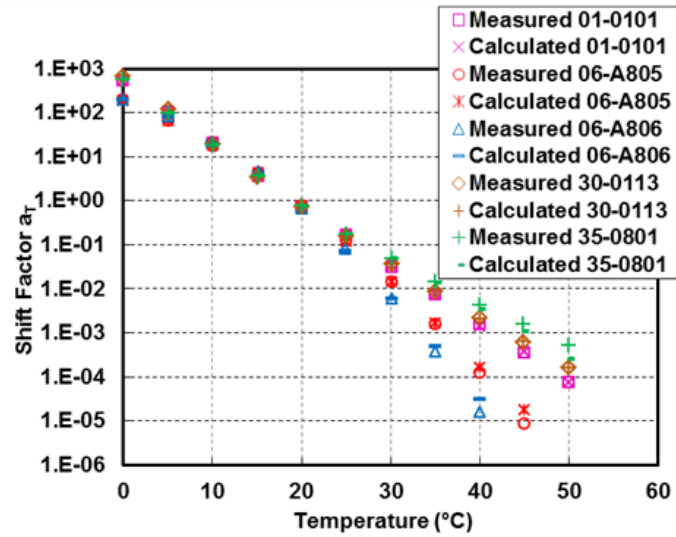
State 06, Section A806; State 30, Section 0113; State 35, Section 0801;), which were conventionally or equivalently three-layer flexible pavement structures (FHWA 2016). The thicknesses of asphalt layer were 107~188mm, and the thicknesses of aggregate base layer were 201~307mm. The FWD test was conducted under the load of 26.7~53.3kN. The depth of subgrade was assumed infinite since there is no bedrock in the shallow depth. Temperature profiles were recorded in terms of air and surface temperatures during FWD test. The range of air temperatures is 14.2~19.4°C and the range of pavement surface temperature is 18.4~37.8°C. From the recorded information in LTPP database, this section was considered with no rehabilitation between the specified two consecutive years and was in good service condition. The dynamic modulus with WLF factors were originally obtained as creep compliance from field cores and then were converted to dynamic modulus (Chatti et al. 2003). The validation focused on viscoelastic material properties of asphalt layer due to the lack of data for unbound material layers.

#### *4.4.2 Validation of Backcalculation Results*

Figure 4.5 shows the comparison of outputs from the ANN-GA program to measured material properties from the LTPP database. The reference temperature was 19°C, so the backcalculated dynamic modulus in the original outputs (at reference temperature of 21°C) was shifted accordingly. It can be seen from Figure 4.5 (a) that the calculated and measured master curves of dynamic modulus have acceptable agreements, although the accuracy decrease a little bit in the range of low frequency. Figure 4.5 (b) shows that the calculated time-temperature shift factors match well with the measured ones as temperatures is below 45°C. The discrepancy is because the temperature considered in the synthetic database does not cover the high temperature ranges, which will be considered in the future work.



(a)



(b)

Figure 4.5 Comparison of outputs from ANN-GA program with measured data from LTPP database by (a) dynamic moduli and (b) WLF function parameters for time-temperature shift factor



To further validate the ANN-GA program, the measured FWD deflections in the field sections were compared to the calculated deflections using FE models and the backcalculated material parameters, as shown in Figure 4.6. As mentioned before, the selected five pavement sections have different layer thicknesses, temperature profiles, and loading magnitudes. The comparison results confirm the consistence and accuracy of the ANN-GA program. The root mean square error (RMSE) and mean absolute error (MAE) were calculated using Equation 4-4 and 4-5. The results show that the RMSE is 0.01mm and the MAE is 0.008mm. This indicates that the calculated FWD deflections have acceptably small discrepancies from the measurements.

$$\text{RMSE: } y_{mse} = \sqrt{\frac{1}{n} \sum (y_i - y_m)^2} \quad (4-4)$$

$$\text{MAE: } y_{mae} = \frac{1}{n} \sum |y_i - y_m| \quad (4-5)$$

Where,

$y_{rms}$  is root mean square error between calculated and measured results;

$y_{mae}$  is mean absolute error between calculated and measured results;

$y_i$  is calculated results;

$y_m$  is measured results; and

$n$  is number of measured points.

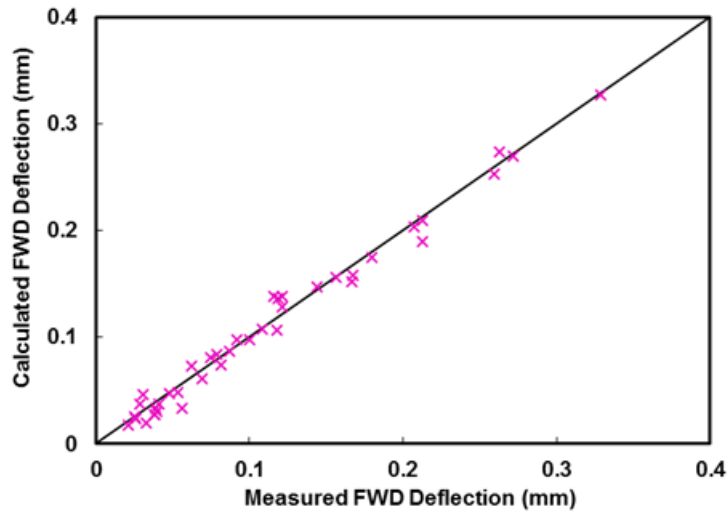


Figure 4.6 Comparison of measured and calculated deflections using the backcalculated material parameters for LTPP sections

## 4.5 Assessment of Asphalt Material Deterioration

### 4.5.1 Field Sections from LTPP Database

On-site measured FWD deflections and laboratory-tested layer material parameters were taken into consideration in the validation of the ANN-GA Program. Previously five pavement sections were selected from the LTPP database. Good agreements were found between predicted and tested material parameters of asphalt layers. However, unbound material parameters were not rather available for those selected pavement sections. Therefore, more unbound layer properties were still in need of validation against the filed data.

To validate the ANN-GA program with field data from AC to unbound material parameters, nine pavement sections from the LTPP program were used in this study from the Seasonal Monitoring Program (SMP) of LTPP database. The primary information for those pavement sections was summarized in Table 4.2, which were basically or equivalently three-layer asphalt pavement structures (Yau and Von Quintus 2002). As shown in Table 4.2, the thicknesses of asphalt layer are 81~277mm, and the thicknesses

of base or subbase layer are 51~668mm. The FWD testing was conducted under the loading magnitudes of 26.7~71.2kN. The air and surface temperatures were recorded during FWD testing, and their ranges are 3.6~35.8°C and 5.7~53°C, respectively. Those pavement sections were known without rehabilitation during the selected time periods when FWD testing was conducted. The dynamic moduli were converted from the creep compliance that were measured using field cores taken from the pavement sections based on inter-conversion theory of linear viscoelasticity (Park and Schapery 1999).

Table 4.2 LTPP On-site Testing Pavement Layer Thickness

State No.	State	Section ID	AC (mm)	Base(mm)	Subbase (mm)
27	MN	1018	112	132	/
27	MN	6251	188	259	/
28	MS	1016	195	525	/
28	MS	1802	220	51	/
35	NM	1112	160	152	/
48	TX	1068	277	152	203
48	TX	1077	130	264	/
48	TX	1122	81	396	213
87	ON	1622	135	168	668

The time history of FWD deflections is shown in Figure 4.7, expressed in terms of load-displacement curves. As verified in previous study, the hysteresis loop was an effective input in the ANN-GA program along with deflection peak values to better capture the viscoelasticity of asphalt layer. It considers energy dissipation of pavement while the FWD loading drops on pavement surface. Only the pavement deflections at loading center ( $D_0$ ) were utilized for analysis of hysteresis loop because  $D_0$  was affected by the stiffness combination of pavement layers especially the asphalt surface layer.

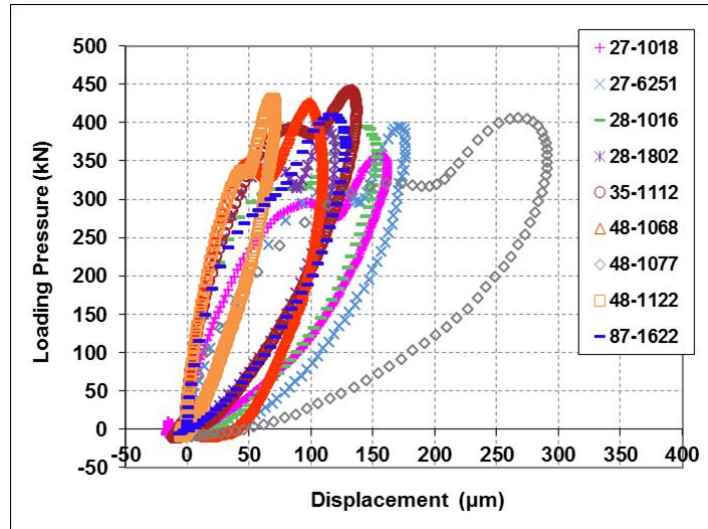


Figure 4.7 FWD deflections in hysteresis loop from LTPP program database

#### 4.5.2 ANN-GA Program for Evaluation of AC Material Deterioration

The ANN-GA program was modified in particular to predict layer parameters of existing asphalt pavement, rather than just the undamaged one, by inputting into the program pavement variables including peak deflections at different offsets, shape factors of hysteresis loop, layer thicknesses, loading magnitudes, and air and surface temperatures, as shown in Figure 4.8. In this part, a typical three-layer ANN architecture with feed-forward backpropagation structure were generated for assessment of AC material deterioration, which was combined along with GA operators including initialization, evaluation, selection, cross-over, and mutation (Li and Wang 2017).

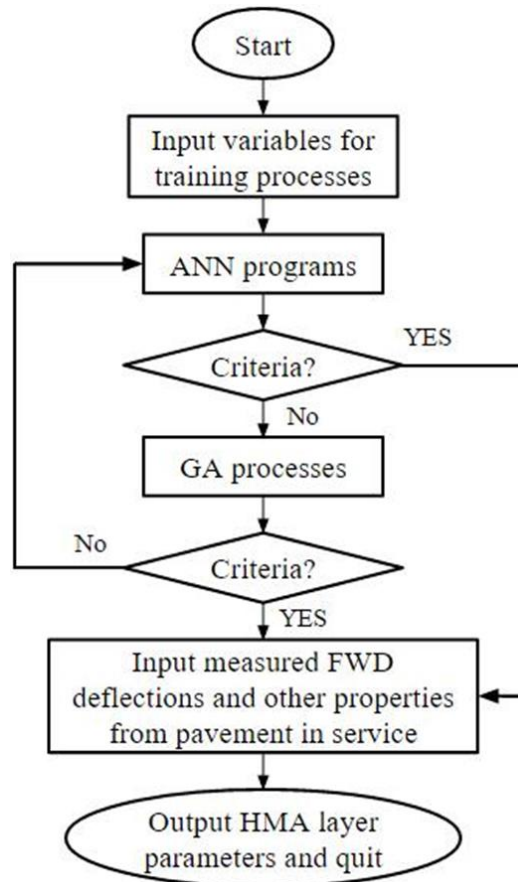


Figure 4.8 Flowchart of ANN-GA program predicting existing AC moduli

#### 4.5.3 Extensive Validation of ANN-GA Program

The extensive validation on the pavement sections was conducted in this paper for backcalculating viscoelastic material properties via the ANN-GA program, as shown in Figures 4.9. The backcalculated dynamic modulus was shifted to the reference temperature of 21°C. Two predictive approaches were applied in this study in the validation process. The first one was to synchronically backcalculate material properties of asphalt layer and granular base layer, while the second approach was to independently run the backcalculation for material parameters of each layer. This two-fold validating procedure was utilized to evaluate the soundness and robustness of the ANN-GA program.

As shown in Figure 4.9 (a) and (b), measured and calculated master curves of dynamic moduli were compared. The curves appear in sigmoidal shapes that extend horizontally as the reduced frequency approaches zero or infinity. The comparison results show good agreements between measured and calculated moduli. Meanwhile the results from the synchronic and the independent procedures have little discrepancy between each other, which indicate the accuracy and stability of the ANN-GA program. Similar findings can be found for time-temperature shift factors of dynamic moduli, as shown in in Figure 4.9 (c) and (d).

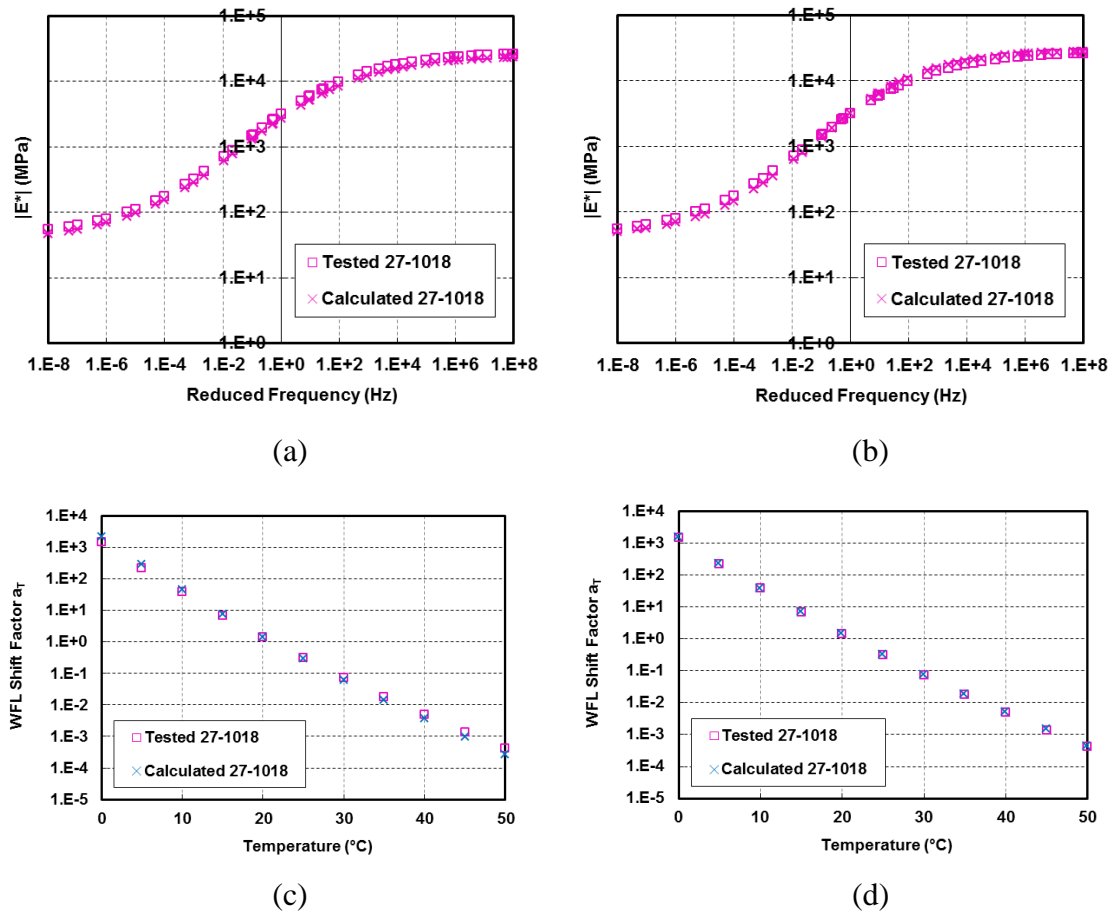


Figure 4.9 Comparison between LTPP testing and ANN-GA results in: (a) synchronically predicted dynamic moduli; (b) independently predicted dynamic moduli; (c) synchronically predicted WLF shift factor; and (d) independently predicted WLF shift factor

For simplicity reason, only the detailed results for LTPP section 27-1018 were presented here. The same level of accuracy and stability was achieved for all other LTPP sections considered in the validation. The consistency in the comparison results proves the ability of ANN-GA program in carrying out backcalculation for asphalt pavements with different materials and layer thicknesses. Therefore, the ANN-GA program can be used to further investigate material deterioration trends in asphalt layer.

To quantitatively verify the accuracy of backcalculated results by ANN-GA models, spectrum accuracy of backcalculated dynamic moduli for all sections were analyzed and shown in Figure 4.10. In general, the backcalculation can produce the sigmoidal master curve with error less than 5% in logarithmic range. As shown in Figure 4.10, less accuracy was mainly located in the low frequency zone and more accurate results were found in the high frequency area. And maximum accuracy can be spotted in around 30Hz. It means that the ANN-GA models have more accurate prediction for dynamic moduli in high frequency spectrum. This may be mainly due to the reason that the training processes were implemented with FWD deflections generated by the loading frequency of 33Hz. A proposed method can be made to prevent from dropping into the low frequency error. The training programs would be input with special FWD deflections loaded and simulated by full frequency spectra. Therefore, the predictive capacity of the ANN-GA models can be enhanced more sound and robust for the entire backcalculated sigmoidal master curve of the dynamic moduli.

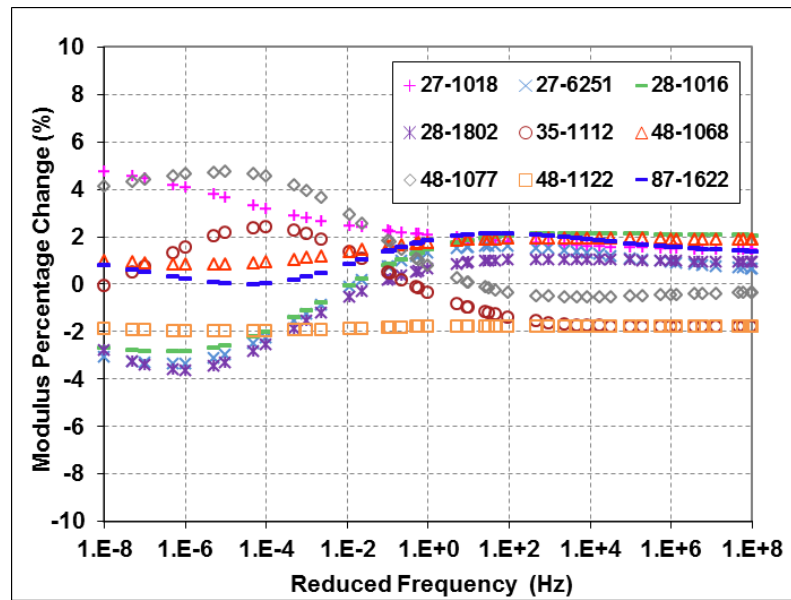


Figure 4.10 Accuracy of backcalculated dynamic moduli at different frequencies for all sections



#### 4.5.4 Backcalculation of Damaged Dynamic Modulus

The prediction of AC deterioration was dependent on measured FWD deflections at different pavement ages. For example, FWD deflections would increase as asphalt surface material deteriorated along time. To better capture the variation of the AC performance state in different time point, three phases were introduced into this study as initial stage, damaging stage, and end stage. As shown in Figure 4.11, the hysteresis loops were extracted from the same location point but different testing time indicating the varying FWD deflections. The hysteresis loop in the initial stage is similar to Figure 4.8, which is quite close to the intact state at the very beginning of service period. The damaging stage is shown as developing phase with maximum displacement increased and loop shape changed. The end stage is the end of service life before rehabilitation. It was assumed in this study that only the material properties changed throughout the specified span of time, whereas pavement structure and other material parameters stayed unchanged such as layer thickness, and Poisson's ratio.

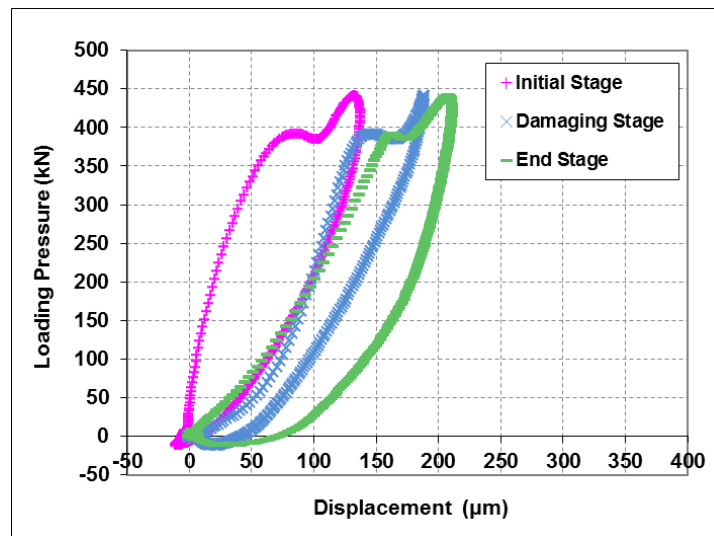


Figure 4.11 FWD hysteresis loops in different stages of pavement life

Figure 4.12 compares dynamic moduli in different stages of AC deterioration calculated by ANN-GA program. Only four sections were selected due to data

availability. Although the damaged curves by ANN-GA program (DAG) develop smoothly in sigmoidal shape and extend horizontally as the reduced frequency approaches infinity, they decrease tremendously compared to the tested curves in initial stage. Figure 4.12 (a) only has the available FWD time history in the year of 5/3/2011 after the initial stage on 7/13/04, but other three sections display a desirable three-stage deterioration of the asphalt mixture. However, enormous discrepancy is noted merely in the ranges of high frequency and little difference is observed from the low frequency zones. This is in part because the AC deterioration was mainly attributed to the damaging or aging of the AC binder instead of the AC gradation; and it was well known that AC dynamic modulus is more sensitive to binder than degradation when it comes to a loading with high frequency, and *vice versa*. This helps justify the ability of the ANN-GA program to effectively reflecting the AC damaging mechanism.

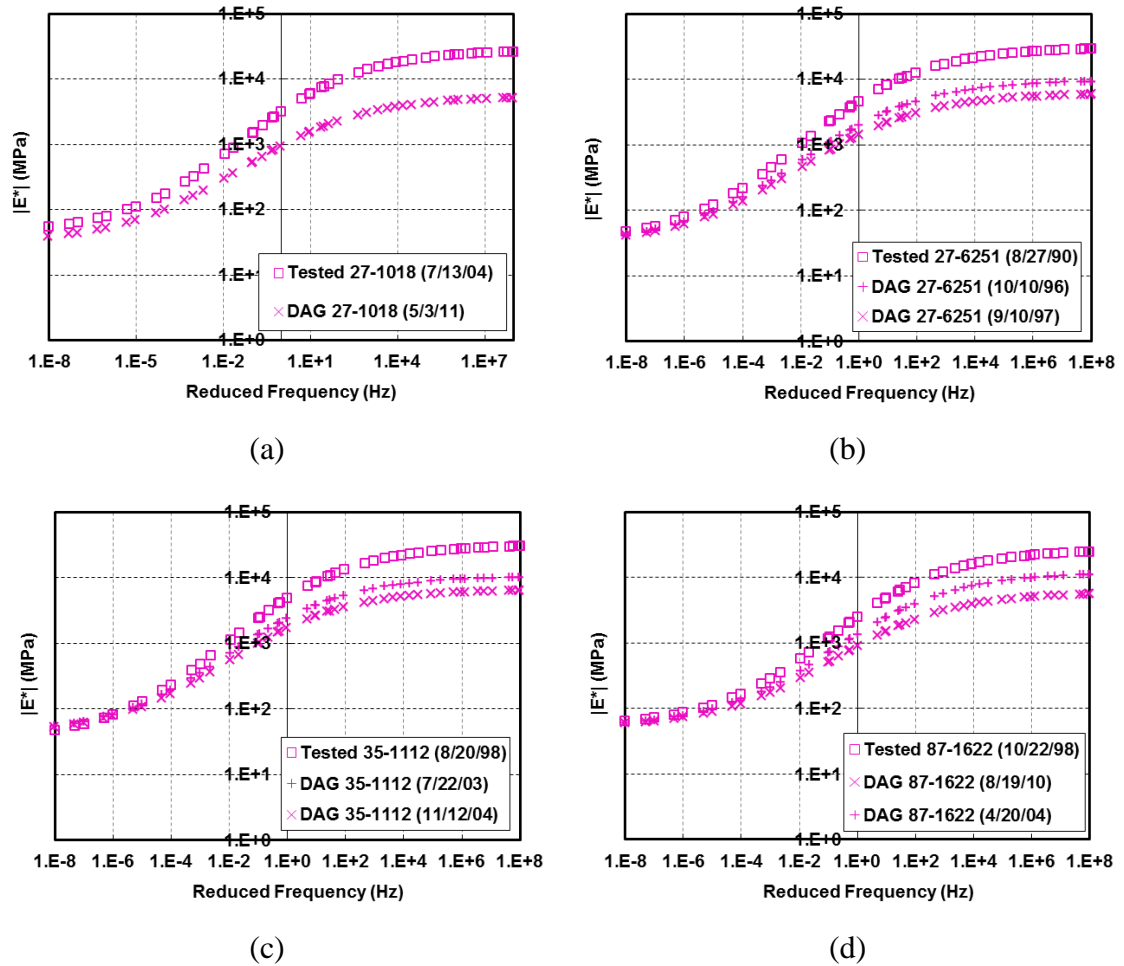


Figure 4.12 Compared dynamic moduli in different phases of AC deterioration by ANN-GA program for: (a) 27-1018; (b) 27-6251; (c) 35-1112; and (d) 87-1622

#### 4.5.5 Comparison with Damaged Modulus Model in MEPDG

To further verify the capability of ANN-GA program in predicting the damaged modulus of AC, the method used in MEPDG to estimate the asphalt mixture damage was evaluated as comparison. In the level one input of MEPDG, damaged modulus was defined as a function of damage factor in the sigmoidal function of dynamic moduli, as shown in Equation 4-6 (ARA 2004). To effectively characterize in situ AC condition in terms of existing dynamic moduli, the damage factor was defined as the ratio of FWD-

backcalculated modulus and the initial dynamic modulus at the loading frequency of FWD, as shown in Equations 4-7 and 4-8.

$$\left| E_{dam}^* \right| = 10^{c'_1} + \frac{\left| E^* \right| - 10^{c'_1}}{1 + e^{(-0.3 + 5 \times \log(d_{AC}))}} \quad (4-6)$$

Where,

$\left| E_{dam}^* \right|$  is damaged dynamic modulus, MPa;

$E_{FWD}$  is backcalculated modulus from FWD deflections;

$c'_1$  is degraded parameter for Equation 3-4 instead of  $c_1$ ; and

$d_{AC}$  is fatigue damage factor.

$$d = \frac{E_{FWD}}{\left| E^*(\omega) \right|} \quad (4-7)$$

$$c'_2 = d \times c_2 \quad (4-8)$$

Where,

$d$  is damage factor;

$E_{FWD}$  is backcalculated modulus from FWD deflections;

$\left| E^*(\omega) \right|$  is undamaged dynamic modulus at FWD loading frequency (33Hz here) at the same temperature as FWD testing; and

$c'_2$  is degraded parameter for Equation 3-4 instead of  $c_2$ .

As shown in Equation 4-6, elastic moduli were backcalculated from peak deflection values using the traditional backcalculation software, Evercalc from EVERSERIES in this study (WSDOT 2005). By conducting analysis using the MEPDG method for the damaged dynamic modulus, dynamic moduli at different stages of AC deterioration at four LTPP sections were shown in Figure 4.13. Similar to the results obtained from ANN-GA program, the reduction of modulus is more obvious in the range of high

frequency. Compared with the backcalculated dynamic moduli, the shifted dynamic moduli using MEDPG approach has slightly more discrepancy between the initial and damaged dynamic modulus in the ranges of low frequency. These discrepancies could be caused by the assumption of the damage factor in shifting the dynamic modulus curve as the MEDPG approach is used.

Overall, the MEDPG approach and the ANN-GA program predict similar trends of dynamic modulus for damaged AC. With the developed ANN-GA program, the damaged dynamic moduli can be directly backcalculated through FWD deflections tested in-service asphalt pavement, which can bypass the conventional backcalculation of elastic modulus and the shift of dynamic modulus curve.

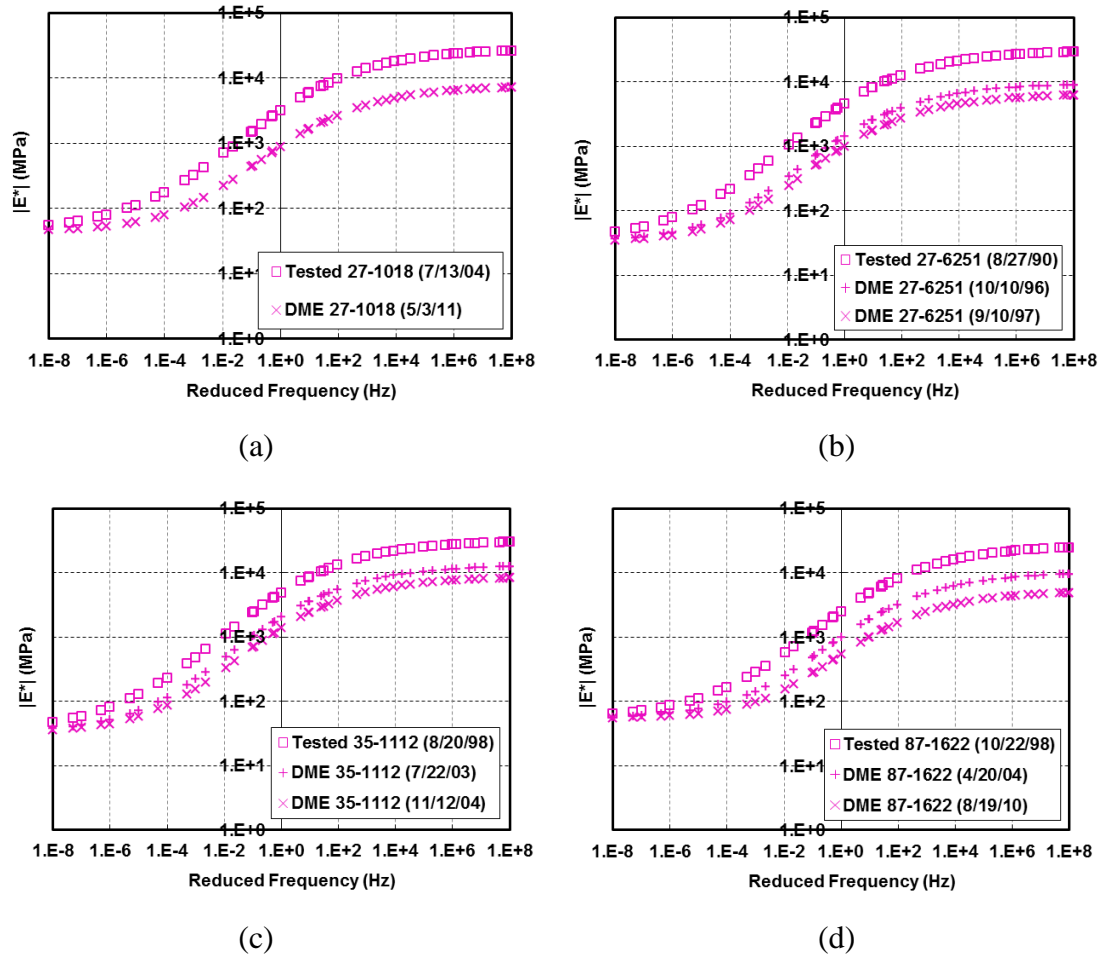


Figure 4.13 Dynamic moduli in different phases of AC deterioration by MEPDG approach for LTPP section (a) 27-1018; (b) 27-6251; (c) 35-1112; and (d) 87-1622

#### 4.5.6 Comparison with LTPP Field Distress Data

It is expected that pavement distresses increase as pavement material deterioration happens. Field distress survey data were extracted from LTPP database as indication of pavement performance deterioration. Although multiple distress data are available in LTPP database, the analysis here focused on fatigue cracking considering it is the structural distress related mostly to material modulus.

Figure 4.14 plots pavement fatigue cracking against damage factors in the AC layer recorded in LTPP program based on different time points within one construction period.

The summation fatigue cracking area at low, medium and high severity levels were presented here. It is noted that the records of fatigue cracking in section 35-1112 were not available and the ones in section 27-1018 and 27-6251 were only measured at several timings. The results show that fatigue cracking area increase as the damage factor is higher. Therefore, the deterioration trend of AC modulus is related to the increase of figure cracking area at pavement surface. The increase of fatigue cracking and damage factor with time are not exactly following the same points, which indicates that the correlation between fatigue cracking and damage is not linear relationship.

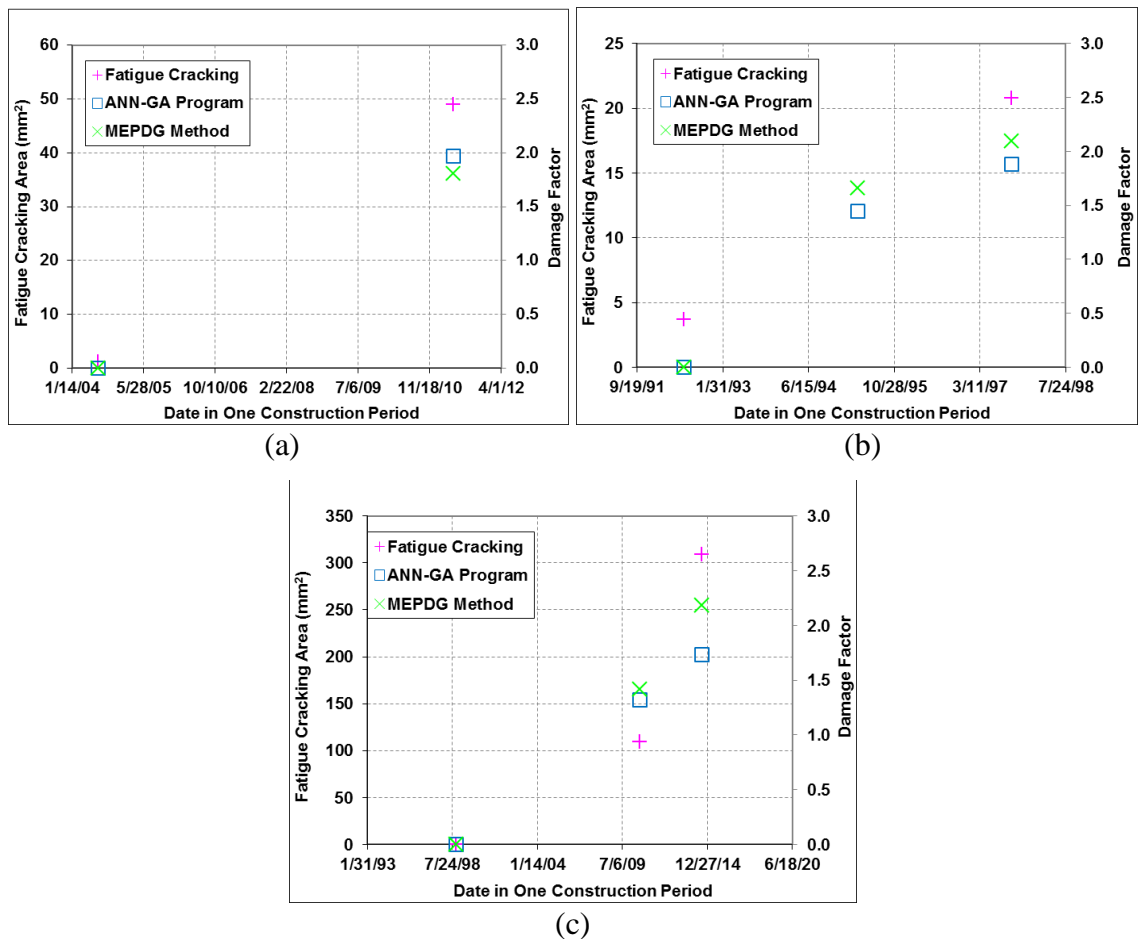


Figure 4.14 Correlation between pavement distresses and damage levels in AC for (a) 27-1018; (b) 27-6251; and (c) 87-1622

## **4.6 Assessment of Unbound Material Degradation**

### *4.6.1 Unbound Material Properties at Field Sections*

As discussed in previous section, measured FWD deflections and laboratory-tested layer material parameters were considered in the validation of ANN-GA Program. Previously five pavement sections were selected from the LTPP database. Although unbound material parameters were not rather available for those selected pavement sections, ANN-GA program can be used to investigate the unbound material properties. Unbound material moduli were measured as resilient ones along with corresponding bulk and deviator stress. And the measurements were incorporated into Equation 3-7 to produce the regression results ( $k_1$ ,  $k_2$ , and  $k_3$ ) for base layer and subgrade (Park et al. 2005).

Nine pavement sections from the LTPP program were further used to validate the ANN-GA program with field data from AC to unbound material parameters, which were from the Seasonal Monitoring Program (SMP) of LTPP database. The primary information with material types for those pavement sections was summarized in Table 4.3 and Table 4.4 (Yau and Von Quintus 2002; Park et al. 2005). The section information data listed would be incorporated into the ANN-GA program to backcalculate the material properties in validation with the listed unbound material parameters.



Table 4.3 LTPP On-site Testing Pavement Section Information

Section Information						Material Type		
State No.	State	ID	AC	Base	Subbase	Base	Subbase	Subgrade
27	MN	1018	112	132	/	Gravel	/	SP
27	MN	6251	188	259	/	Gravel	/	SP
28	MS	1016	195	525	/	Granular	/	SM
28	MS	1802	220	51	/	Silty Sand	/	SC
35	NM	1112	160	152	/	Soil Agg.	/	SP
48	TX	1068	277	152	203	Cr. Stone	Lime-tr Soil	CL
48	TX	1077	130	264	/	Cr. Stone	/	ML
48	TX	1122	81	396	213	Soil Agg.	F. gr. Soil	SP
87	ON	1622	135	168	668	Cr. Gravel	Sand	MH

Note: SHRP ID = Strategic Highway Research Program identification number; Cr. Stone = crushed stone; Cr. Gravel = crushed gravel; Agg = aggregate; Soil Agg. = soil aggregate; Lime-tr soil = lime-treated soil, ML = inorganic silts and very fine sands; SM = sand-silt mixtures; MH = micaceous fine sandy soils; SP = poorly graded sands; SC = sand-clay mixtures; CL = inorganic, gravelly, or sandy clays.

Table 4.4 Unbound Material Parameters for LTPP Sections

Unbound Material Parameters				
State No.	State	ID	Base Layer ( $k_1/k_2/k_3$ )	Subgrade ( $k_1/k_2/k_3$ )
27	MN	1018	0.752/0.632/-0.264	0.715/0.692/-0.737
27	MN	6251	N/A	0.614/0.887/-1.764
28	MS	1016	0.720/0.617/-0.143	0.564/0.834/-1.419
28	MS	1802	0.900/0.639/-0.121	0.753/0.304/-0.060
35	NM	1112	0.948/0.804/-0.538	0.846/0.513/-0.122
48	TX	1077	1.153/0.634/-0.066	0.762/0.440/-1.017
48	TX	1122	1.564/0.482/-0.004	0.778/0.648/-0.211
87	ON	1622	0.744/0.667/-0.323	0.834/0.374/-0.978

The ANN-GA program was used in particular to predict layer parameters of existing asphalt pavement, rather than just the undamaged one, by inputting into the program pavement variables including peak deflections at different offsets, shape factors of hysteresis loop, layer thicknesses, loading magnitudes, and air and surface temperatures. Similar process was applied as show in Figure 4.9.

#### *4.6.2 Validation of ANN-GA Program for Unbound Material Properties*

A validation on the pavement sections was conducted in this paper for backcalculating unbound material properties through the ANN-GA program, as shown in Figure 4.15 and 4.16. Figure 4.15 shows comparisons between LTPP testing and ANN-GA backcalculated base aggregate parameters for  $k_1$ ,  $k_2$ , and  $k_3$ . Good agreements were achieved from the backcalculation of the ANN-GA program between measurement and calculation whereas the section of 27-6251 was unavailable for the base aggregate parameters. Similar results can also be found in Figure 4.16 for the compared subgrade soil parameters between measurement and calculation.

The predicted nonlinear parameters were well matched with the tested parameters within 5% differences. Therefore, the validation signified the availability of estimating unbound material parameters from the ANN-GA program by FWD deflections, pavement structure, loading levels, and temperature profiles. The ANN-GA was proposed after the validation to verify the capacity of predicting degradation of unbound material by means of LTPP field testing results.

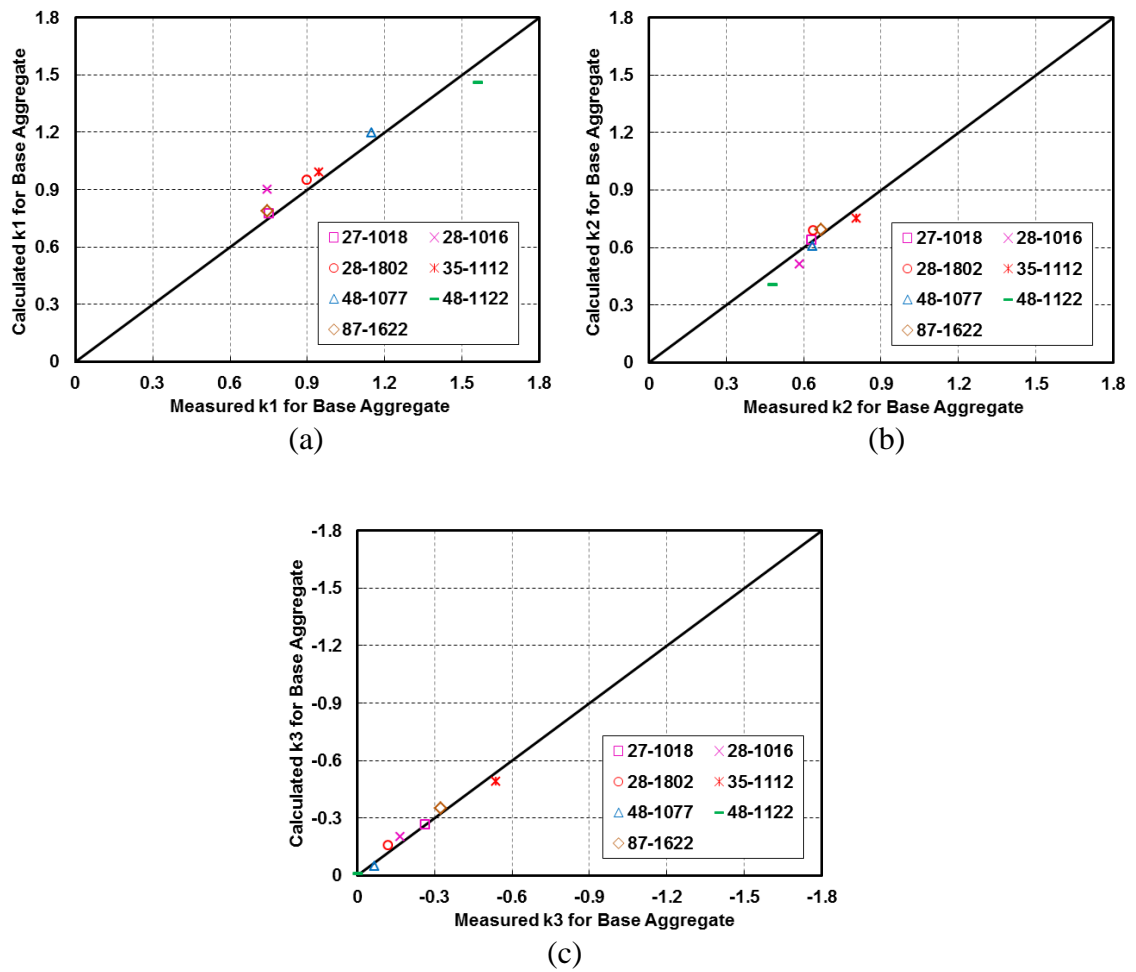


Figure 4.15 Comparison between LTPP testing and ANN-GA backcalculated base aggregate parameters: (a)  $k_1$ ; (b)  $k_2$ ; and (c)  $k_3$

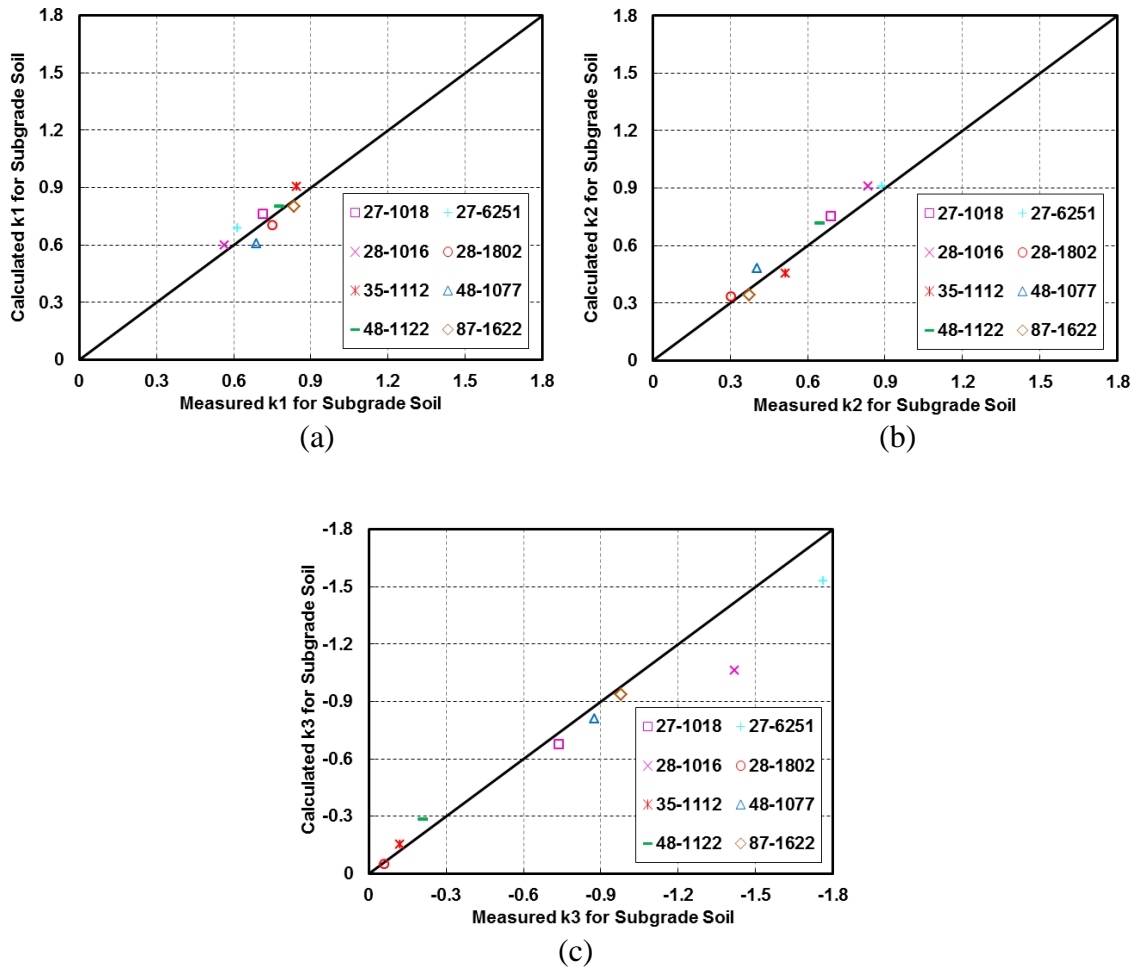


Figure 4.16 Comparison between LTPP testing and ANN-GA backcalculated subgrade soil parameters: (a)  $k_1$ ; (b)  $k_2$ ; and (c)  $k_3$

#### 4.6.3 Damage in Unbound Material Properties Modulus

The prediction of unbound material degradation was assumed dependent on measured FWD deflections at different pavement ages, because FWD deflections varied as base layer material deteriorated along time. In this study, only the material properties were assumed changed throughout the specified span of time. Table 4.4 and 4.5 show the backcalculated unbound material parameters using ANN-GA program for different stages of pavement service life. Only four sections were selected due to data availability in the field sections. During the calculation for the four sections, the parameter  $k_1$  showed

decreasing trend along pavement age in both base layer and subgrade. This indicates that the elastic modulus of unbound material decreases as the material degrades over time.

However, the changing trends of nonlinear parameters  $k_2$  and  $k_3$  are more complicated. The decreasing trends of  $k_2$  and  $k_3$  were observed in Table 4.5, which indicates the reduction of stress-hardening behavior in the aggregate layer. On the other hand, the increasing trends of  $k_2$  and  $k_3$  were observed in Table 4.6. It indicates of the reduction of stress-softening behavior for subgrade soil. It is known that nonlinear parameters of unbound material are affected by multiple factors, such as aggregate gradation and shapes, moisture content, density, and percent of fines. Although the degradation trend of unbound material is predicted from surface deflections, field testing is still needed to validate the cause of material degradation.

Table 4.5 Degraded Base Material Parameters Backcalculated by ANN-GA Program

Pavement section and date		$k_1$	$k_2$	$k_3$
27-1018	7/13/2004	0.752	0.632	-0.264
	5/3/2011	0.613	0.601	-0.291
27-6251	8/27/1990	N/A	N/A	N/A
	10/10/1996	0.725	0.671	-0.031
	9/10/1997	0.692	0.657	-0.049
35-1112	8/20/1998	0.948	0.804	-0.538
	7/22/2003	0.827	0.753	-0.591
	11/12/2004	0.715	0.726	-0.612
87-1622	10/22/1998	0.744	0.667	-0.323
	4/20/2004	0.665	0.651	-0.319
	8/19/2010	0.589	0.648	-0.311

Table 4.6 Degraded Subgrade Material Parameters Backcalculated by ANN-GA Program

Pavement section and date		k <sub>1</sub>	k <sub>2</sub>	k <sub>3</sub>
27-1018	7/13/2004	0.715	0.692	-0.737
	5/3/2011	0.597	0.721	-0.698
27-6251	8/27/1990	0.614	0.887	-1.764
	10/10/1996	0.578	0.843	-1.792
	9/10/1997	0.552	0.817	-1.819
35-1112	8/20/1998	0.846	0.513	-0.122
	7/22/2003	0.805	0.539	-0.107
	11/12/2004	0.763	0.561	-0.096
87-1622	10/22/1998	0.834	0.374	-0.978
	4/20/2004	0.795	0.399	-0.939
	8/19/2010	0.769	0.412	-0.891

## 4.7 Summary

In this chapter, axisymmetric finite element (FE) models were developed to serve as the forward program simulating FWD-induced pavement responses and generating an assembled synthetic database. The FE models considered dynamic loading nature of FWD testing and viscoelastic and nonlinear material parameters for pavement layers. And the FE models were validated by field testing data before incorporated into the development of the ANN-GA program.

The ANN-GA possesses some advantages over traditional iteration-based backcalculating program such as the elimination of seed moduli and consideration of complex material properties. More importantly, the backcalculated pavement layer parameters can be directly used for M-E design of pavement overlays.

The ANN-GA program provides an effective approach in assessing structural capacity of existing pavement. The deterioration condition of AC modulus was found consistent with fatigue cracking measured at pavement surface based on LTPP distress survey results. And the degradation of unbound material was validated by LTPP database. Although quantified relationship between the damaged modulus parameters and pavement distress need to be further studied, the developed ANN-GA program can be

successfully used to obtain dynamic moduli of damaged AC and evaluate *in situ* pavement condition from structural point of view. The backcalculated moduli of existing pavement layers can be further used to facilitate the overlay design procedure using MEPDG.

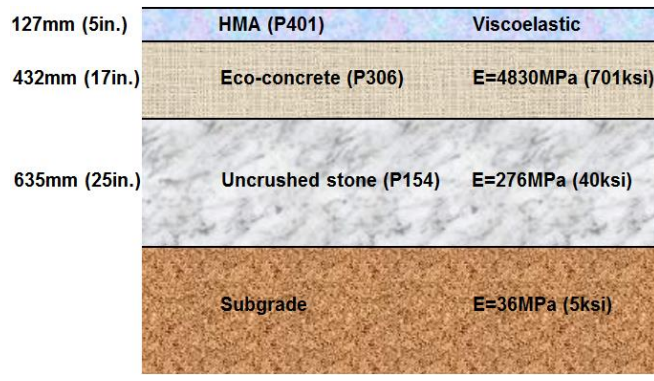
## **CHAPTER 5 AIRPORT PAVEMENT RESPONSES UNDER HIGH TIRE PRESSURE AND AIRCRAFT GROUND MANOVERTING**

### **5.1 Accelerated Pavement Testing at NAPTF**

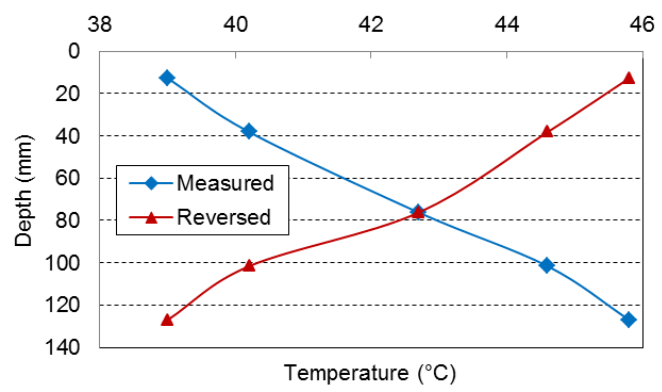
#### *5.1.1 Indoor Heated Pavement Sections*

The modeled pavement structure in this analysis is an existing section built at the NAPTF for high tire pressure tests as shown in Figure 5.1 (a). The pavement section consists of a HMA surface layer (P-401), an econocrete base layer (P-306), an uncrushed aggregate subbase layer (P-154), and the subgrade. P-401, P-306, and P-154 are FAA specifications for airport pavement materials referenced in FAA AC 5320-10F (FAA 2013). In the test section, a hydronic (hot water piping) heating system was embedded along one-half of the depth of the econocrete layer to heat the pavement. Figure 5.1 (b) plots the measured temperature profile in the asphalt layer as well as the reversed temperature profile. The measured temperature profile was obtained from the artificial “bottom-up” heating that was used in the full-scale test; while the reversed temperature profile represents the natural “top-down” heating under sunlight. Figure 5.1 (c) shows the measured dynamic modulus curve that can be converted into an array of input parameters for FE program in terms of Prony series. The Prony series and shift factors are shown in Table 5.1.

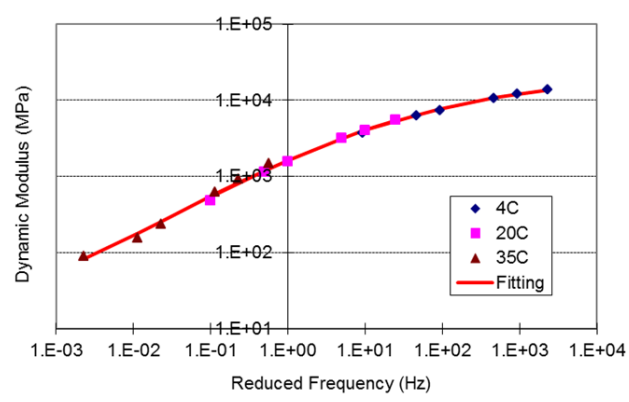




(a)



(b)



(c)

Figure 5.1 Modeled pavement: (a) cross-section; (b) two temperature profiles in FE modeling and (c) dynamic modulus curve

Table 5.1 Prony Series and Shift factors for the HMA material

i	$G_i$ or $K_i$	$\tau_i$	WLF	
1	3.56E-01	5.00E-04	C <sub>1</sub>	33.5
2	3.04E-01	7.70E-03		
3	1.89E-01	9.44E-02		
4	7.28E-02	6.03E-01	C <sub>2</sub>	291.5
5	4.97E-02	4.36E+00		
6	1.84E-02	1.54E+01		

As shown in Figure 5.2, the distribution of vertical contact stress with tire inflation pressure of 1.45MPa presents a concentrated stress as high as 3.6MPa at the edge rib of the tire at play. The aspect ratio of the tire imprint (the ratio of contact width to length) was controlled depending on the load level. Previous field measurements of tire-pavement contact behavior have shown that, as the tire load increases, the contact length increases more significantly than the contact width due to the rigidity of tire sidewall (Howll et al. 1986). The aspect ratio was selected as 0.71 when the tire loading is 133kN and 0.63 when the tire loading is 222kN, respectively.

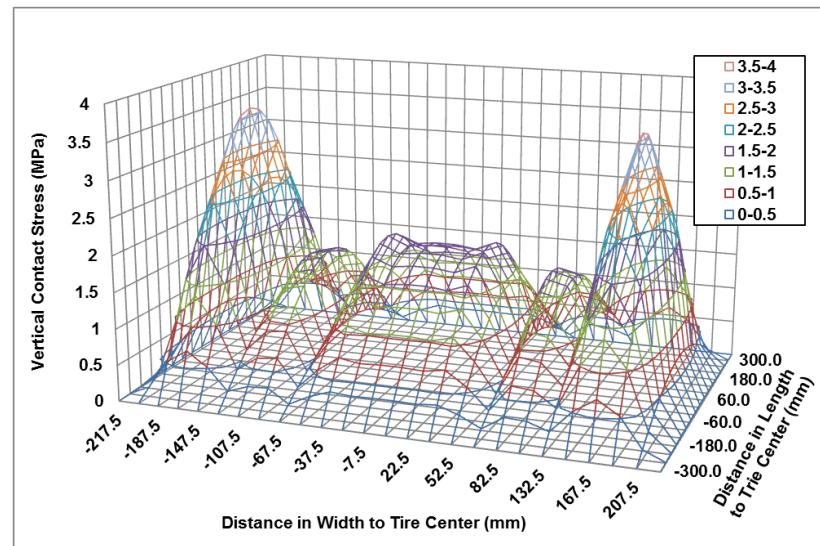


Figure 5.2 Distributions of tire-pavement vertical contact stresses

Figure 5.3 shows measurements from the full-scale test at the indoor heated pavement section by applying two wandering paths parallel to the main wheel path in different passes (Song 2010). The increasing tire load causes much greater rutting depths while the higher tire inflation pressure causes slight increase in rutting depths slightly.

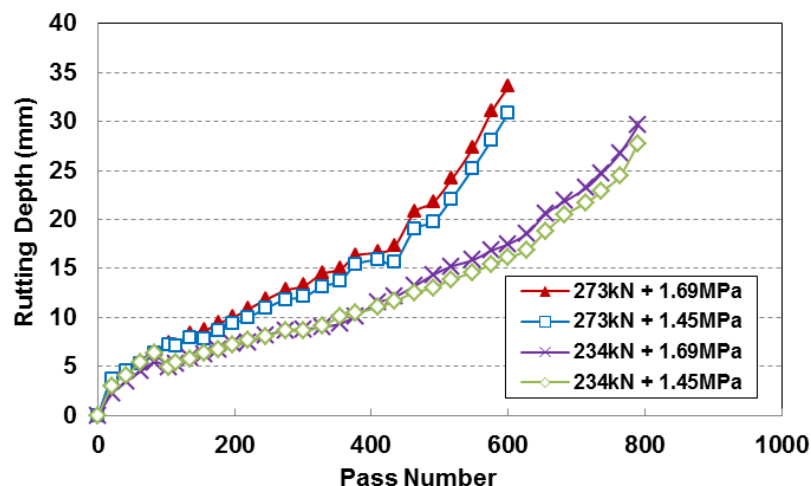


Figure 5.3 Rutting depth measured at the indoor heated pavement section

### 5.1.2 HVS Test Sections

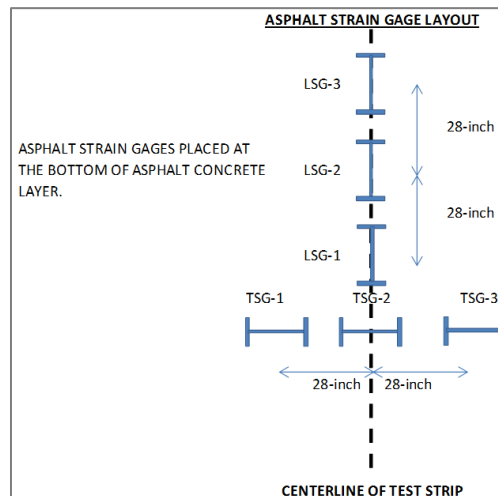
The FAA Airport Technology R&D Branch accepted the Heavy Vehicle Simulator-Airport Version (HVS-A) in November 2013, as shown in 5.4 (a). The HVS-A was designed to apply single- and dual-wheel system that can load up to 100 kips in a wandering range of 6 feet. The pavement surface temperature in the chamber can be heated up to 150°F and the test speed for the simulated wheel loading ranges from 0.17 to 5 mph. It was designed to accommodate the 52x21.0R22 radial tire for single-wheel and smaller tires (such as B737-800) would be assigned for dual-wheel assembly.

In the acceptance test of HVS-A, two pavement sections were built to evaluate the effect of aircraft high tire pressure on responses of airfield flexible pavement. The

pavement structure is composed of a 254-mm asphalt layer (P401) with the PG76-22 binder and a 381-mm aggregate base layer (P209). The pavement section was constructed on sandy subgrade with a California Bearing Ratio (CBR) of 20. During construction, strain gauges were embedded at the bottom of the asphalt layer and temperature gages were placed in the asphalt layer at different depths as shown in 5.4 (b).



(a)



(b)

Figure 5.4 NAPTF (a) Heavy Vehicle Simulator-Airport Version (HVS-A) and (b) pavement instrumentation

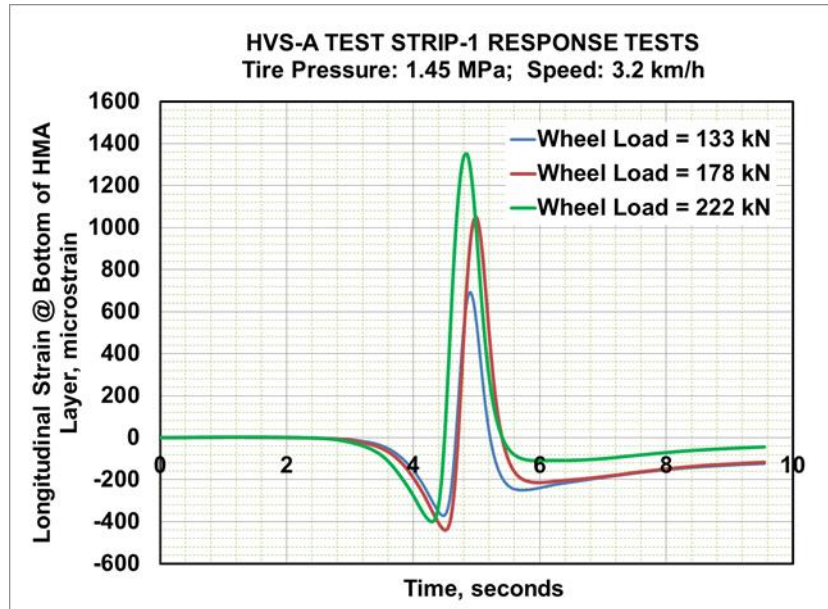
The accelerated pavement testing was implemented based on two plans, response testing and traffic testing (Garg et al. 2015). The tire pressure was set to 210 psi for tests on test strip-1 and 254 psi for tests on test strip-2. The response test plan aimed to identify surface profile of test strip in use of on-board profiler and to measure the tensile strains at bottom of HMA layer. The pavement surface temperature is 140°F measured at a depth of 1 inch below pavement surface. The test speed was 2 mph. Three levels of wheel loading were applied including 30,000, 40,000, and 50,000 lbs. The lateral wandering pattern included five wandering positions with the maximum offset of 20 inches away from centerline. Data from sensors embedded in pavement were collected for every loading cycle. To avoid the disturbance of the measurement for test strip-2, the testing on test strip-2 was performed after the traffic testing on test strip-1 was accomplished.

Test parameters for traffic testing were mostly the same as the ones implemented in response testing except the wheel load increased to 61,300 lbs. Pavement surface profile measurements were made using HVS-A on-board profiler before the start of traffic tests. After that, surface profiles were measured after 18, 72, 144, 576, 1152, 2304, 4608, 9216 passes. Straight-edge rutting depth measurements were measured at three locations (middle three blue lines on the test strips) at the same intervals. The loading was applied in a predetermined wandering pattern that simulates a normally distributed traffic with approximate standard deviation of 12-inches and mean of zero. Each wander pattern consists of 5 offsets and 18 passes.

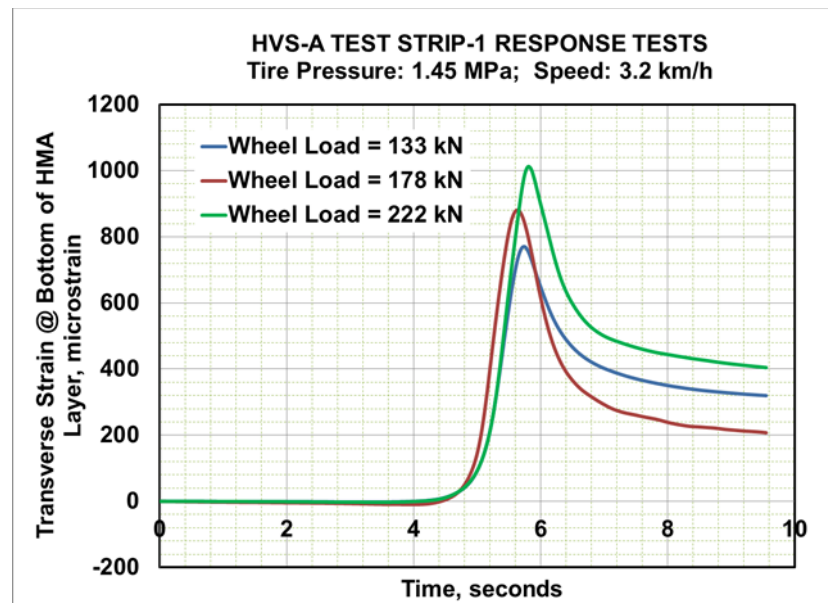
Figure 5.5 shows the measured tensile strains from the response test at different loading levels, respectively, for longitudinal and transverse tensile strains. The time histories of tensile strains under the moving tire loading were plotted. All of the strain gauges were embedded at the bottom of asphalt layer. Both the LSG-1 and LSG-2 gauges were embedded longitudinally at the centerline of the test strip. The TSG-1 gauge was embedded transversely at the centerline of test strip, while the TSG-2 strain gauge was embedded transversely at an offset of 28 inches away from the centerline. Only the measured tensile strains under tire loading with the inflation pressure of 210 psi were

reported here since the strain gauges in the test strip-2 for testing at tire pressure of 245 psi were found not functional.

The longitudinal strains appear the negative values (compression) as the tire is far away, then the positive values (tension) as the tire approaches the strain gage, followed by the negative values (compression) again as the tire is leaving. On the other hand, the transverse strains are always in tension or compression as the tire loading is approaching and leaving, depending on the transverse offsets of strain gauges to the loading location. This is because the direction of transverse strains was always perpendicular to the tire moving direction. An unsymmetrical pattern of strain shapes were observed for both longitudinal and tensile strains due to the viscoelasticity of asphalt mixture. The results clearly show that increasing loads produced the greater peak values for the tensile strains. It is noted that the peak values of longitudinal tensile strains were observed at different timings due to the offset locations of the embedded strain gages.



(a)



(b)

Figure 5.5 Measured (a) longitudinal and (b) transverse strains under different loading levels

Figure 5.6 shows the rutting depth measurement against loading passes under tire loading with two different tire pressure levels. It shows that the rutting depth increases nonlinearly as the loading pass increases. The difference of rutting depth under two pressure levels was smaller than 0.13 inches when the rutting depth is smaller than 0.75 inches; while the difference increased to 0.3 inches when the rutting depth reached 1.5 inches due to cracking outside traffic area. This indicated that the effect of high tire pressure on rutting became more noticeable when the rutting development progressed.

It is believed that the total rutting depth measured at the pavement surface is caused by the accumulation of permanent deformation in the asphalt layer, base layer, and subgrade. Previous studies conducted at the NAPTF have found that the rutting development in the thick base layer is significant due the shear stress caused by the moving load (Kim and Tutumluer 2004).

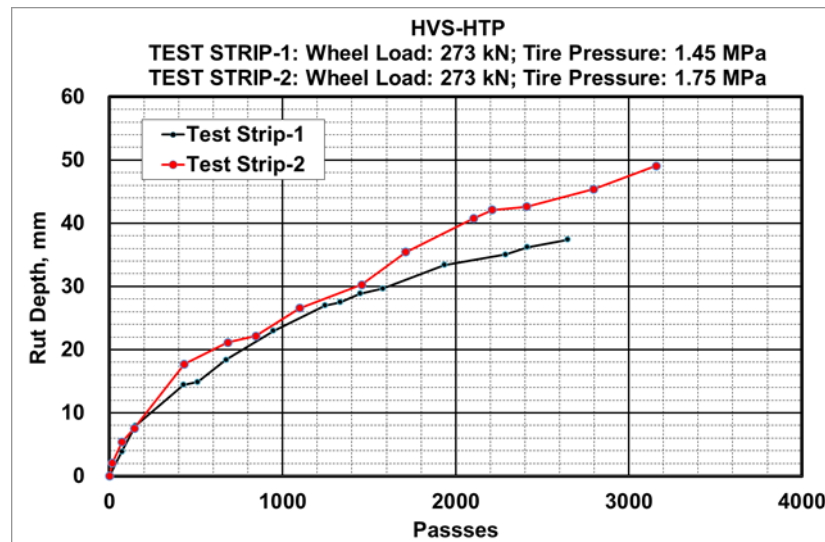


Figure 5.6 Rutting depth measured under two different pressure levels



## 5.2 Aircraft Tire Contact Stresses

### 5.2.1 Tire Contact Stress at Free Rolling Condition

The applied tire loads in the full-scale test were 273kN and 234kN, which are approximately equivalent to the wheel load of A380 with the gross weight of 586 tons and 502 tons. Two inflation pressure levels, 1.45MPa and 1.69MPa, were used to evaluate the influence of tire inflation pressure on pavement responses. This tire pressure of 1.69MPa exceeds the current ICAO tire pressure limit in category X (1.5MPa).

The realistic tire-pavement contact stresses are critical in the evaluation of tire pressure effect on pavement responses. For each tire inflation pressure, non-uniform contact stress distributions were assumed in the tire imprint area with five ribs, as shown in Figure 5.7 (a). The non-uniform contact stress distributions were based on the contact stress measurements under heavy aircraft tire load reported by Rolland (2009). In the longitudinal direction, a half-sinusoidal pressure distribution was used along the contact length of each rib. The peak contact stresses beneath two edge ribs were assumed equal to 2.5 times the tire inflation pressure; while the peak contact stresses under central ribs were assumed equal to 1.2 times the tire inflation pressure. As the inflation pressure increases, the contact length decreases; while the contact width was assumed constant due to the relatively high lateral stiffness of the tire sidewall.

Two uniform contact stress distributions (area-based and pressure-based) were used in the analysis to analyze the effect of contact stress pattern on pavement responses, Figures 5.7 (b) and 5.7 (c). The area-based distribution assumes that the contact area equaling the area in the non-uniform contact stress distribution and the contact stress equaling the wheel load divided by the area. The pressure-based distribution assumed that the tire contact stress equaling tire inflation pressure and the contact area equaling the wheel load divided by the contact stress. Table 5.2 summarizes the three contact stress distributions and contact areas under loading of 234kN at tire inflation pressure of 1.45MPa and 1.69MPa, respectively.

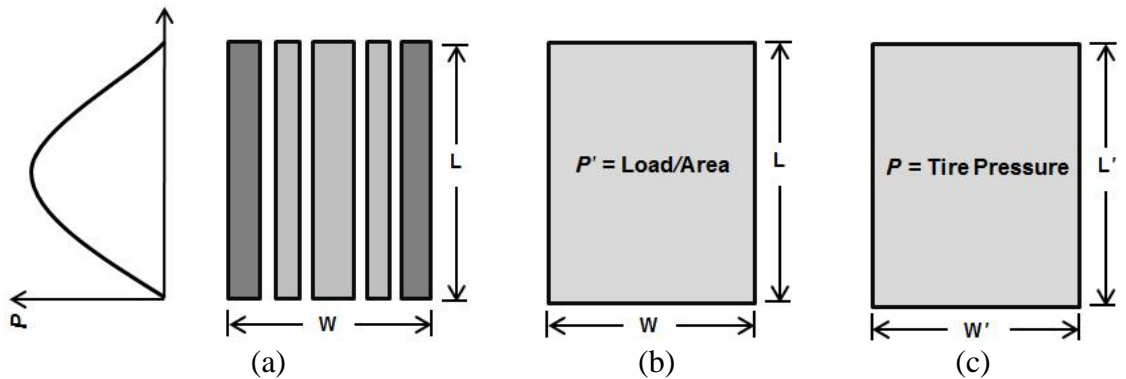


Figure 5.7 Contact stress assumptions of (a) non-uniform, (b) area-based uniform, and (c) pressure-based uniform

Table 5.2 Contact Stress Distributions and Contact Areas (Tire load: 234kN)

Contact stress Assumptions		Contact width (mm)	Contact length (mm)	Tire pressure at 1.45MPa	Tire pressure at 1.69MPa
				Peak contact stress (MPa)	
Area-based uniform		400	520	1.12	1.33
Pressure-based uniform		360	440	1.45	1.69
Non-uniform	Rib 1	60	520/440	3.05	3.55
	Rib 2	50	520/440	1.52	1.86
	Rib 3	120	520/440	1.52	1.86
	Rib 4	50	520/440	1.52	1.86
	Rib 5	60	520/440	3.05	3.55
	Groove	15	520/440	0	0

### 5.2.2 Tire Contact Stresses at Maneuvering Conditions

The tire loading parameters follow the recommendation from the airplane manual of Boeing 737-600, which is one of most common aircrafts at large hub airports (Boeing 2013). Typical landing and takeoff weights were considered and the calculated loads on a single wheel are 153kN (34.4kips) for landing and 182kN (40.9kips) for takeoff,

respectively. The main gear tire pressure of B737-600 is 1.4MPa (203psi) with a tire-pavement contact area of 600mm×380mm (L×W).

Three tire rolling conditions at landing were considered to analyze the impact of aircraft ground maneuvering on airfield pavement responses. These include free rolling at taxiing, full-braking (FB-Loading), and turning at high-speed exit (THE-Loading). An instant full-braking operation after aircraft landing decelerates the velocity until it is appropriate for turning at the exit taxiway. The high-speed exit taxiway that forms a 30-degree angle with the runway centerline is used to reduce the runway occupancy time and enhance airport capacity (FAA 2012). The high-speed exit can guide the aircraft off the runway at speeds of up to 48km/h (30mph) with minimum brakes (Vickers 1991). In order to better investigate the effect of maneuvering operations on pavement responses, the operating speed of 37km/h (23mph) was used for different tire rolling conditions based on the average taxiing speeds reported in the literature (Jordan et al. 2010).

The tire loading for different operating conditions were characterized with the non-uniformly distributed contact stresses at the tire-pavement interface. The non-uniform vertical contact stress distributions were based on the contact stress measurements under heavy aircraft tire loading (Rolland 2009). In the longitudinal direction, a half-sinusoidal distribution of vertical contact stress was used along the contact length of each rib. The peak contact stresses beneath two edge ribs were assumed equal to around 2.2 times the tire inflation pressure; while the peak contact stresses under central ribs were assumed equal to around 1.1 times the tire inflation pressure. The vertical contact stresses were assumed similarly for all the free rolling, braking, and turning conditions.

The tangential tire contact stresses were assumed accordingly based on the rolling status of tire. At free-rolling, the distribution of tangential contact stresses follows the trend that was reported from previous instrumentation measurements and tire modeling (Howell et al. 1986; Wang et al. 2012). In the analysis, two contact stress patterns were considered for free rolling, one with vertical contact stresses only (V-Loading) and another one with 3-D contact stresses (3D-Loading). For full braking, the longitudinal contact stresses were assumed equal to the vertical contact stresses multiplied by the tire-

pavement friction coefficient (a coefficient of 0.8 was used for the highest possible friction on dry pavement surface). In this case, the slip ratio of tire was assumed 100% with pure sliding on pavement surface. To consider the tangential contact stresses caused by aircraft turning at the high-speed exit, the resultant shear due to the centripetal motion were considered, as shown in Equation 5-1 (Cook et al. 2015). The typical steering angle of 30° and a turning radius of 16m were used for Boeing 737-600 (Boeing 2013).

$$F = m \frac{v^2}{r} \quad (5-1)$$

where,

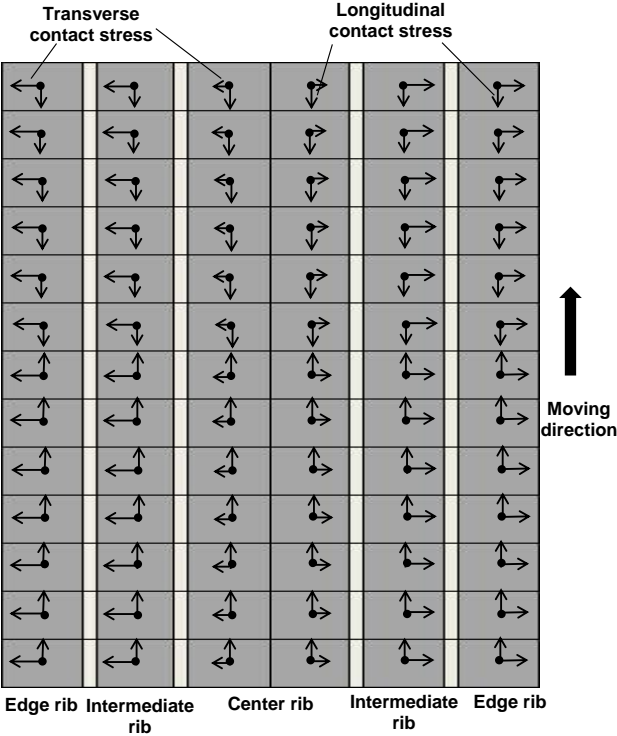
$F$  is the resultant turning force;

$m$  is the mass of single tire load;

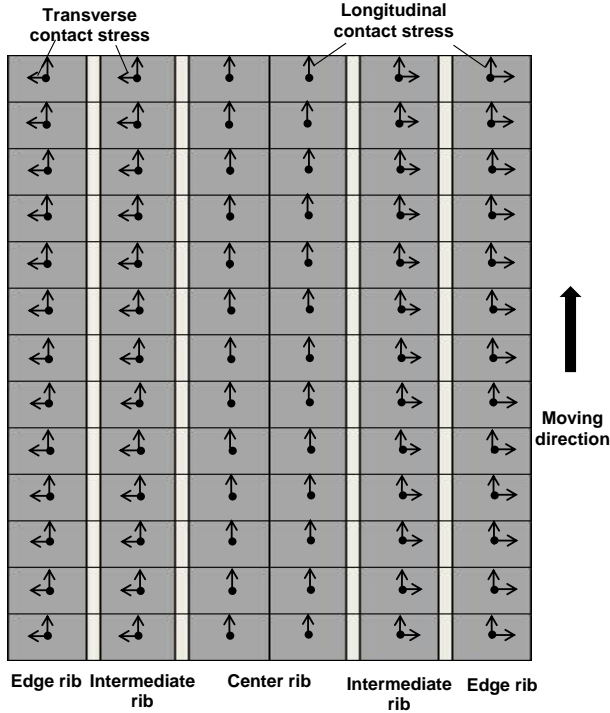
$v$  is the aircraft turning velocity at inner gear; and

$r$  is the turning radius.

Figure 5.8 shows the distribution of tire-pavement contact stresses for different ground maneuvering operations, where the center rib is wider and grooves exist between tire ribs.



(a)



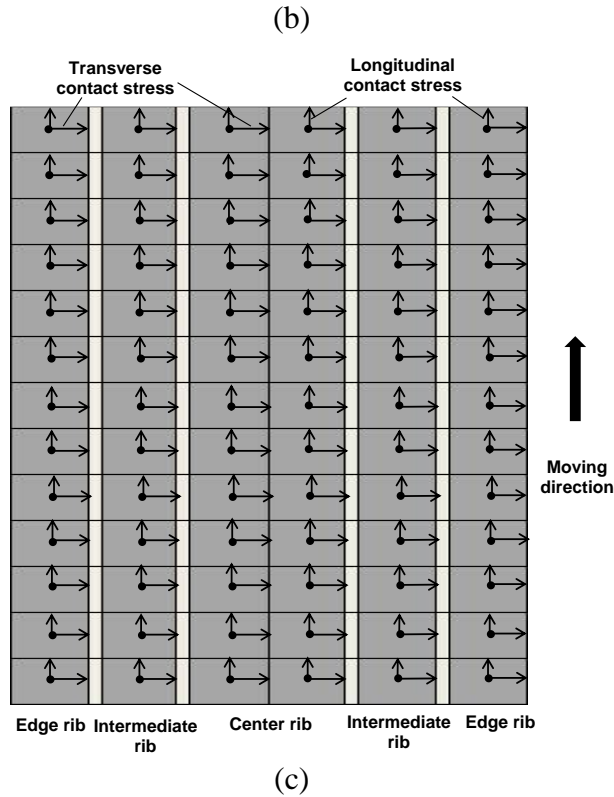


Figure 5.8 Illustration of tire-Pavement contact stresses for (a) free rolling; (b) full braking; and (c) turning

### 5.3 Development of FE Model for Airfield Pavement

#### 5.3.1 Material Properties

The viscoelastic material properties of asphalt mixture were considered in the finite element model. Figure 5.9 shows the measured dynamic modulus and the fitted master curve using the sigmoid function at a reference temperature of 20°C, as well as the related Prony series. As expected, under a constant loading frequency, the dynamic modulus decreases as the temperature increases; while under a constant testing temperature, the dynamic modulus increases as the frequency increases.

The relaxation modulus was interconverted from the dynamic modulus using Equations 3-1, 3-2, and 3-3 assuming that the linear viscoelasticity of HMA was represented by a generalized Maxwell solid model. The relaxation modulus and

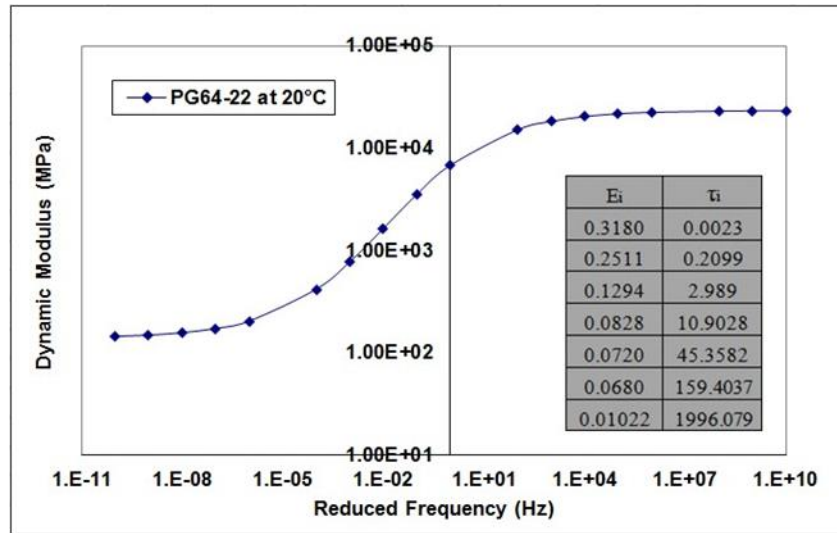
relaxation times were determined by minimizing the sum of squares of the errors (Equation 5-2). The bulk and shear relaxation moduli were calculated assuming a constant Poisson's ratio. The relationship between the shift factor and the temperature can be approximated by the Williams-Landell-Ferry (WLF) function (ABAQUS 2010).

$$\min \sum_{j=1}^k \left[ \left( \frac{E'(\omega)_{calculated}}{E'(\omega)_{measured}} - 1 \right)^2 + \left( \frac{E''(\omega)_{calculated}}{E''(\omega)_{measured}} - 1 \right)^2 \right] \quad (5-2)$$

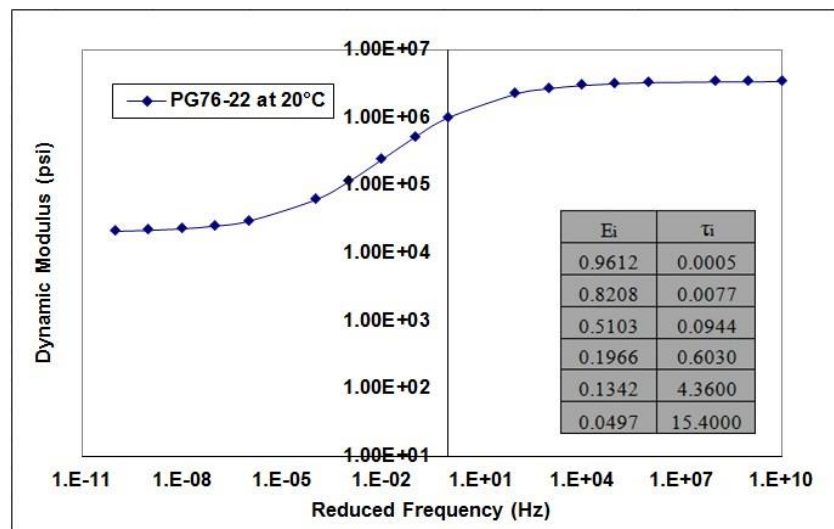
Where,

$E'(\omega)$  is real part of the dynamic modulus; and

$E''(\omega)$  is imaginary part of the dynamic modulus.



(a)



(b)

Figure 5.9 Master curve of dynamic modulus at 20°C for (a) PG 64-22 and (b) PG76-22 asphalt mixture

### 5.3.2 Material Parameters of Unbound Layers

To investigate the effect of aggregate base nonlinearity on pavement responses, both linear isotropic and cross-anisotropic nonlinear models were used to predict pavement



responses. For the linear isotropic analysis, the elastic modulus was set equal to a typical value of 330MPa for the P-209 base layer. In the nonlinear cross-anisotropic model, the vertical modulus is described using the generalized model adopted in the proposed Mechanistic-Empirical Pavement Design Guide (MEPDG), Equation 3-7 (ARA 2004). In this model, the first stress invariant or bulk stress term considers the hardening effect, while the octahedral shear stress term considers the softening effect. The nonlinear coefficients ( $k_1 = 2.800$ ,  $k_2 = 1.184$ , and  $k_3 = -1.597$ ) were obtained from the literature where the stress-dependent modulus of P-209 base material was measured at different moisture contents (Nazarian et al. 2014). The stress dependency of Poisson's ratios was not considered in this study and the in-plane and out-of-plane Poisson's ratios are assumed constant.

For the cross-anisotropic modulus, the horizontal and shear modulus ratios ( $n$  and  $m$ ) were used, as shown in Equations 3-10 and 3-11. Previous research has found that horizontal modulus ratios and shear modulus ratios had a relatively small range of variation (Tutumluer and Thompson 1997). The modulus ratios were assumed constant as 0.35 for  $n$  and  $m$  in this study as typical values. The linear elastic modulus of the subgrade in the thin asphalt pavement section was estimated from its California Bearing Ratio (CBR) value, as shown in Equation 5-3.

$$M_R = 2555(CBR)^{0.64} \quad (5-3)$$

### 5.3.3 FE Model Meshes and Boundary Conditions

A 3-D FE model was developed using ABAQUS Version 6.10-EF2. The schematic illustration of the FE mesh is shown in Figure 5-10. In the FE model, the element thicknesses were selected at 10-20 mm for the HMA layers and 30-50mm for the base/subbase layers and subgrade. The widths of the elements within the loading area were selected at 10-25 mm depending on the widths of tire ribs and grooves. The lengths of the elements were selected at 40 mm in the longitudinal (trafficking) direction. The elements in the loading area were loaded with the non-uniform contact stress

corresponding to their locations within the tire imprint area. For the non-uniform stress distribution, the loading magnitudes of contact stress continuously changed at each step as the tire was moving. The loading area at a specific level of load and inflation pressure was considered by adjusting the numbers and dimensions of elements within the tire imprint area.

Infinite elements were used in the transverse and longitudinal boundaries of the model and at the bottom of subgrade to reduce the degrees of freedom at far field and absorb stress waves for dynamic analysis. Sensitivity analysis was conducted to determine the location of infinite boundaries so that the strains in the asphalt layer show less than 5% changes as the domain sizes increase, Figure 5-11. The finite dimension of the model was selected to be 5.4m (length) $\times$ 3.4m (width) $\times$ 2.6m (depth) with an in-plane loading area of 2.8m $\times$ 0.7m to balance the computation cost and accuracy. The dynamic transient analysis was used in this study considering the inertia associated with the moving load and the dependency of the material properties on the loading frequency. Additional details about moving load simulation and dynamic transient analysis can be found elsewhere (Wang 2011).

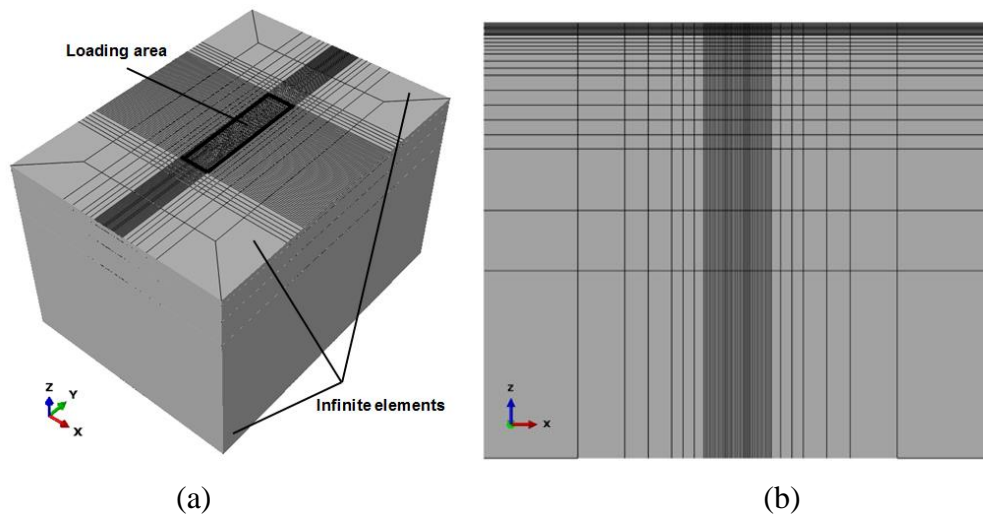
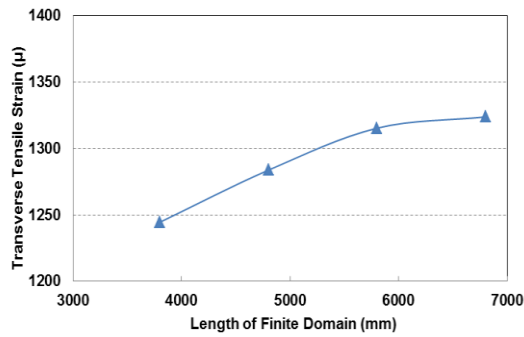
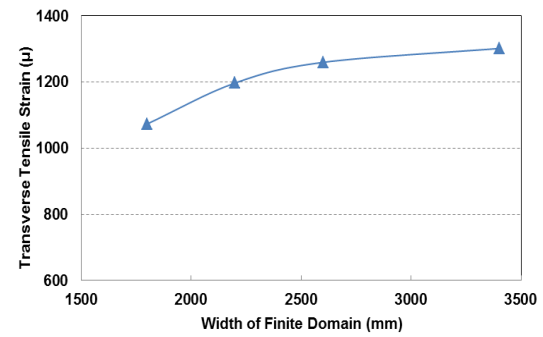


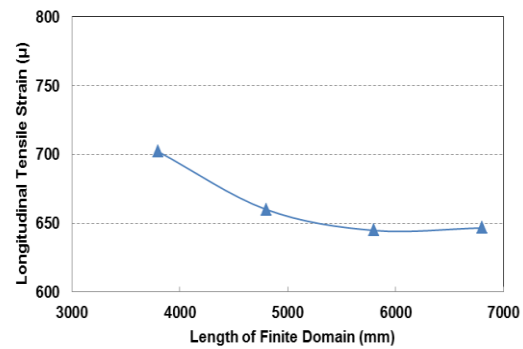
Figure 5.10 Schematic illustration of FE model layout: (a) 3-D finite with infinite domain and (b) cross-section of trafficking direction



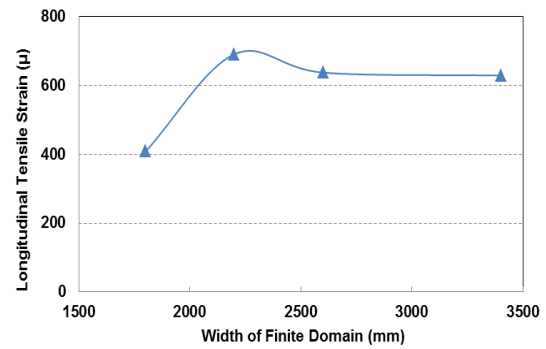
(a)



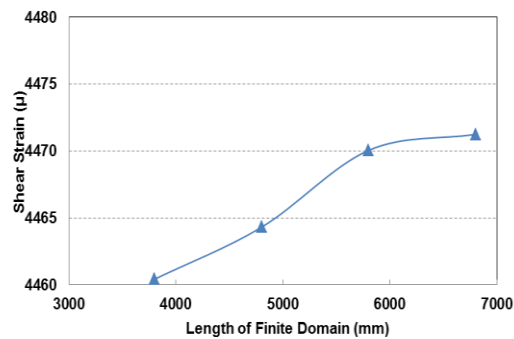
(b)



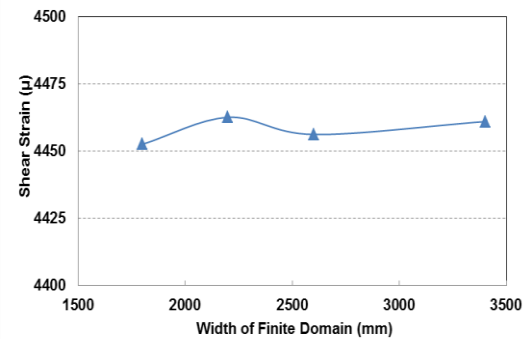
(c)



(d)



(e)



(f)

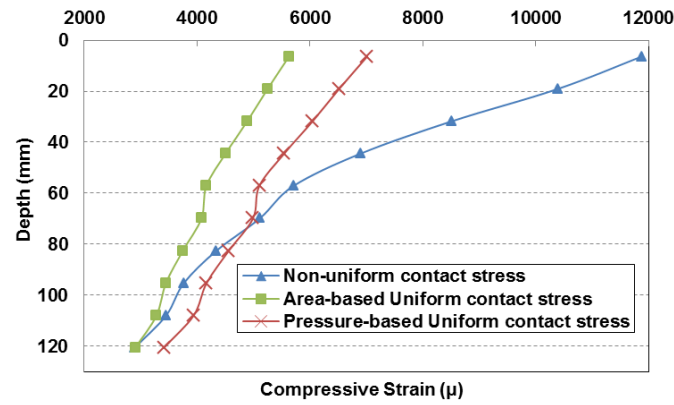
Figure 5.11 Sensitivity analyses for (a) transverse tensile strain vs. finite domain length; (b) transverse tensile strain vs. finite domain width; (c) longitudinal tensile strain vs. finite domain length; (d) longitudinal tensile strain vs. finite domain width; (e) shear strain vs. finite domain length and (f) shear strain vs. finite domain width

## **5.4 Analysis of Pavement Responses with Heated Pavement Sections**

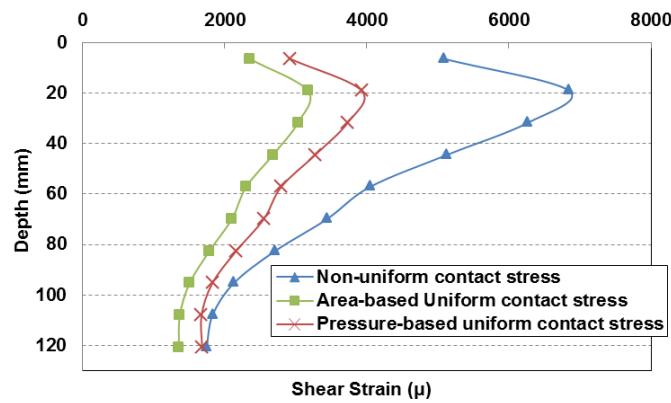
### *5.4.1 Effect of Tire-Pavement Contact Stresses*

The in-depth distributions of compressive, shear, and tensile strains under different contact stress assumptions were plotted in Figure 5.12. All pavement responses here were calculated using the reversed temperature profile at tire moving speed of 0.3m/s. Figures 5.12 (a) and 5.12 (b) show that the critical compressive strain is located at the surface of asphalt layer; while the critical shear strain is located at the shallow depth of asphalt layer. The upper-layer strain responses under the non-uniform contact stress are the greatest among three contact stress distributions. The area-based uniform contact stresses resulted in the minimum strains. The strain distribution patterns along the pavement depth are similar for both uniform contact stress patterns. However, the in-depth strain distribution under the non-uniform contact stresses features a curve with steeper slopes.

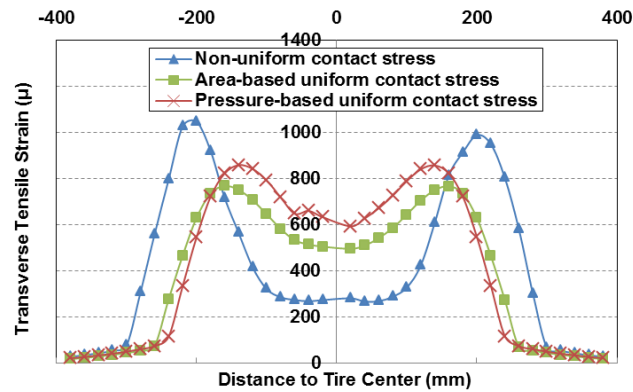
The transverse tensile strain was found as the critical tensile strain at the bottom of HMA layer and the strain distributions along the tire contact width were plotted in Figure 5.12 (c). It shows that the maximum transverse tensile strains are induced at different locations, depending on the contact stress assumptions. The location of critical tensile strain under non-uniform contact stresses stands at the very edge of tire imprint; however, the critical tensile strains under uniform contact stresses were located just inside the tire imprint. This is because the concentration of high contact stress at tire edge ribs when the non-uniform contact stress pattern is considered.



(a)



(b)



(c)

Figure 5.12 Effect of contact stress patterns on (a) in-depth distribution of compressive strain, (b) in-depth distribution of shear strain, and (c) transverse distribution of transverse tensile strain at the bottom of HMA layer

Table 5.3 compares the calculated maximum pavement responses using different contact stress distributions. Compared to two uniform contact stress distributions, the non-uniform stress distribution induces 18-27% greater critical tensile strain at the bottom of HMA layer. Therefore, using uniform stress distribution may underestimate fatigue cracking potential of airfield flexible pavement. However, tension-induced bottom-up cracking is not usually the primary distress in airfield pavements due to relatively thick asphalt layer, unless weak bonding between asphalt layers exists.

Moreover, the results clearly show that the non-uniform contact stress distribution induces 43-54% greater shear strains and 41-53% greater compressive strains, compared to the area-based and pressure-based uniform stress distributions. The changes are relatively significant. This is probably because the contact stress at the edge of the non-uniform pattern was up to 2.5 times the tire pressure. It necessitates the need of using stable asphalt mixtures with high shear resistance to support heavy aircrafts. Among three contact stress distributions, the minimal pavement responses were predicted if the area-based uniform contact stress pattern is used.

Table 5.3 Comparison of Critical Pavement Responses under Different Contact Stress Patterns (Tire load 234kN; Tire pressure 1.45MPa)

Contact stress pattern	Area-based uniform	Non-uniform	Change	Pressure-based uniform	Non-uniform	Change
Critical tensile strain ( $\mu$ )	767	1046	+27%	858	1046	+18%
Shear strain ( $\mu$ )	3170	6846	+54%	3927	6846	+43%
Compressive strain ( $\mu$ )	5632	11885	+53%	7017	11885	+41%

#### 5.4.2 Comparison between Moving and Stationary Loading

To evaluate the effect of loading conditions on airfield pavement responses, both moving and stationary loading were considered in the analysis. Two moving velocities were employed at 0.305m/s (0.68mph) and 2.2m/s (4.9mph), which were considered as reference velocities for analyzing AC strain responses at a previous full-scale test (Garg and Hayhoe 2001). In a like manner, the duration under the stationary loading was calculated based on two approaches. The first approach is the MEPDG method that calculates the effective length at any depth with an assumption of 45° affecting zone after transforming the pavement structure into a single layer using Odemark theory (ARA 2004). The second approach is using the vertical stress pulse from the FE model by detecting the slope change in the time history. Vertical stress was exclusively selected to calculate the pulse duration representing the equivalent loading time in the analysis. This is mainly because the compressive stress is not confounded with changes in moving directions and also not affected by the viscoelastic property in HMA layer like strains.

The pulse times calculated from different methods were compared at two velocities, as shown in Table 5.4 (a). As expected, the mid-depth pulse time under the 0.3m/s loading is much greater than the one at 2.2m/s. It shows that the pulse duration increases as the depth becomes deeper or the speed reduces. It is noted here that the calculated pulse duration using MEPDG method depends the selection of modulus for transforming the pavement structure into a single layer system and the assumption of 45° affecting zone is questionable (Al-Qadi et al. 2008).

Table 5.4 (b) compares the maximum pavement responses using moving and stationary loading. In the analysis, the mid-depth pulse duration under moving load was used as an equivalent loading time for the stationary loading. All pavement responses here were calculated under the non-uniform contact stress with the reversed temperature profile. The results indicate that as compared to the moving loading, the stationary loading method could predict the greater or smaller strain responses depending on the moving speed. As the stationary loading is applied, the small differences in the loading duration may cause considerable differences in the strain responses. In the moving load,

the loading time varies at different depths; while in the stationary loading the loading time is the same for the whole asphalt layer. This affects the viscoelastic modulus of asphalt material as well as the duration when the loading is applied.

All critical strain responses under speed of 2.2m/s were found 48-51% less than the responses under 0.3m/s. However, the difference between moving loading and stationary loading increases as the speed becomes greater. Therefore, the stationary loading may not be used as an alternative method to estimate the responses under moving loading.

Table 5.4 (a) In-depth Pulse Time from MEPDG and FE Methods

HMA depth	Moving speed = 0.3m/s		Moving speed = 2.2m/s	
	MEPDG method (s)	FE method (s)	MEPDG method (s)	FE method (s)
Surface	1.70	1.70	0.24	0.23
Mid-depth	2.46	2.23	0.34	0.31
Bottom	3.21	2.49	0.45	0.32



TABLE 5.4 (b) Comparison of Pavement Responses under Moving and Stationary Loading (Tire load 234kN; Tire pressure 1.45MPa)

Loading condition	Moving	Stationary	Change	Moving	Stationary	Change
	0.3m/s	2.46s (MEPDG)		0.3m/s	2.23s (FE)	
Critical tensile strain ( $\mu$ )	1046	1039	-0.7%	1046	964	-8%
Shear strain ( $\mu$ )	6846	7590	+11%	6846	6860	+0.2%
Compressive strain ( $\mu$ )	11885	12830	+8%	11885	11815	-1%
Loading condition	Moving	Stationary	Change	Moving	Stationary	Change
	2.2m/s	0.34s (MEPDG)		2.2m/s	0.31s (FE)	
Critical tensile strain ( $\mu$ )	542	595	+10%	542	570	+5%
Shear strain ( $\mu$ )	3386	3942	+16%	3386	3756	+11%
Compressive strain ( $\mu$ )	6243	7200	+15%	6243	6885	+10%

#### 5.4.3 Effect of Temperature Profile

Table 5.5 presents the calculated pavement responses under two different temperature profiles (Figure 5.1 (b)), as compared to the case that uses the average temperature for the whole asphalt layer. All pavement responses here were calculated at tire moving speed of 0.3m/s. Compared to the average temperature profile, the reversed temperature profile induces 8% less critical tensile strain at the bottom of HMA layer, but 12% greater maximum shear strains and 19% greater maximum compressive strains at near-surface locations, respectively. The opposite trends were caused by the temperature-dependent modulus of the HMA. The reversed temperature profile represents the field temperature condition in summer seasons. Therefore, it suggests that applying average temperature profile in summer is a conservative approach for predicting fatigue cracking

potential; however, it underestimates rutting or near-surface cracking potential in the airfield pavement.

On the other hand, the results from the measured temperature profile show 15% less maximum shear strains and 25% less maximum compressive strains as compared to the average temperature profile. However, the critical tensile strain was found nearly unchanged. In general, the results show that strain responses at the upper HMA layer seem more sensitive to the change of temperature profile.

Table 5.5 Comparisons of Pavement Responses with Different Temperature Profiles

Temperature profile	Average	Reversed	Change	Average	Measured	Change
Critical tensile strain ( $\mu$ )	1130	1046	-8%	1130	1118	0%
Shear strain ( $\mu$ )	6001	6846	+12%	6001	5075	-15%
Compressive strain ( $\mu$ )	9611	11885	+19%	9611	7162	-25%

#### 5.4.4 Effect of Tire Load and Inflation Pressure

Table 5.6 summarizes the maximum pavement responses beneath different tire loads and pressure levels. All pavement responses here were calculated under the non-uniform contact stress in the reversed temperature profile at tire moving speed of 0.3m/s. As the tire load increases from 234kN to 273kN, 17% greater tire load causes 12% greater maximum tensile strain at the bottom of HMA layer. On other hand, as the tire pressure increases from 1.45MPa to 1.69MPa, 17% higher tire pressure induces only 4% greater maximum tensile strain. It indicates that, in comparison with higher tire pressure, increasing tire load would reduce more service life of airfield pavements by inducing much greater fatigue cracking potential.

Similarly, the results show that 17% increase of tire load causes 19% greater maximum shear and compressive strains; while 17% increase of tire inflation pressure

causes 10-11% greater maximum shear and compressive strains. It signifies that the increasing tire load dominates the variation of shear and compressive strains over tire inflation pressure. Accordingly, an inference can be drawn that the tire load behaves as a predominant factor in impairing the resistance of airfield flexible pavement to near-surface rutting or cracking. Moreover, it is worthwhile to point out yet that near-surface cracking and rutting are two major failure modes in thick asphalt pavements; and thus the variations of shear and compressive strains are more significant than of tensile strains as tire load or pressure changes.

Table 5.6 Comparisons of Critical Pavement Responses under Different Tire Loads and Pressure Levels

Tire pressure: 1.45MPa				Tire load: 234kN			
Tire load	234	273	Change	Tire pressure	1.45	1.69	Change
Critical tensile strain ( $\mu$ )	1046	1174	+12%	Critical tensile strain ( $\mu$ )	1046	1090	+4%
Shear strain ( $\mu$ )	6846	8158	+19%	Shear strain ( $\mu$ )	6846	7543	+10%
Compressive strain ( $\mu$ )	11885	14119	+19%	Compressive strain ( $\mu$ )	11885	13142	+11%

## 5.5 Analysis of Pavement Responses at HVS Sections

### 5.5.1 Effect of High Tire Pressure

Table 5.7 summarizes the critical pavement responses caused by different tire pressure levels. Compressive strain of asphalt was located the critical spot on the top of surface close to the tire center. The maximum tensile strains were found at the bottom of asphalt layer under tire center. The maximum shear strain was found at the shallow depth of asphalt layer at the outmost tire rib. Unbound material layers have the maximum values on the top of layers under tire center. All critical pavement responses were calculated using the nonlinear cross-anisotropic model for base layer and linear elastic

modulus for subgrade. The results show that as the tire pressure increases from 210 psi to 254 psi, the changes of strain are smaller than 5% in general. This means that the effect of high tire pressure on fatigue cracking potential is not significant for the airfield pavement structure with a 10-inch asphalt layer.

On the other hand, the effect of tire load on strain responses was found much more significant compared to tire pressure effect. As the load increases, the increase of shear strain is more significant than the increase of tensile strain. This is probably because the tire load increase mainly causes the concentration of tire contact stress at tire edge ribs due to the rigidity of tire sidewalls. There is more obvious influence of increasing load than of higher tire pressure on both the compressive strain on the top of asphalt layer and compressive stress on the top of unbound material layers. It indicates that the rutting failure would be more sensitive to the loading magnitude other than the tire pressure.

Table 5.7 Comparison of Critical Pavement Responses under Different Tire Loads and Pressure

Parameters	Load = 30 kips using different tire pressure levels		Load = 50 kips using different tire pressure levels	
	210	254	210	254
Tire inflation pressure (psi)	210	254	210	254
Longitudinal tensile strain at bottom of asphalt layer (micro)	764	785	910	944
Transverse tensile strain at bottom of asphalt layer (micro)	996	1032	1081	1123
Shear strain in asphalt layer (micro)	2176	2204	3746	3926
Compressive strain on top of asphalt layer (micro)	1562	1572	2197	2333

### 5.5.2 Effect of Non-Linear Behavior of Granular Base

Figure 5.13 plots the distribution of vertical modulus in the base layer under the moving loading of 133- and 222-kN aircraft single wheel tire with tire pressure of 1.45MPa, using the nonlinear cross-anisotropic model for the base layer, asphalt binder

PG76-22 for the HMA layer, and an 155-MPa linear elastic modulus for the subgrade. The modulus plotted in Figure 5.13 is at the time step when the base modulus reaches the maximum value under the moving aircraft tire load. It is clearly shown that the modulus varies both vertically and horizontally because the stress state changes throughout the aggregate base layer. As expected, the highest modulus was observed on the top of the base layer under the loading center and the modulus decreases as the horizontal distance or vertical depth increases.

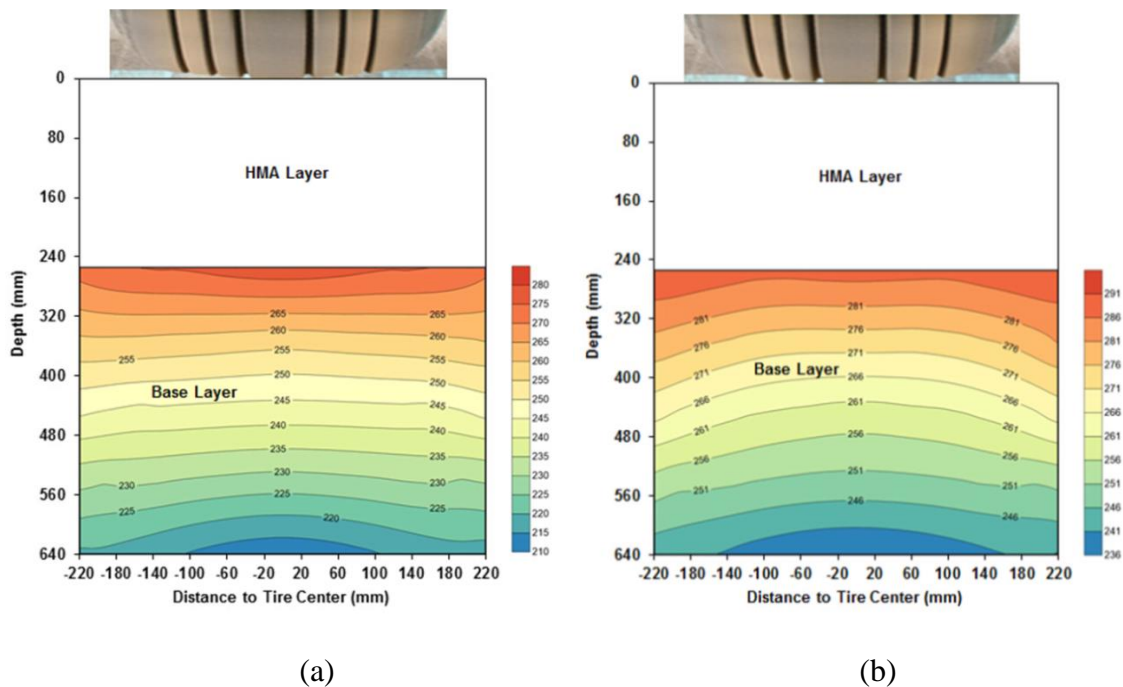


Figure 5.13 Vertical modulus distributions (unit: MPa) in base layer using nonlinear anisotropic model at (a) 133kN and (b) 222kN

Table 5.8 compares the strain responses calculated using different models for the granular base layer under two loading levels (30 kips and 50 kips) with tire pressure of 210 psi. The results show that the cross-anisotropic stress dependent model results in 27% to 58% greater tensile strains but only 2% to 4% greater shear strains, compared to the results obtained using the traditional linear isotropic model for granular base. It

indicates that the stress-dependency and cross-anisotropy of the aggregate base layer has more significant effect on the tensile strain than on the critical shear strain of asphalt layer. This may be attributed to the fact that the bending behavior of asphalt layer is more sensitive to the underlying layer support. 14 to 22% greater compressive strains on the HMA surface were found, while 14 to 19% smaller compressive stresses on the top of base layer were calculated. The opposite trend shows that traditional assumption for the base model underestimated the rutting potential generated by the HMA layer but overestimated the rutting failure in the base layer. And no significant difference of rutting-related compressive stresses was observed in the subgrade.

Table 5.8 Comparison of Pavement Responses Using Different Models for Aggregate Base Layer

Pavement responses	Load = 30 kips using different base models		Load = 50 kips using different based models	
	Linear isotropic	Nonlinear cross-anisotropic	Linear isotropic	Nonlinear cross-anisotropic
Compressive strain on the top of asphalt layer (micro)	1284	1562	1928	2197
Longitudinal tensile strain at the bottom of asphalt layer (micro)	599	764	718	910
Transverse tensile strain at the bottom of asphalt layer (micro)	661	996	690	1081
Shear strain in the asphalt layer (micro)	2083	2176	3666	3746

### 5.5.3 Comparison between Measured and Calculated Pavement Responses

Figure 5.14 plots the strain-time history predicted from the FE model, respectively, for longitudinal and transverse tensile strains. The strain development trend is consistent with the measured strain pulses. This emphasizes the importance of considering moving

load pattern and viscoelastic asphalt layer in the FE model for predicting pavement responses.

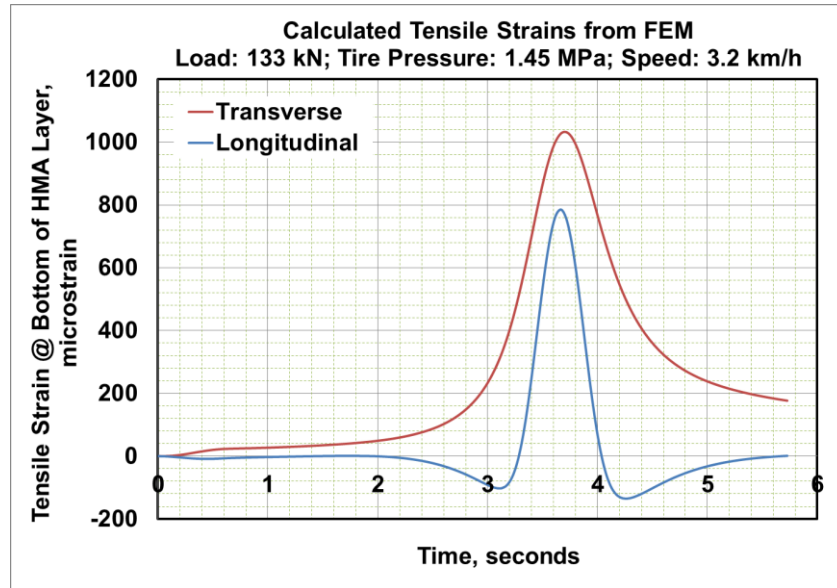


Figure 5.14 Caculated tensile strains from FE model

Figure 5.15 compares the calculated and measured tensile strains in the asphalt layer under two loading levels (30 kips and 50 kips) with tire pressure of 210 psi. In general, the modeling results agree well with measurement results when the nonlinear anisotropic mode was applied for the aggregate base material. Therefore it signifies the incorporation of the nonlinear model for unbound base layer into the prediction of responses in simulated flexible pavement. The discrepancy in Fig.9 (b) could be mainly caused by the reason that the stress-softening behavior of subgrade and the plastic behavior of asphalt concrete were not considered in the model, which will be considered in the future work.

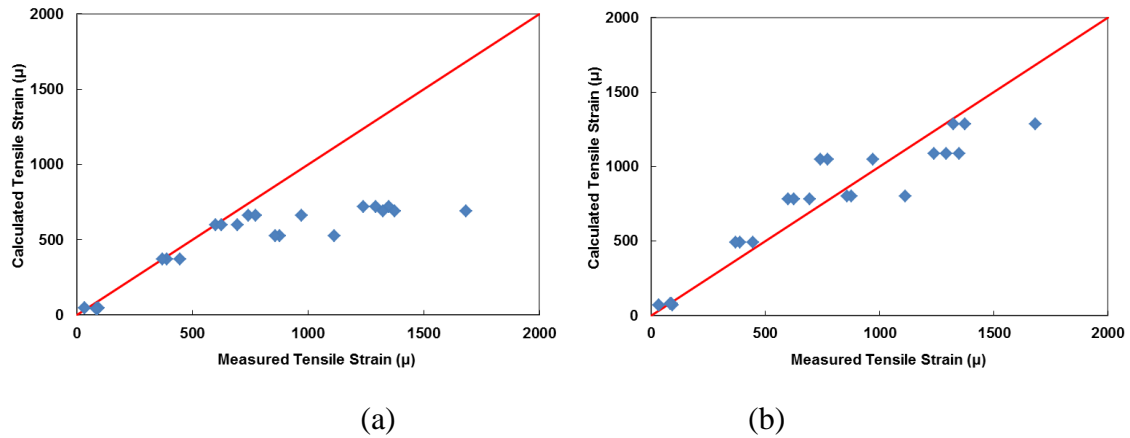


Figure 5.15 Comparison of tensile strains from Accelerated Pavement Testing and numerical modeling using (a) linear and (b) non-linear model for granular base

## 5.6 Effect of High Aircraft Tire Pressure on Rutting

### 5.6.1 Pavement Rutting Prediction Models

The rutting depths were calculated with contribution from each layer of flexible pavement, as shown in Equation 5-4. Considering the purpose of this study is to compare rutting depths under different loading conditions, available performance models in the literature were identified and the most appropriated ones were selected in the analysis.

$$RutDepth_{Total} = RutDepth_{AC} + RutDepth_{GB} + RutDepth_{SG} \quad (5-4)$$

The rutting depths in the HMA layer can be calculated using the performance transfer functions proposed by the calibrated AASHTO Mechanistic-Empirical Pavement Design Guide (MEPDG), Equations 5-5 and 5-6 (ARA 2004). The mechanistic-empirical based rutting prediction models can be used for asphalt concrete in highway and airfield when specific calibration parameters are developed. Since the calibration parameters are not available for airfield pavements, the model parameters were based on the global calibration as recommended by MEDPG.



$$\text{Log}\left(\frac{\varepsilon_p}{\varepsilon_r}\right) = -3.35 + \text{Log}(K_Z) + 1.56\text{Log}(T) + 0.48\text{Log}(N) \quad (5-5)$$

Where,

$\varepsilon_p$  is plastic strain calculated at the mid-depth of a thickness increment;

$\varepsilon_r$  is incremental resilient strain at the mid-depth of a thickness increment;

$T$  is temperature at the mid-depth of a thickness increment, °F;

$N$  is number of axle load applications of a specific axle type; and

$K_Z$  is depth function.

$$RD_{AC} = \sum_{i=1}^N (\varepsilon_p)_i \Delta h_i \quad (5-6)$$

Where,

$RD_{AC}$  is rutting depth at the asphalt concrete layer;

$N$  is number of sub-layers;

$(\varepsilon_p)_i$  is vertical plastic strain at mid-thickness of layer i; and

$\Delta h_i$  is thickness of sublayer i.

The permanent deformation model of granular base was based on the laboratory tests of P-209 base material considering both static and dynamic stress effects, as shown in Equation 5-7.

$$\varepsilon_p = 0.2908 \sigma_s^{0.1391} \sigma_{3d}^{-0.4565} N^{0.0877} \quad (5-7)$$

Where,

$\sigma_s$  is static confining pressure;

$\sigma_{3d}$  is dynamic stress in radial direction; and

$N$  is number of load applications.

Due to the consideration of wandering pattern in the full-scale test at the NAPTF, given an arbitrary rutting depth model like Equation 5-8, a time-hardening equation was employed in calculating the rutting depths, Equation 5-9 (Monismith et al. 2000).

$$\varepsilon_p = a\varepsilon_r(n)^c \quad (5-8)$$

Where,

$\varepsilon_p$  is plastic strain;

$\varepsilon_r$  is elastic strain;

$n$  is number of axle load repetitions; and

$a$  and  $c$  are regression coefficients.

$$\varepsilon_{p(j)} = a_j \left[ \left( \frac{\varepsilon_{p(j-1)}}{a_j} \right)^{(1/c)} + \Delta n_j \right]^c \quad (5-9)$$

Where,

$\varepsilon_{p(j)}$  is plastic strain strain at the  $j^{\text{th}}$  hour;

$\Delta n_j$  is number of axle load repetitions at the  $j^{\text{th}}$  hour;

$a_j$  is parameter related to elastic strain at the  $j^{\text{th}}$  hour,  $a_j = 10^{-3.35} \varepsilon_{r(j)} K_Z T^{1.56}$  for the MEPDG rutting model here; and

$c$  is regression coefficient, 0.48 here.

### 5.6.2 Calculation of Rutting Depth

The rutting depth in the asphalt layer of the indoor heated pavement section was calculated and compared to the measured rutting depth. The rutting in the granular base layer was neglected due to the existence of Econcrete layer under asphalt layer. It was found that although the development trends of rutting depth are consistent, the prediction

from the MEPDG model cannot capture the tertiary stage of rutting development as observed in the full-scale test.

The increased rutting depths due to high tire pressure were shown in Figure 5.16. The rutting depths at the 400<sup>th</sup> pass were extracted before the starting of the tertiary stage. As expected, rutting depths calculated with wander pattern are smaller compared to the ones without wander pattern. The increase of rutting depth caused by higher tire pressure was found to be 0.5-0.8mm in the measurement but 1.0-1.3mm in the prediction. This considerable difference is probably caused by the fact that all parameters in the performance transfer function were based on the global calibration using long-term pavement performance (LTPP) data for highway pavements. Therefore, it suggests that specific calibration parameters should be developed in order to provide accurate prediction of rutting depth for airfield pavements.

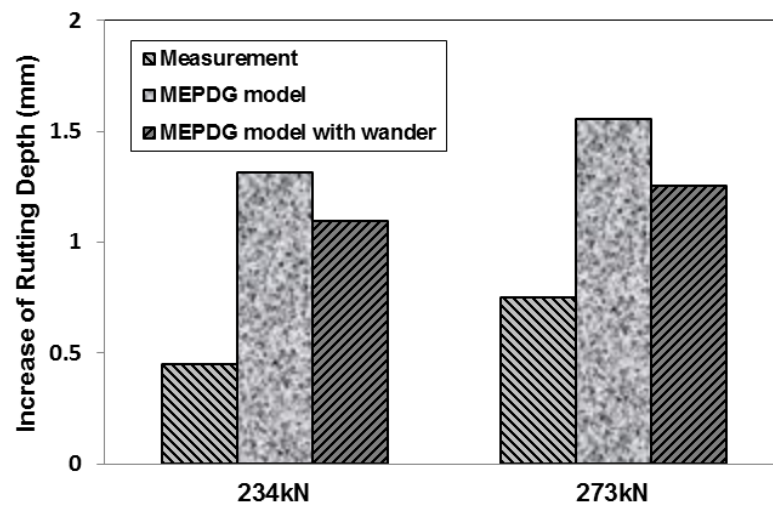


Figure 5.16 Comparison of rutting depth increase at high tire pressure for the indoor heated pavement section

The rutting depth in the HVS test section was calculated consider the rutting depth in the asphalt layer and granular base layer. The permanent deformation of subgrade was neglected due to the thick top layers and the relatively strong sand subgrade. Figure 10

compared the development trends of rutting depth are consistent between the calculated and measured results at the HVS test section. It was found that the rutting depth of asphalt layer is dominant in the total rutting depth due to high temperature. Further research will be conducted to improve the mode accuracy by considering the plastic constitutive behavior of pavement materials or developing local calibration parameters for airfield pavements.

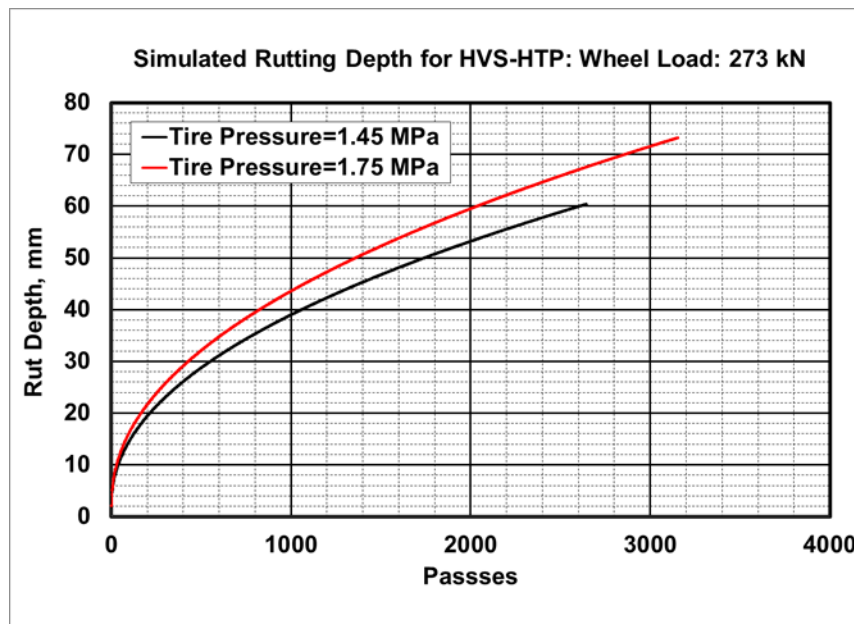


Figure 5.17 Rutting depths from simulation for the HVS test section

## 5.7 Failure Criteria for Multi-Axial Stress

In order to accurately identify the damage mechanisms of shear failure, an approach that can accurately and effectively capture multi-axial state of stresses is needed. The multi-axial stress states for ductile materials can be investigated using several failure theories. They include maximum octahedral shear stress (von Mises criterion), Equation 5-10; Mohr-Coulomb criterion, Equation 5-11; and Drucker-Prager criterion, Equation 5-12 (Doweling 1999).

$$(\sigma_1 - \sigma_2)^2 + (\sigma_2 - \sigma_3)^2 + (\sigma_1 - \sigma_3)^2 = 2\sigma_y^2 \quad (5-10)$$

$$\left(\frac{\sigma_1 + \sigma_3}{2}\right) \sin \phi - \left(\frac{\sigma_1 - \sigma_3}{2}\right) + c \cdot \cos \phi = 0 \quad (5-11)$$

$$\sqrt{\frac{1}{6}[(\sigma_1 - \sigma_2)^2 + (\sigma_2 - \sigma_3)^2 + (\sigma_1 - \sigma_3)^2]} = \frac{6c \cdot \cos \phi}{\sqrt{3}(3 - \sin \phi)} + \frac{2 \sin \phi}{\sqrt{3}(3 - \sin \phi)} (\sigma_1 + \sigma_2 + \sigma_3) \quad (5-12)$$

Where,

$\sigma_1$ ,  $\sigma_2$ , and  $\sigma_3$  are maximum, middle, and minimum principal stresses;

$\tau$  is maximum shear stress (shear strength);

$\sigma_y$  is yield stress in uniaxial tension;

$\phi$  is angle of friction; and

$c$  is cohesive strength.

The Mohr-Coulomb failure criterion is widely used in soil mechanics. Asphalt mixtures are composed of aggregate, asphalt, and air, so it resembles to soils composed of soil solids, water, and air. It was known that the asphalt concrete may be modeled as Mohr-Coulomb materials with both cohesive and granular properties at intermediate-to-high temperatures. The Drucker-Prager model is a smooth version of the Mohr-Coulomb model because it modifies the Mohr-Coulomb yield function to avoid singularities associated with corners. However, both Mohr-Coulomb and Drucker-Prager criteria are pressure dependent models assuming the compressive strength of the material is much greater than its tensile strength.

The Mohr-Coulomb theory is usually represented by using Mohr's circles, as shown in Figure 5.18 (a). Instead of plotting a series of Mohr's circles, it is mathematically convenient to plot the states of stress as points in a  $p-q$  diagram, as shown in Figure 5.18 (b). The Mohr-Coulomb failure envelope with strength parameters ( $c$  and  $\phi$ ) can be defined by Equations. 5-13 and 5-14.

$$\tau = c + \sigma \tan \phi \quad (5-13)$$

$$q = a + p \tan \alpha \quad (5-14)$$

$$\text{Stress Ratio} = \frac{q}{q_{failure}} = \frac{q}{a + p \tan \alpha} = \frac{\sigma_1 - \sigma_3}{2c \cdot \cos \phi + (\sigma_1 + \sigma_3) \sin \phi} \quad (5-15)$$

with  $c \cdot \cos \phi = a$  and  $\sin \phi = \tan \alpha$

Where,

$\tau$  is shear stress at failure (shear strength);

$\sigma$  is normal stress at failure;

$p$  is normal stress at failure with  $p = (\sigma_1 + \sigma_3) / 2$ ;

$q$  is shear stress at failure with  $q = (\sigma_1 - \sigma_3) / 2$ ;

$\phi$  is angle of friction; and

$c$  is cohesive strength.

The failure of a material based on the Mohr-Coulomb failure criterion will initiate as the Mohr's circle reaches its failure envelope. Therefore the closeness of the stress state point to the failure envelop can be expressed by Equation 5-15 to measure how critical a point in multi-axial stress state behaves.

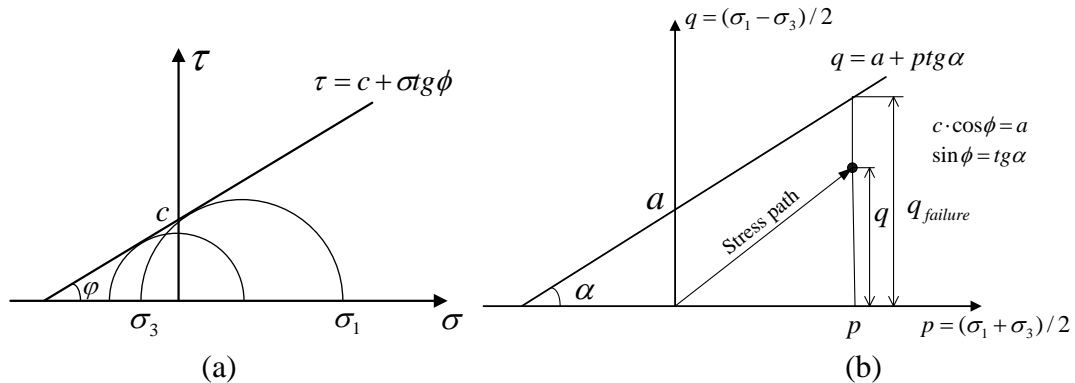


Figure 5.18 Representations of Mohr-Coulomb failure criterion in (a) Mohr's circles and (b) p-q diagram (compression: positive and tension: negative)

The shear strength of asphalt concrete is affected by both cohesion strength and frictional resistance. The cohesion strength is mainly determined by the viscous

properties of asphalt binder, while the friction angle is dominated by aggregate morphology and gradation. The cohesive strength and friction angle in the Mohr–Coulomb criteria are typically obtained from tri-axial strength tests conducted at various confinement levels in many studies (Hajj et al. 2007). In this study, the cohesion strength was estimated to be 901 kPa with regard to fixed friction angle of  $30^\circ$  based on the high-temperature performance-grade of asphalt binder and aggregate gradation used in the asphalt mixture (Gokhale et al. 2005).

It is reasonable to directly apply the Mohr-Coulomb failure criterion expressed in Equation 5-9 to examine the interface failure between asphalt layers. The interface shear strength between asphalt layers depends on tack coat type and residual application rate, temperature, confinement (normal pressure), surface condition (such as texture, milled or smooth surface), and moisture condition (Romanoschi and Metcalf 2001; Mohammad and Elseifi 2012). In this study, the interface cohesion strength is 140kPa with the friction angle of  $36^\circ$  were used in the analysis considering the relatively high temperature (Canestrari et al. 2005).

## **5.8 Effect of Aircraft Maneuvering on Pavement Near-Surface Failure**

### *5.8.1 Effect of Aircraft Maneuvering on Near-Surface Responses*

The analysis was conducted using the pavement structure in the indoor heated pavement section. In this study, the typical summer condition at New Jersey was characterized using the climate parameters extracted from the Long-Term Pavement Performance (LTPP) database. The BELLS2 equation was used to model temperature profile along the depth of asphalt pavement (FHWA 2000). Figure 1 shows the pavement structure and the temperature profile in the asphalt layer used in the analysis. The in-depth distribution of temperature is decreasing along depth from  $37^\circ\text{C}$  to  $33.5^\circ\text{C}$ , where the average pavement temperature is around  $35^\circ\text{C}$ , as shown in Figure 5.19.

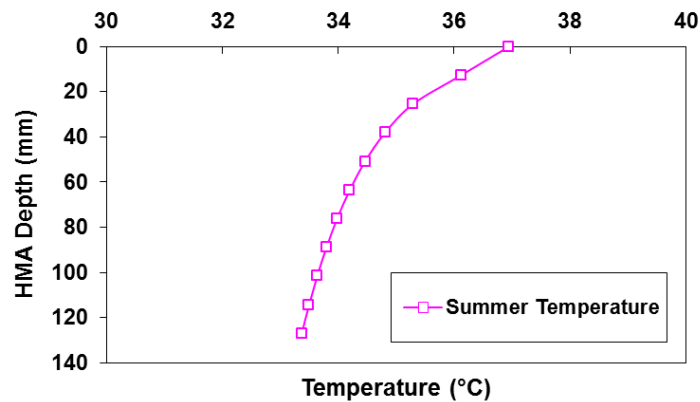
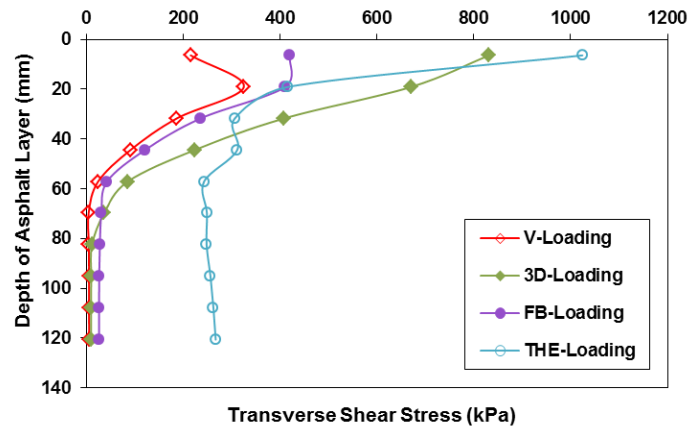


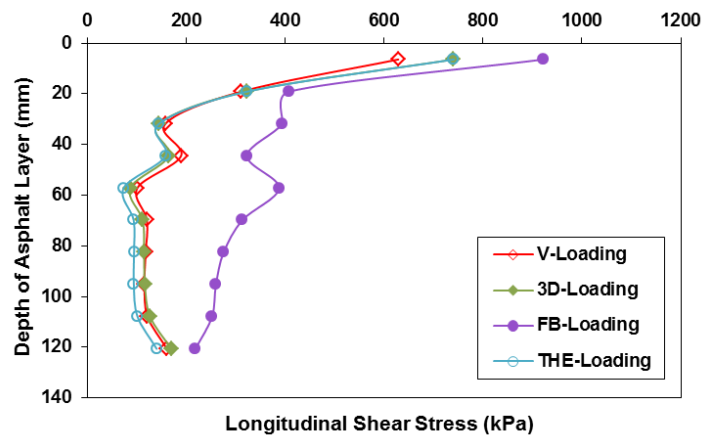
Figure 5.19 Temperature profile in the modeled pavement under aircraft maneuvering

In order to evaluate shear failure potential in the asphalt layer, the maximum shear stresses along the depth of asphalt layer were first plotted, respectively, for transverse and longitudinal shear stresses, as shown in Figure 5.20. The maximum transverse shear stresses were obtained when the tire loading was directly above the point of interest; while the maximum longitudinal shear stresses were obtained when the tire was approaching or leaving the point of interest. It was found that aircraft turning caused the greatest transverse shear stresses; while aircraft braking induced the greatest longitudinal shear stresses at the surface of asphalt layer. On the other hand, as compared to the loading with only vertical contact stresses, the 3-D contact stresses shifted the maximum transverse shear stress from shallow-depth to near-surface and increased the stress magnitude significantly.





(a)



(b)

Figure 5.20 In-depth distributions of maximum shear stresses (a) at transverse direction and (b) along traffic direction

The in-depth distribution of shear stresses proved that shear stresses mainly concentrated in the upper asphalt layer. Due to the effect of confinement stress along the depth, the shear failure potential need be evaluated considering the multi-axial stress state. Figure 5.21 presents all the stress states at pavement near-surface within the upper 50-mm of asphalt layer. Three locations of interest were selected and compared in terms of the horizontal distance away from the center of aircraft tire. The data show that the critical locations of shear failure were at pavement near-surface under tire edges where

the normal stresses may not reached the maximum values. This observation is in agreement with the definition in Mohr-Coulomb criterion that the smaller normal stress would probably lead to the greater shear failure potential. The stress states are closer to the failure envelope under the loading caused by aircraft turning or braking due to the effects of tangential contact stresses. It is noted that aircraft turning caused the shear stresses at one side of tire edges were significantly greater than the stresses at the other side.

The shear failure in the bulk asphalt material may appear as shear-induced deformation or cracking. Due to high cohesion, asphalt concrete may prevent shearing by dilation and developing secondary tension that could result in micro-cracks. After that, visible cracks are more likely to develop in the absence of higher confinement that keeps the micro-cracks closed (Song and Pellinen 2007).

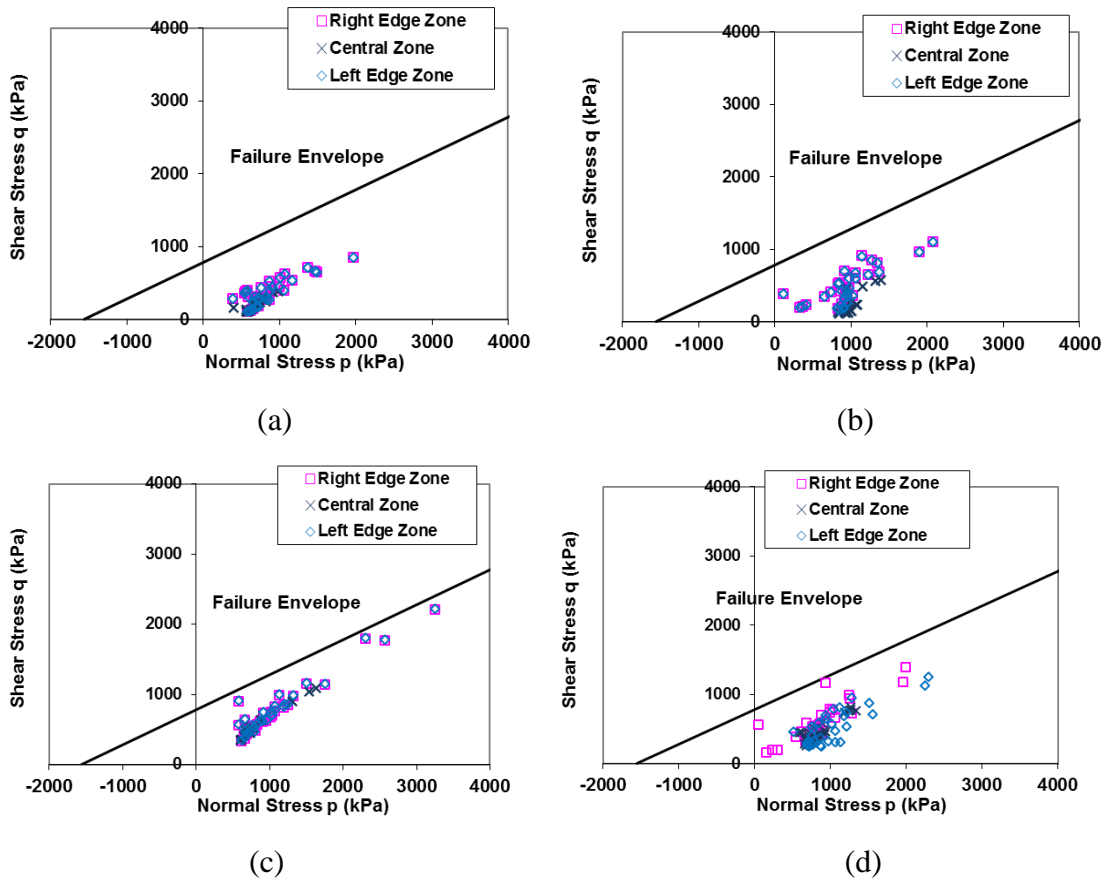


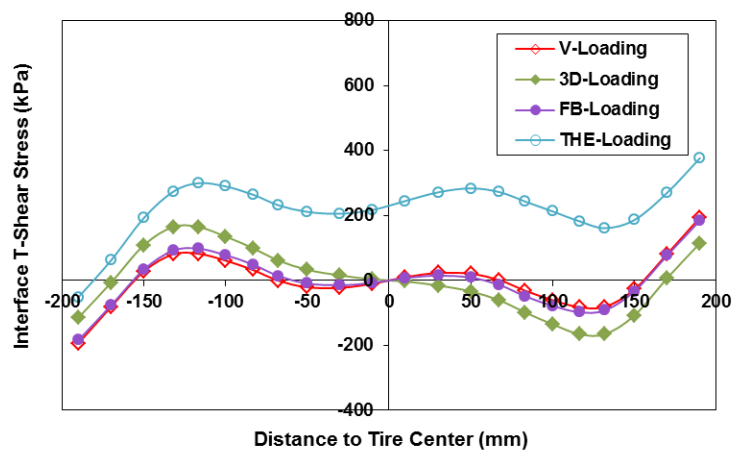
Figure 5.21 Stress states at pavement near-surface under (a) V-Loading; (b) 3D-Loading; (c) FB-Loading; and (d) THE-Loading

### 5.8.2 Effect of Aircraft Loading on Interface Responses

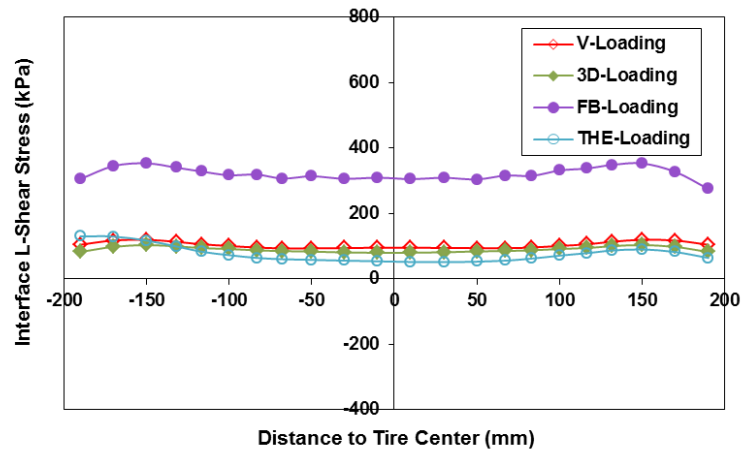
The interface failure potential between asphalt layers was investigated at the 50mm (2in.) below the pavement surface. The distributions of maximum interface stresses along the tire contact width were plotted in Figure 5.22, respectively, for transverse and longitudinal shear stresses and normal (compression) stresses. The transverse shear stress is perpendicular to the moving direction, while the longitudinal shear stress is parallel to the moving direction. The maximum normal stress and transverse shear stress were obtained when the tire loading was directly above the point of interest. However, the maximum longitudinal shear stress was obtained when the tire was approaching or

leaving the point of interest. On the other hand, the transverse shear stresses have the maximum values at tire edges with opposite directions at each side except the case of aircraft turning; while the longitudinal shear stresses kept relatively constant along tire contact width.

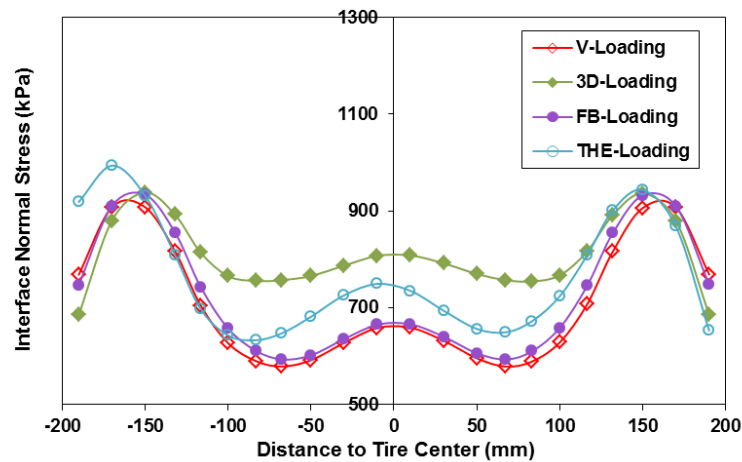
The results in Figure 5.22 also show that the aircraft turning induces much greater transverse shear stresses compared to other tire rolling conditions. The transverse shear stresses were concentrated toward one direction due to the centripetal effect, which were different from the asymmetric stress distributions caused by other loading conditions. However, aircraft braking induces the maximum longitudinal interface shear stresses due to the high friction force. Variations in normal (vertical) interface stresses were observed among different aircraft maneuvering operations. The greatest normal stresses were induced by the free rolling taxiing; while aircraft turning or braking results in relatively lower normal stresses under tire center area. This indicates that aircraft turning or braking can increase the interface shear failure potential due to the greater shear stresses and the lower normal stresses (less confinement).



(a)



(b)



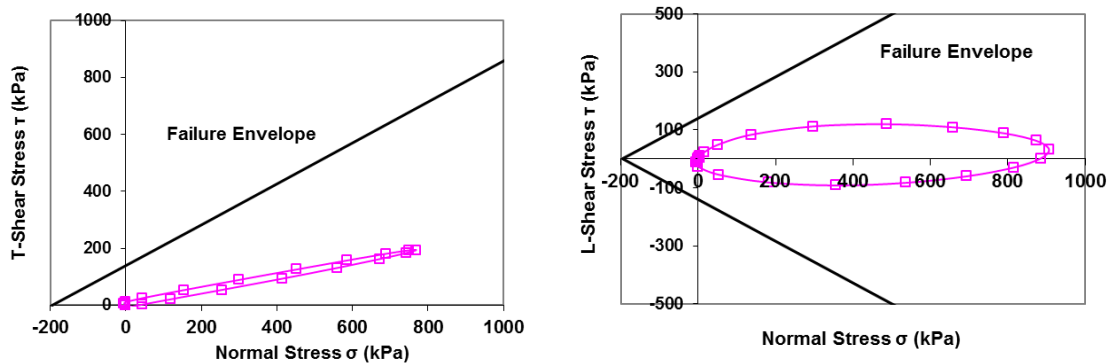
(c)

Figure 5.22 Distributions of (a) transverse shear stress; (b) longitudinal shear stress; and (c) normal stress at the interface along tire contact width

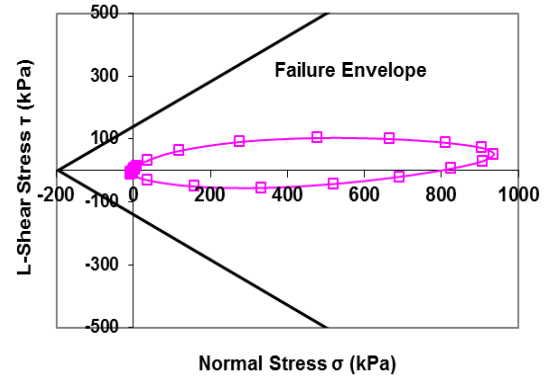
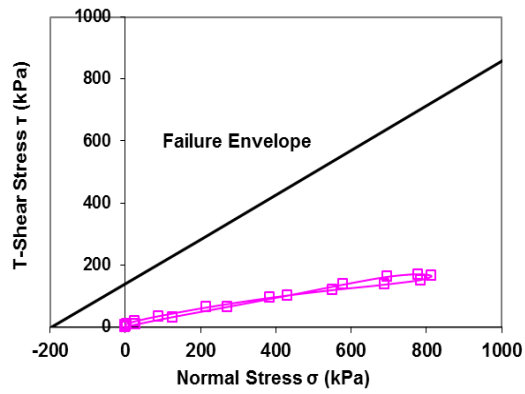
Figure 5.23 presents the transverse and longitudinal shear stress paths at the interface under different aircraft maneuvering operations. It shows that the loading and unloading stress paths for the transverse shear stresses are nearly the same under moving loads. For the longitudinal shear stress, an elliptical loop was developed due to the opposite directions of shear stress as the tire was approaching and leaving. In the free rolling

condition, although the transverse shear stresses were greater than the longitudinal shear stress, the longitudinal shear stresses cause the greater failure potential because the maximum longitudinal shear stress was induced at the stress state with the smaller normal stress (vertical confinement). This clearly indicates the importance of considering multi-axial stress states in prediction of shear failure potential at the interface.

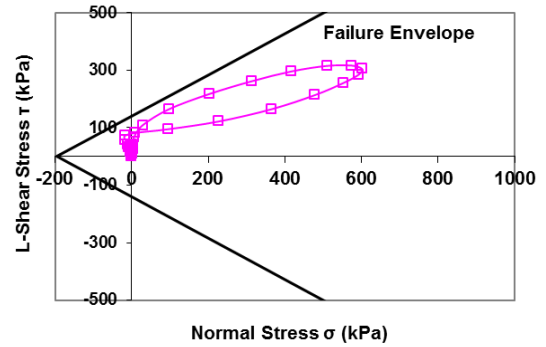
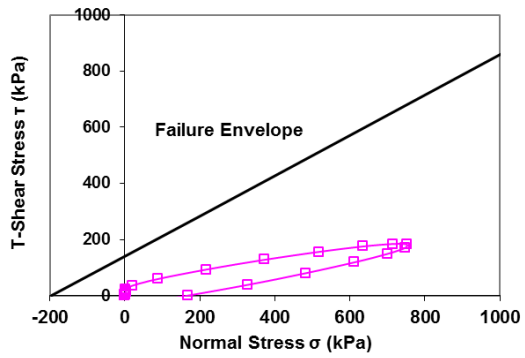
The results in Figure 5.23 show that aircraft braking caused the one-directional longitudinal shear stresses and increased shear failure potential as the tire approaching the point of interest; while aircraft turning increases shear failure potential caused by the transverse shear stresses. It is worth mentioning that the critical shear stress paths were found under different ribs of the aircraft tire. For the free rolling condition, the critical stresses were located under the edge ribs of aircraft tire; while the critical stresses were located under central ribs for the braking condition and under intermediate ribs for the turning condition. This emphasizes again that the interface shear failure potential would occur at the locations where the greater interface shear stresses were induced associated with the lower normal stress or less confinement.



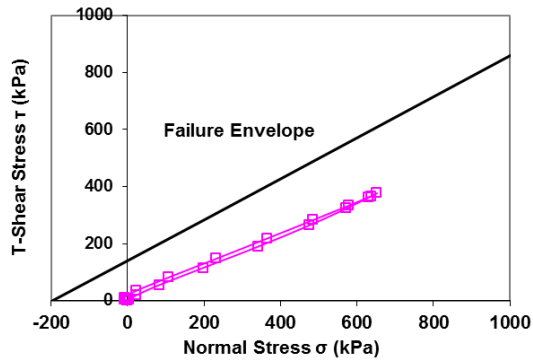
(a)



(b)



(c)



(d)

Figure 5.23 Critical stress paths at interface under (a) V-Loading; (b) 3D-Loading; (c) FB-Loading; and (d) THE-Loading

### *5.8.3 Effect of Aircraft Loading on Critical Stress Ratios*

Critical shear stresses and stress ratios at different aircraft loading conditions (maneuvering operations, weight, and speed) were compared in Table 5.9. For comparison, pavement responses under aircraft loading during takeoff and at a low operating speed were also calculated. The data clearly show that aircraft turning and braking increase the shear failure potential both in the bulk asphalt material and at the layer interface. The aircraft braking condition causes the similar stress ratio in the bulk asphalt material but the much greater stress ratio at the layer interface than the aircraft turning condition. This indicates that aircraft braking is the most critical loading condition for shear failure of airfield pavements. The effects of aircraft turning or braking were found more significant for shear failure at the layer interface than in the bulk asphalt material.

On the other hand, it was found that the increased aircraft weight at takeoff and the lower operation speed only caused the slightly greater shear failure potential as compared to the effects of aircraft ground maneuvering. The results indicate that the shear failure potential in airfield asphalt pavements is more affected by aircraft ground maneuvering, rather than aircraft weight and operating speed. This is different from the traditional observation that the airfield pavement responses, such as tension at the bottom of asphalt layer or compression on top of subgrade, are sensitive to the wheel load and speed (Garg and Hayhoe 2001). This finding could be only observed when the failure criteria under the multi-axial stress state were considered in the analysis.



Table 5.9 Critical Shear Stresses and Stress Ratios at Different Aircraft Loading Conditions

Indicator of Shear Failure Potential	B737 Aircraft landing at 37 km/h			
	Free Rolling (V-Loading)	Free Rolling (3-D Loading)	Full Braking	Turing
Critical shear stress at near-surface (kPa)	629 (L*)	832 (T*)	922 (L)	1020 (T)
Stress-ratio at near-surface	0.48	0.67	0.92	0.93
Critical shear stress at layer interface (kPa)	242 (T)	170 (T)	353 (L)	429 (T)
Stress ratio at layer interface	0.28	0.23	0.78	0.47
Indicator of Shear Failure Potential	B737 Aircraft at free rolling (3-D contact stresses)			
	Landing at 37km/h	Landing at 3.7km/h	Takeoff at 37km/h	Takeoff at 3.7km/h
Critical shear stress at near-surface (kPa)	832 (T)	803 (T)	990 (T)	956 (T)
Stress-ratio at near-surface	0.67	0.68	0.73	0.75
Critical shear stress at layer interface (kPa)	170 (T)	195 (T)	203 (T)	232 (T)
Stress ratio at layer interface	0.23	0.26	0.24	0.26

\*L: longitudinal (along traffic direction); T: transverse.

## 5.9 Summary

This chapter mainly focuses on the non-uniform contact stress distribution induces greater transverse (critical) tensile strains, shear strains and compressive strains in the asphalt layer, than both area-based and pressure-based uniform contact stress distributions. This emphasizes the importance of considering tire-pavement interaction in airfield pavement analysis. As compared to the moving loading, the stationary loading method could predict the greater or smaller strain responses depending on the moving

speed. As the stationary loading is applied, the small differences in the loading duration may cause considerable differences in the strain responses in the asphalt layer. Applying average temperature profile in summer is a conservative approach for predicting fatigue cracking potential; however, it underestimates rutting or near-surface cracking potential in the airfield pavement. In general, the results show that strain responses at the upper HMA layer seem more sensitive to the change of temperature profile. With the same increasing ratio, the increase of tire load causes greater change of maximum strain responses compared to the increase of tire inflation pressure. This suggests that the tire load behaves as a predominant factor affecting airfield pavement service life. As the MEDPG performance transfer function is used, the predicted rutting depth in the asphalt layer increase due to high tire pressure is greater than the one obtained from the full-scale test. It suggests that specific calibration parameters should be developed to provide accurate prediction of rutting depth for airfield pavements.

Airfield pavement responses at the near-surface were affected by the non-uniform distributions of 3-D tire-pavement contact stresses that varied depending on different tire rolling conditions under aircraft ground maneuvering operations. The multi-axial stress state criterion was proven effective to evaluate the shear failure potential at airfield asphalt pavements under the combined loading of normal stresses and shear stresses. Aircraft braking or turning significantly increases the shear failure potential in the bulk material and at the asphalt layer interface due to the tangential stresses applied on pavement surface. The effects of aircraft weight and operating speed on pavement shear failure were limited compared to aircraft maneuvering. The analysis of stress states in the asphalt layer sheds light on the requirement of shear strength and selection of laboratory tests for evaluation of shear failure potential at airfield asphalt pavements. The cohesion strength of asphalt concrete plays an important role in preventing shear failure because aircraft ground maneuvering causes significant amounts of tangential stresses applied on pavement surface that increases the shear stress at the small confinement. Appropriate laboratory test setup should be able to simulate in-situ pavement stress states under

critical loading conditions, such as the triaxial test or hollow cylinder test with confinements.

## **CHAPTER 6 AIRFIELD PAVEMENT RESPONSES UNDER MULTI-WHEEL GEAR LOADING**

### **6.1 Full-Scale Pavement Testing**

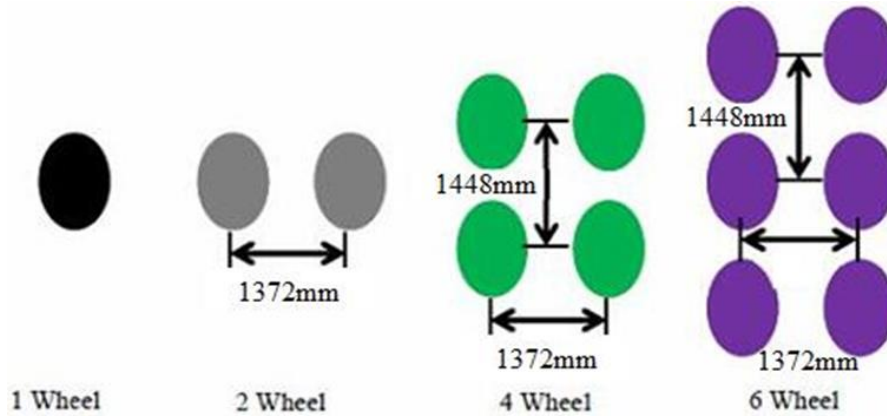
#### *6.1.1 Test Sections and Loading Conditions*

The primary purpose of the NAPTF is to generate full-scale pavement response and performance data for development and verification of airport pavement design criteria. The test facility consists of a 274.3m (900ft) long by 18.3m (60ft) wide test pavement area, embedded pavement instrumentation, environmental instrumentation, static and dynamic data acquisition system, and a test vehicle with up to twelve aircraft tires at single wheel load of up to 34tonnes (75,000lbs). Additional information about the test facility is available elsewhere (FAA 2015).

A pavement construction cycle at the NAPTF includes pavement instrumentation, traffic testing to failure, post-traffic testing (includes trenching activities and other tests), and pavement removal. CC7 consists of flexible testing pavements built on both the north and south side over subgrades of different strengths. The north side testing sections (LFP-1N, LFP-2N, LFP-3N, and LFP-4N) will be the focus of discussion in this paper. Pavement cross-sections and loading configuration are shown in Figure 6.1. The construction material met P-401 specifications for asphalt concrete and P-154 (uncrushed stone) for subbase layer (FAA 2014). PG 76-22 binder was used in the asphalt layer.

LFP-1	LFP-2	LFP-3	LFP-4
15 inch P-401	12 inch P-401	10 inch P-401	8 inch P-401
34 inch P-154 Subbase Course	37 inch P-154 Subbase Course	39 inch P-154 Subbase Course	41 inch P-154 Subbase Course
Subgrade CBR 5-6 DuPont Clay	Subgrade CBR 5-6 DuPont Clay	Subgrade CBR 5-6 DuPont Clay	Subgrade CBR 5-6 DuPont Clay

(a)



(b)

Figure 6.1 Accelerated Pavement Testing information: (a) pavement cross-sections and (b) aircraft gear configurations

The response testing was performed on the four pavement sections utilizing the test vehicle with four multiple-wheel configurations, as shown in Figure 6.1 (b). The lateral wheel spacing is 1372mm (54in.) and the longitudinal wheel spacing is 1448mm (57in.), respectively. Several different traffic speeds and loading levels were incorporated into the response testing. The traffic speeds of 0.5mph, 1.16mph, and 4mph were employed in the accelerated pavement testing along with three loading levels of 12kips, 24kips, and 36kips.

### 6.1.2 H-bar Strain Gauge Responses

H-bar asphalt strain gages (ASGs) were imbedded at the bottom of asphalt layer under the wheel loading paths, as shown in Figure 6.2. The data of asphalt strain gauge (ASG) were monitored and collected during the response testing (Li et al. 2016). The critical (transverse) tensile strains measured at 4mph were presented here.



Figure 6.2 Pavement instrumentation: (a) layout and (b) protection of asphalt strain gauges

Figure 6.3 (a) and 6.3 (b) represent the measured transverse strains at LFP-1N (15-inc. asphalt layer) and LFP-3N (10-in. asphalt layer) sections under two-wheel loading gear. The time history of tensile strains first increases to the peak value and then drops to the level with certain residual strains, as the two-wheel loading was approaching and leaving, respectively. As expected, the maximum tensile strains of LFP-1N are smaller than LFP-3N due to the thicker asphalt layer.

Figure 6.3 (c) and (d) show the strain responses of LFP-1N and LFP-3N under six-wheel loading. The time history of tensile strains includes a climbing stage with triple peak values and a decreasing stage ending up with residual strains, as the 6-wheel loading was approaching and leaving, respectively. The greatest tensile strain was induced by the third wheel groups as the tensile strain from the first and second wheel groups are not fully recovered. Similarly, the thinner asphalt concrete (LFP-3N) would have the greater tensile strain.

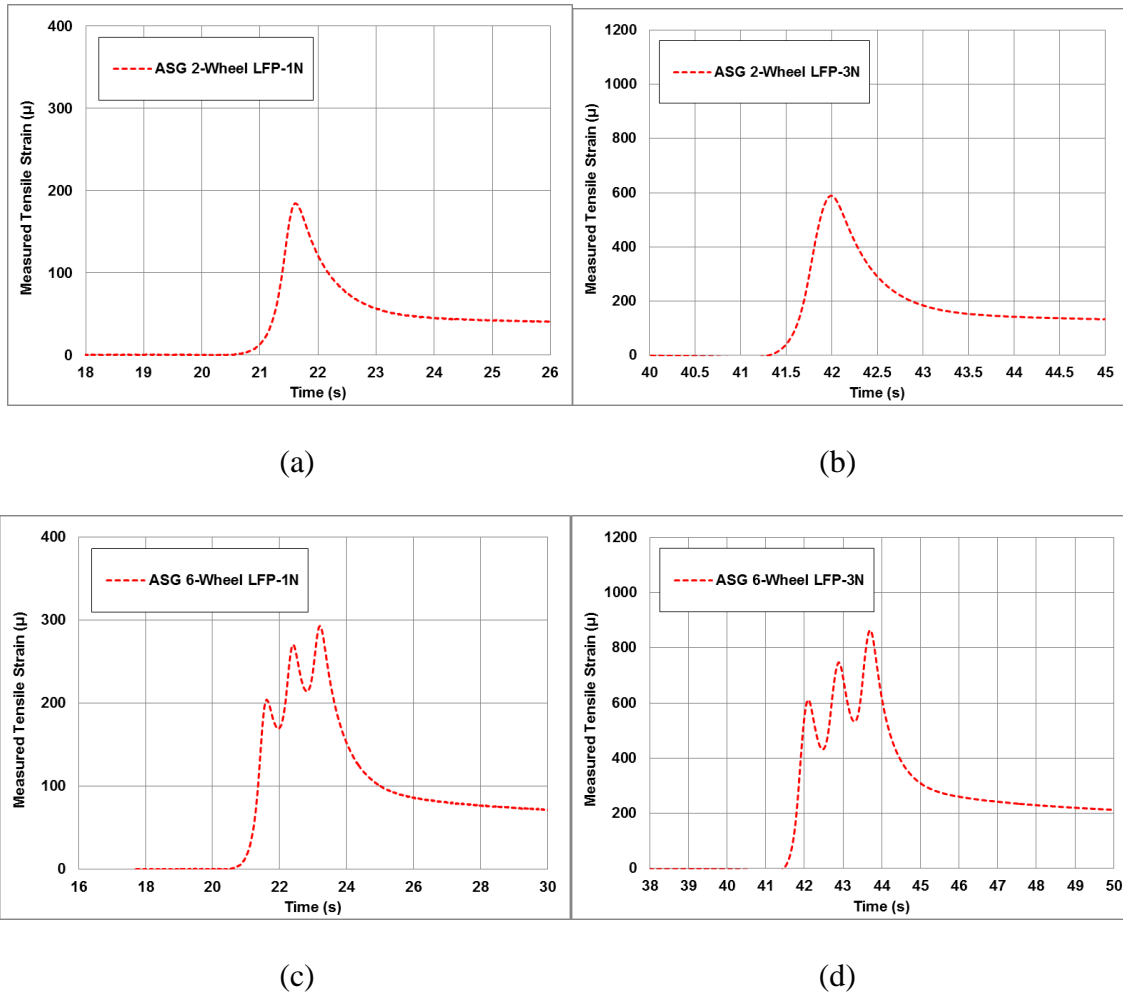


Figure 6.3 Response testing results from strain gauge at 36-kip loading: (a) LFP-1N under 2-wheel gear configuration; (b) LFP-3N under 2-wheel gear configuration; (c) LFP-1N under 6-wheel gear configuration; and (d) LFP-3N under 6-wheel gear configuration

## 6.2 Multi-Wheel Loading Simulation and Response Analysis

### 6.2.1 FE Model Validation for Multi-Wheel Loading

Three gear configurations (2-wheel, 4-wheel, and 6-wheel) were simulated which are the same as the ones used in the test vehicle. A continuous moving loading method was

used to simulate the vehicular aircraft loading. The tire loading pattern possesses a half-sinusoidal distribution longitudinally and a non-uniform distribution laterally under each rib of the tire. The inflation tire pressure was set as 1.75MPa (254psi) and the non-uniform tire contact stress distribution is based on field measurements reported in the literature (Rolland 2009). The peak contact stresses under edge tire ribs were assumed twice tire inflation pressure, while the peak contact stresses beneath central tire ribs were assumed 1.1 times tire inflation pressure. The compressive stresses applied on pavement surface under six-wheel (dual-tridem) gear configuration are shown in Figure 6.4. More details on 3-D FE models and tire contact stresses can be obtained elsewhere (Wang 2011; Wang et al. 2015; Wang et al. 2014; Wang et al. 2016; Wang et al. 2017).

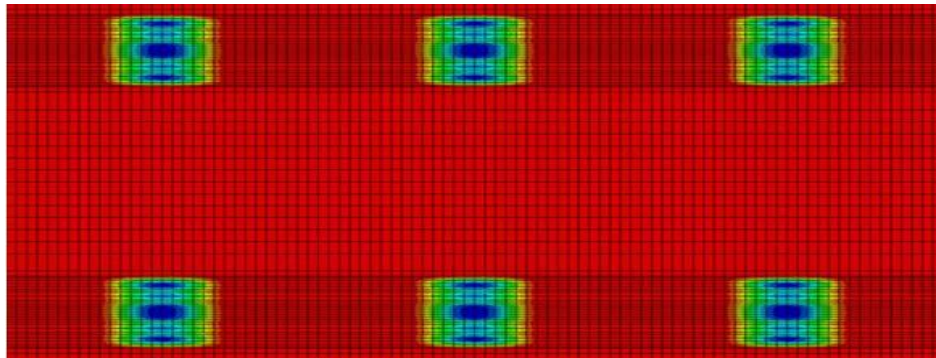


Figure 6.4 Illustration of FE model for (a) pavement structure with moving loading pattern; and (b) compressive stresses on pavement surface under six-wheel loading

Two pavement sections with different asphalt layer thicknesses (381mm [15in.] at LFP-1N and 254mm [10in.] at LFP-3N) were considered in the analysis. The model validation procedure was conducted to exhibit the capability of the developed 3-D FE models as compared to the measurements from the responses testing conducted at the NAPFT. As shown in Figure 6.5, the peak values matched well between the calculated and measured tensile strains for LFP-1N and LFP-3N sections under different gear loading configurations. Some discrepancies were observed for the measured and calculated strain-time histories.



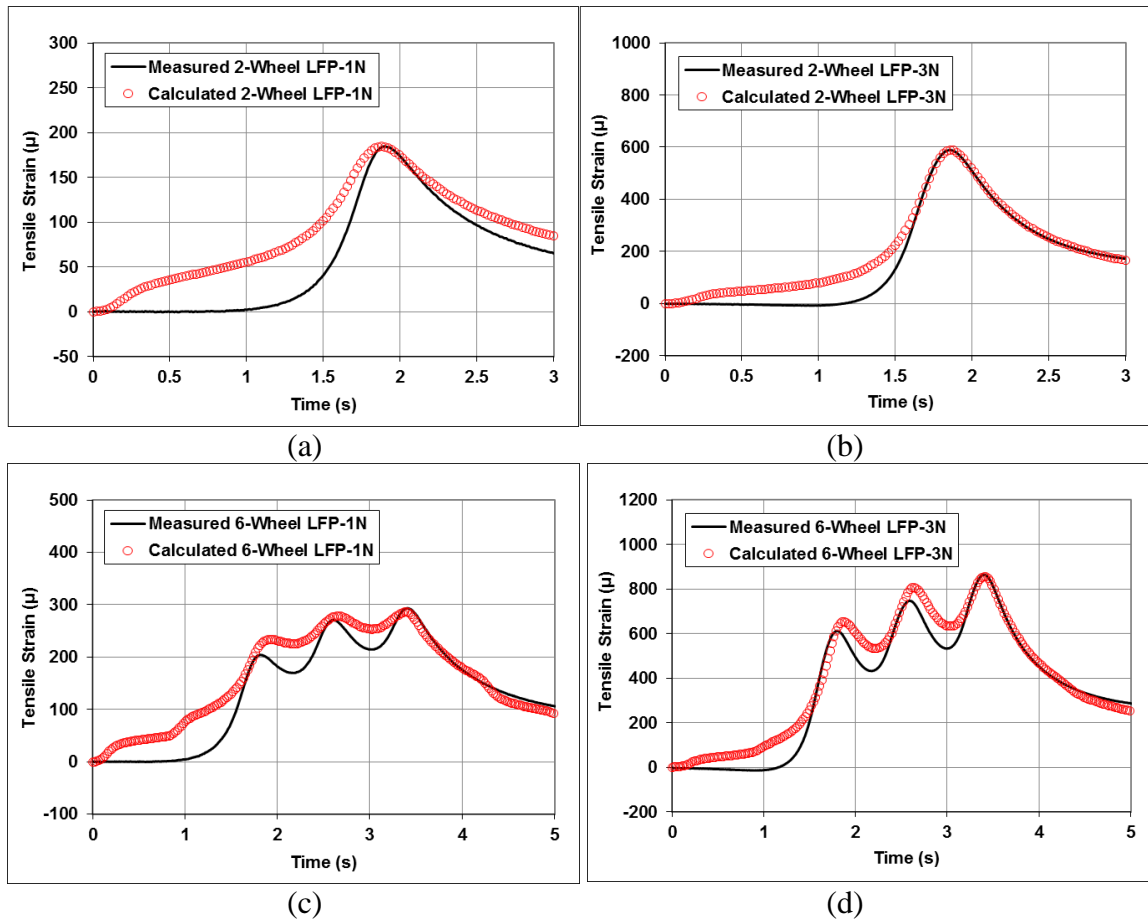


Figure 6.5 Validation of FE models with response testing results by 36-kip aircraft loading: (a) LFP-1N under 2-wheel gear configuration; (b) LFP-3N under 2-wheel gear configuration; (c) LFP-1N under 6-wheel gear configuration; and (d) LFP-3N under 6-wheel gear configuration

The calculated peak values of tensile strains at different pavement sections were compared to the measured results from full-scale testing under different multi-wheel gear configurations, as shown in Figure 6.6. Different loading levels and varying numbers of multi-wheel loading were considered in the validation. The root mean square errors (RMSEs) were calculated using Equation 6-1 to verify the accuracy of calculation results. The RMSE between calculated and measured tensile strains were found around 5%,

which indicated that the FE models can produce relatively accurate results in comparison to field measurements.

$$y_{rms} = \sqrt{\frac{1}{n} \sum \left( \frac{y_i - y_m}{y_m} \right)^2} \quad (6-1)$$

Where,

$y_{rms}$  is root mean square error (RMSE) between calculated and measured results;

$y_i$  is calculated results;

$y_m$  is measured results; and

$n$  is number of measured points.

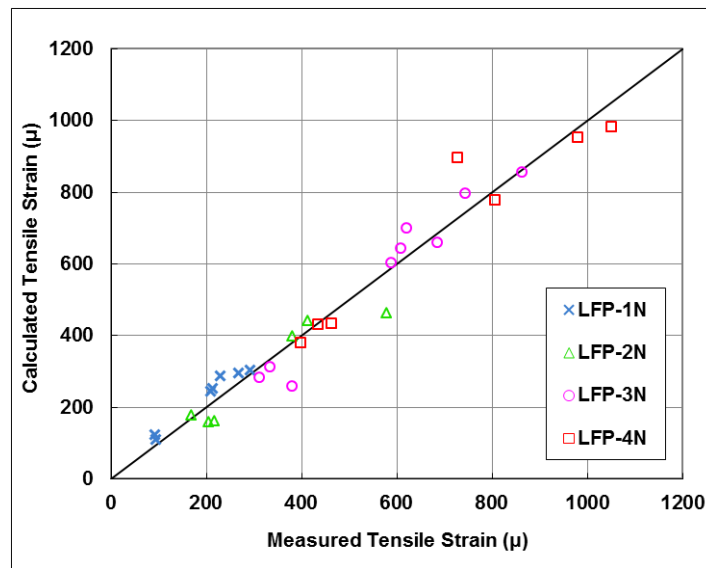


Figure 6.6 Validation results for critical tensile strains from 3-D FE models

### 6.2.2 Multi-Wheel Loading Effect on Fatigue Cracking Potential

Tensile strains at the bottom of asphalt layer were responsible for causing bottom-up fatigue cracking. The validated 3-D models were used to calculate the time histories of transverse and longitudinal tensile strains under varying multi-wheel gear loading conditions, as shown in Figure 6.7. The loading magnitude on each wheel was selected at 61.3kips that is the heavy wheel load encountered by the new generation of aircraft, like

A380 and B777. The average temperature in the AC layer was around 20°C and the moving speed was 4mph.

In general, the time histories of transverse and longitudinal tensile strains have different peak values depending on the numbers of wheels. The transverse tensile strains keep increasing as the wheels approach and then decrease with the unrecovered tensile strain as the wheels leave. The longitudinal tensile strains follow a different trend from the transverse ones. The longitudinal tensile strains have compressive strains before the wheels approach and can fully recover between the intervals of arriving wheels.

Figure 6.7 (a) and (c) show that the maximum transverse tensile strains are increased as the number of loading wheels increases. On the other hand, Figure 6.7 (b) and (d) show that the changes of peak values are not obvious by varying loading gear configuration for longitudinal tensile strains. Due to the greater magnitudes, the transverse tensile strains were considered as critical tensile strains in the asphalt layer.

The effects of asphalt layer thickness on tensile strains were observed by comparing tensile strains at two pavement sections. The significant influence of asphalt layer thicknesses on the peak values of transverse tensile strains were found as shown in Figure 6.7 (a) and (b), as compared to the longitudinal tensile strains in Figure 6.7 (c) and (d). It means that transverse tensile strains are more sensitive to the variations of asphalt layer thicknesses. The critical tensile strain decreases by around 60% as the asphalt layer thickness increases from 254mm (10 in.) to 381mm (15 in.).

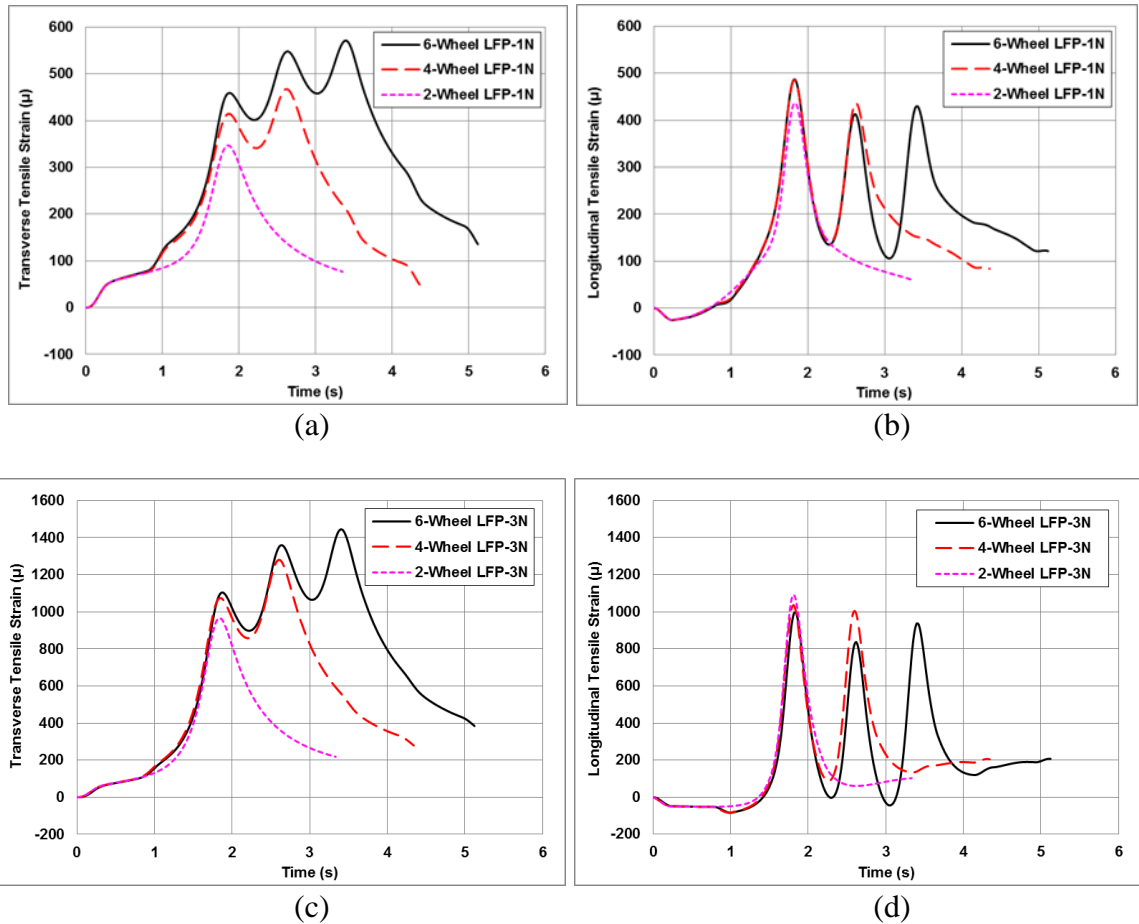


Figure 6.7 Time histories of tensile strains at the bottom of asphalt layer: (a) transverse strains in LFP-1N and (b) longitudinal strains in LFP-1N; (c) transverse strains in LFP-3N; and (d) longitudinal strains in LFP-3N

To better understand the effect of loading gear configuration on critical tensile strains in the asphalt layer, transverse distributions of tensile strains along the distance to loading center in LFP-3N is shown in Figure 6.8. Both maximum transverse and longitudinal tensile strains are located at the bottom of asphalt layer directly below each loading wheel. It is noted that transverse compressive strains were observed under the loading center, which is due to the large lateral distance between wheels. On the other hand, longitudinal tensile strains show much smaller variation along the distance to loading center.

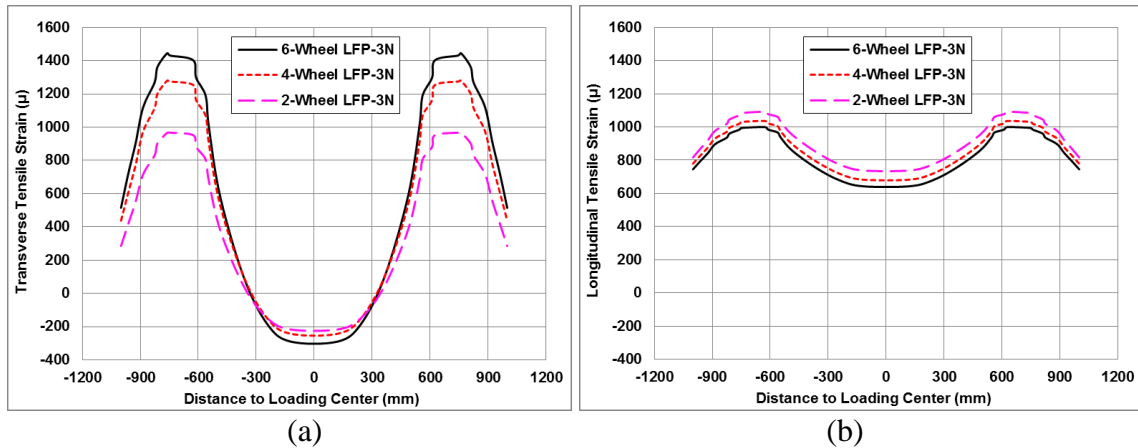


Figure 6.8 Transverse distributions of tensile strains in LFP-3N: (a) transverse strains and (b) longitudinal strains

### 6.2.3 Multi-Wheel Loading Effect on Near-Surface Cracking Potential

The near-surface cracking failure is represented by critical shear strains at the shallow depth of asphalt layer. The critical shear strains under tire edges under varying multi-wheel gear loading conditions are shown in Figure 6.9, respectively, for transverse and longitudinal shear strains. The loading magnitude on each wheel was 61.3 kips. The average temperature in the AC layer was around 20°C and the moving speed was 4 mph.

The results show that the time histories of transverse and longitudinal shear strains have different peak values due to varying gear configurations. The transverse shear strains keep increasing before each maximum values and then become decreasing after the maximum values along the time histories. However, the longitudinal shear strains follow a different trend from the transverse ones. The longitudinal shear strains show the reverse pattern (opposite direction) during the arrival of successive wheels.

Figure 6.9 (a) and (c) show that the maximum transverse shear strains increased due to the increasing number of loading wheels. However, Figure 6.9 (b) and (d) show that the changes of peak values for longitudinal shear strains are insensitive to the varying gear configuration. Comparably, the transverse shear strains were considered as critical shear strains in the asphalt layer.

The effects of asphalt layer thickness on shear strains are also shown in Figure 6.9. More influence of AC thicknesses is found on the maximum transverse shear strains in Figure 6.9 (a) and (b) than on the maximum longitudinal shear strains in Figure 6.9 (c) and (d). It concludes that the transverse shear strains are more sensitive to the variations of AC thicknesses. The critical shear strain decreases by around 30% as the asphalt layer thickness increases from 254mm (10 inches) to 381mm (15 inches).

The in-depth distribution of shear strains along the asphalt layer thickness in LFP-3N is shown in Figure 6.9. The transverse shear strains have the maximum value at 50mm (2 inches) below pavement surface; while longitudinal shear strains have the maximum value around the mid-depth of asphalt layer. The results show that transverse shear strains are more sensitive to varying gear configurations.

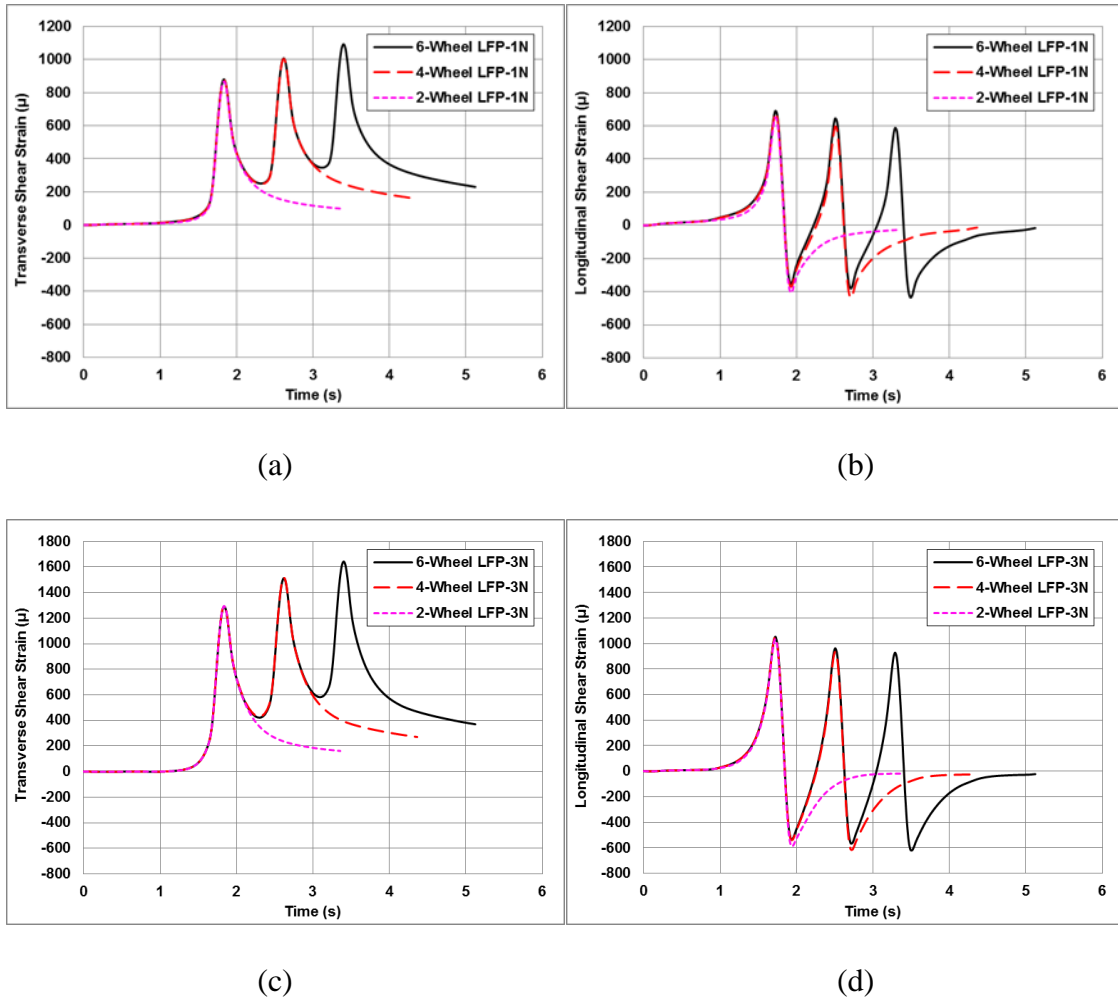


Figure 6.9 Time histories of near-surface shear strains: (a) transverse strains in LFP-1N and (b) longitudinal strains in LFP-1N; (c) transverse strains in LFP-3N; and (d) longitudinal strains in LFP-3N

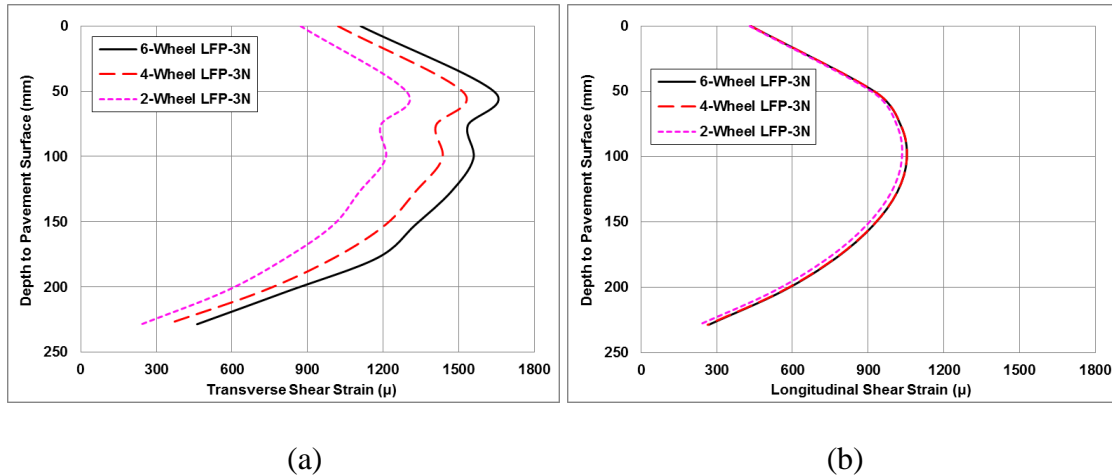


Figure 6.10 In-depth distribution of near-surface shear strains in LFP-3N: (a) transverse strains; and (b) longitudinal strains

#### 6.2.4 Effect of Loading Magnitude

The loading magnitudes were considered as a major factor affecting failure potential of airfield pavement. The critical strain responses in the asphalt layer under different loading levels are shown in Figure 6.11, respectively, for LFP-1N and LFP3N sections. The loading levels are 53kN (12kips), 160kN (36kips), and 272kN (61kips) on each wheel. The average temperature in the asphalt layer was around 20°C and the moving speed was 4mph. In general, both critical tensile and shear strains increase with the increasing loading levels. However, the changing rates of the trend lines vary depending on the type of responses and asphalt layer thicknesses. The shear strain increases more rapidly as the load level increases as compared to the tensile strain; while the thinner asphalt layer is more sensitive to the loading level as compared to the thicker asphalt layer.

Another interesting finding is that the magnitudes of critical shear strain are greater than the ones of critical tensile strains at the same loading condition and pavement structure, especially for the thicker asphalt pavement. This indicates that the near-surface cracking potential is more critical than the bottom-up fatigue cracking for perpetual



pavement design. This inference is consistent with the field observations at the traffic testing of these pavement sections at the NAPTF. The thicker perpetual pavement test sections (LFP-1N and LFP-2N) showed no fatigue cracks, whereas the thinner section (LFP-3N) showed severe fatigue cracking. However, all the cracks were found to be top-down cracks instead of bottom-up cracks.

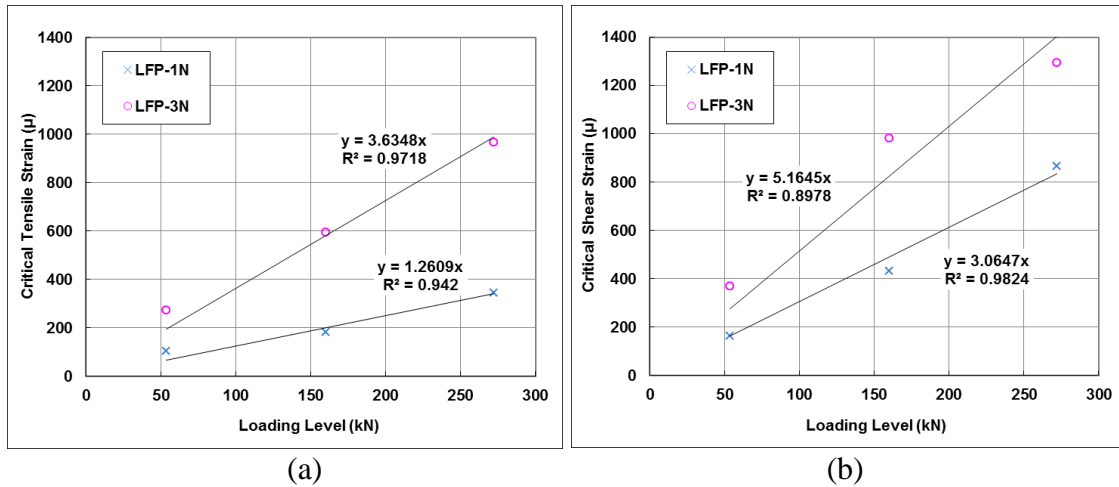


Figure 6.11 Effect of loading level on strain responses in asphalt layer: (a) critical tensile strains and (b) critical shear strains

### 6.2.5 Effect of Wheel Speed

The time histories of critical strains in the asphalt layer of LFP-3N section due to different moving speeds (0.5mph and 4mph) are shown in Figure 6.12. The loading magnitude on each wheel was 61.3kips and the average temperatures in the asphalt layer were 20°C. The results show that moving speeds have considerable effects on both tensile and shear strains. As the speed decreases from 4mph to 0.5mph, the critical tensile strain increases by 53% and the critical shear strain increases by 114%. Therefore, it concludes that the effects of moving speed have significant effect on fatigue cracking potential of airfield pavement even the aircraft is taxiing at low speeds.

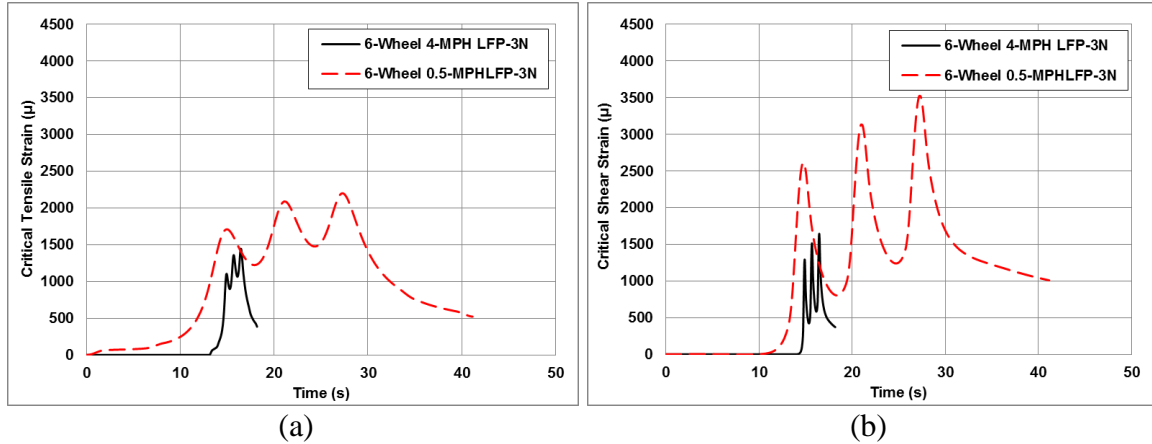


Figure 6.12 Time histories of critical (a) tensile strains at the bottom of asphalt layer and (b) shear strains at pavement near-surface at different moving speeds

## 6.3 Fatigue Life Analysis

### 6.3.1 Fatigue Models

To better understand the effect of multi-wheel loading on airfield pavement fatigue distress, several fatigue models were used and compared in this study. Currently, FAA has adopted strain-based fatigue model to correlate the number of coverages to the maximum horizontal tensile strain at the bottom of HMA layer. The strain-based fatigue model is shown in Equation 6-2 (Heukelom and Klomp 1962). According to FAARFIELD design program (FAA 2009), asphalt modulus was taken of 1380-MPa (200ksi) as default.

$$\log_{10}(C) = 2.68 - 5\log_{10}(\varepsilon_h) - 2.665\log_{10}(E_A) \quad (6-2)$$

Where,

$C$  is the number of coverages to failure;

$\varepsilon_h$  is the horizontal strain at the HMA layer bottom; and

$E_A$  is the HMA modulus (in psi).

The ratio of dissipated energy change (RDEC) has been studied by previous researchers for airport pavements (Carpenter and Jansen 1997; Ghuzlan and Carpenter

2000; Ghuzlan 2001). It introduced a more desirable expression of deterioration caused by the number of loading repetition. The RDEC was defined as the change of the dissipated energy between two hysteresis loops divided by the dissipated energy of previous loop. A Plateau Value (PV) was also defined as the RDEC value where the stiffness reduces to 50% and has a unique relationship with fatigue performance of AC layer. The PV was used to estimate fatigue life caused by aircraft loading wheels, as shown in Equation 6-3 to 6-6 (Shen and Carpenter 2007).

$$N_f = 0.4801PV^{-0.9007} \quad (6-3)$$

$$PV = 44.422\varepsilon_h^{5.14} \cdot S^{2.993} \cdot VP^{1.85} \cdot GP^{-0.4063} \quad (6-4)$$

$$VP = V_a / (V_a + V_b) \quad (6-5)$$

$$GP = (P_{NMS} - P_{PCS}) / P_{200} \quad (6-6)$$

Where,

$N_f$  is the number of cycles to fatigue failure;

$PV$  is the estimated plateau value of RDEC ;

$S$  is HMA flexural stiffness (psi), 871,296 psi here;

$\varepsilon_h$  is the horizontal strain at the bottom of HMA layer;

$V_a$  is air voids, 3.4% here;

$V_b$  is asphalt content by volume, 15.5% here;

$P_{NMS}$  is the percent of aggregate passing the nominal maximum size sieve, 95% here;

$P_{PCS}$  is the percent of aggregate passing the primary control sieve, 48% here;

$P_{200}$  is the percent of aggregate passing the #200 (0.075 mm), 5.3% here;

$VP$  is the volumetric parameter; and

$GP$  is the gradation parameter.

The dissipated energy density is determined as the area inside the stress-strain hysteresis loop. An energy loop area-based transfer function was employed to evaluate the performance of asphalt pavement at the FHWA Accelerated Loading Facility (Monismith et al. 1994). Tests were run in strain-controlled mode under continuous sinusoidal loading with no rest period. The final model related fatigue life ( $N_f$ ) to the initial dissipated energy per cycle. The initial dissipated energy density was defined as the area inside the hysteresis loop. This area can be calculated by means of the trapezoidal rule, as shown in Equation 6-7 (Ghuzlan and Carpenter 2000). Therefore, the third transfer function was introduced in terms of the area of the hysteresis loop of critical response, as shown in Equation 6-8 (Monismith et al. 1994).

$$\omega_0 = \pi \cdot \sigma_0 \cdot \varepsilon_0 \cdot \sin \phi_0 \quad (6-7)$$

$$N_f = 425.81 \omega_0^{-1.846} \quad (6-8)$$

Where,

$\sigma_0$  is the stress amplitude at initial load cycle;

$\varepsilon_0$  is the strain amplitude at initial load cycle;

$\phi_0$  is the phase angle between stress and strain wave signals;

$\omega_0$  is the initial dissipated energy density for critical tensile strain (in psi); and

$N_f$  is the number of cycles to fatigue failure.

### 6.3.2 Comparison of Calculated Fatigue Life

According to the fatigue models mentioned above, namely strain-based model, RDEC model, and dissipated energy model (DE), the fatigue life ( $N_f$ ) was calculated using the three models. Figure 6.13 shows the hysteresis loops of transverse strain (critical strain) at LFP-1N section under multi-wheel loading.

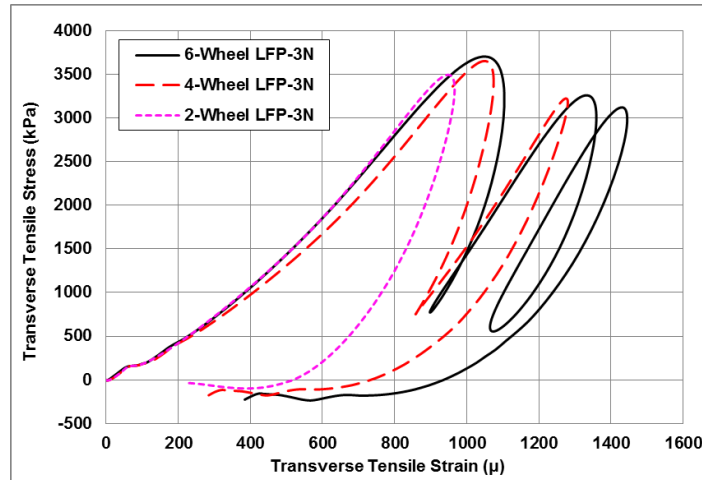


Figure 6.13 Hysteresis loops for the tensile strains under multi-wheel loading for the section of LFP-3N

Based on the results such as shown in Figure 6.13 for different sections along with variations of multi-wheel loading, the critical input variables from the three fatigue models were calculated from the reference parameters. The comparison is listed in Table 6.1 for different loading-section combinations. The loading level was used as 61.3 kips with moving speed of 4mph. It shows that the calculated input variables are increased as the number of multi-wheel loading increased or AC thicknesses were decreased. This describes a reduction in terms of the fatigue life.

Table 6.1 Comparison of Critical Input Variables for Fatigue Life

	Tensile Strain ( $\mu$ )	PV ( $\mu$ )	$\omega_0$ (psi)
LFP-1N; 2 wheels	685	8.5	0.07
LFP-1N; 4 wheels	1026	67.9	0.11
LFP-1N; 6 wheels	1235	176.1	0.17
LFP-3N; 2 wheels	966	49.9	0.14
LFP-3N; 4 wheels	1279	210.8	0.23
LFP-3N; 6 wheels	1445	394.6	0.35

The calculated numbers of coverages to failure by different fatigue models are shown in Table 6.2. As expected from Table 6.1, the fatigue life decreases as AC layer thickness decreased but increased as the number of loading wheels was decreased. Although the exact value of fatigue life was dependent on performance functions, the general trend of varying fatigue life with loading configurations or AC layer thickness was similar. It is noted that the fatigue life is calculated based on the default parameters in fatigue models, which have not been calibrated using performance data of airfield pavements.

Table 6.2 Performance Comparison of Calculated Fatigue Life

Loading Configuration	Fatigue Life ( $N_f$ ) based on		
	Strain	RDEC	DE
LFP-1N; 2 wheels	23676	17698	59570
LFP-1N; 4 wheels	3141	2727	25219
LFP-1N; 6 wheels	1243	1156	11258
LFP-3N; 2 wheels	4238	3599	17086
LFP-3N; 4 wheels	1043	983	6482
LFP-3N; 6 wheels	567	559	2889

Table 6.3 shows the percentage change of different scenarios as compared to the benchmark conditions. The results show that fatigue life decreases by 57.7-86.7% as the number of wheels increases from two to four, and 81.1-94.8% as the number of wheels increases from two to six on LFP-1N section (381-mm AC layer). Similarly, fatigue life decreases by 62.1-75.4% as the number of wheels increases from two to four, and 83.1-86.6% as the number of wheels increases from two to six on LFP-3N section (254-mm AC layer). This indicates that the multi-wheel effect on fatigue life is more significant for the thicker pavement. On the other hand, as AC layer thickness decreased from 381mm to 254mm, fatigue life reduced by 71.3-82.1% for two-wheel loading, but 54.4-74.3% for six-wheel loading. This indicates that the thickness effect on fatigue life at six-wheel loading is not as significant as the effect at two-wheel loading.

However, while the fatigue life was calculated based on the reference fatigue models, the simulated loading conditions lacked of consideration of the situation in realistic loading conditions. Different aircraft types possess different wheel loading configurations in the real case, including different wheel weights, tire pressure levels, and wandering patterns. Therefore, the fatigue life should be estimated from cumulative damage concept as used in FAARFIELD.

Table 6.3 Percentage Change of Calculated Fatigue Life

Effect	Comparison	Change of Fatigue Life ( $N_f$ ) based on		
		Strain	RDEC	DE
Loading Effect	LFP-1N 4-wheel vs. 2-wheel	-86.7%	-84.6%	-57.7%
	LFP-1N 6-wheel vs. 2-wheel	-94.8%	-93.5%	-81.1%
	LFP-3N 4-wheel vs. 2-wheel	-75.4%	-72.7%	-62.1%
	LFP-3N 6-wheel vs. 2-wheel	-86.6%	-84.5%	-83.1%
AC Thickness Effect	2-wheel 254mm vs. 381mm	-82.1%	-79.7%	-71.3%
	4-wheel 254mm vs. 381mm	-66.8%	-64.0%	-74.3%
	6-wheel 254mm vs. 381mm	-54.4%	-51.6%	-74.3%

## 6.4 Summary

In this chapter, the effect of multi-wheel loading gear configuration was investigated on the loading-induced cracking potential of airfield flexible pavements. Response testing was conducted in NAPTF by varying multi-wheel gear configurations. Tensile strains in the asphalt layer were measured by strain gauges. 3-D FE models were built to simulate multi-wheel loading effects along with non-uniform tire-pavement contact stresses. The 3-D FE models were validated by response testing results. The discrepancies of model results are within 5% of measurements in terms of peak strain magnitudes

Analysis results concluded that the six-wheel gear configuration caused the greater tensile strains at the bottom of asphalt layer and shear strains at pavement near-surface. The tensile and shear strains in the transverse direction were found greater than the ones in the longitudinal direction.

As asphalt layer thickness increases from 254mm to 381mm, the critical tensile strain decreases by 60% and the critical shear strain decreases by 30%.

The shear strain increases more rapidly as the load level increases as compared to the tensile strain; while the thinner asphalt layer is more sensitive to the loading level as compared to the thicker asphalt layer.

The magnitudes of critical shear strain are greater than the ones of critical tensile strains at the same loading condition and pavement structure, especially for the thicker asphalt pavement. The effects of moving speed have significant effect on fatigue cracking potential of airfield pavement even the aircraft is taxiing at low speeds.

Fatigue life of airfield pavement is analyzed using different fatigue models. The theoretical predictions vary depend on the response parameter used in the fatigue model, but they indicate the same trend for different wheel configurations and AC layer thicknesses.



## CHAPTER 7 CONCLUSIONS AND RECOMMENDATIONS

### 7.1 Conclusions

This dissertation aims to study the flexible pavement performance under Falling Weight Deflectometer (FWD) loading and moving vehicular loading. The axisymmetric finite element (FE) models were developed to simulate the circular FWD loading on pavement system and to capture the complexity in material properties, layer interfaces, and boundary conditions. The axisymmetric FE models were used to generate the synthetic database that covers the variations in material parameters, pavement structure, temperature, and loading levels. The ANN-GA backcalculating program can produce existing pavement condition after the training, verification, and validation by using the synthetic and field testing database. Moreover, this dissertation investigated the airfield flexible pavement responses under variations of aircraft loading in consideration of the realistic aircraft tire–pavement interaction. For the heavy aircraft and high tire pressure loading, the aircraft loading was simulated as moving wheels having uniform and non-uniform contact stress distributions. Various tire rolling conditions caused by aircraft ground maneuvering were simulated including free rolling, full-braking, and turning. For the multi-wheel aircraft loading, the 3-D FE models characterized loading gear configuration in terms of two-wheel, four-wheel, and six-wheel assembly. The pavement responses in the asphalt layer (tensile, compressive, and shear strains) under different loading conditions were calculated and analyzed in relation to different pavement failure mechanisms.

#### *7.1.1 Finite Element Modeling*

- (1) Parametric analysis emphasized the primary factors affecting calculated responses including dynamic analysis, temperature gradient, bedrock depth, asphalt layer delamination, viscoelasticity of asphalt layer, and nonlinearity of unbound materials.

- (2) In particular, the delamination in asphalt layer induces the greater strain responses; while neglecting bedrock effect overestimates surface deflections. These two factors were usually neglected in the previous analysis work.
- (3) The developed FE model successfully captures the distinctive constitutive model for each pavement layer and the interaction between different layers and boundary conditions.

#### *7.1.2 ANN-GA Program for Backcalculation*

- (1) The input variables of the ANN-GA program are available from FWD test including the peak deflections at different offsets, shape factors of hysteresis loop, layer thicknesses, loading magnitudes, and air and surface temperatures.
- (2) The predicted viscoelastic material parameters of asphalt surface layer were found having acceptable agreements with the measured data from LTPP sections.
- (3) The ANN-GA possesses some advantages over traditional iteration-based backcalculating program such as the elimination of seed moduli and consideration of complex material properties.
- (4) The ANN-GA program provides an effective approach in assessing structural capacity of existing pavement for the deterioration of viscoelastic AC and degradation of nonlinear unbound materials.
- (5) The deterioration condition of AC modulus was found consistent with fatigue cracking measured at pavement surface based on LTPP distress survey results. And the degradation of unbound material was validated by LTPP database.
- (6) The developed ANN-GA program can be successfully used to obtain damaged dynamic modulus of AC and evaluate *in situ* pavement condition from structural point of view.

### *7.1.3 Aircraft High Tire Pressure*

- (1) The non-uniform contact stress distribution induced greater critical tensile strains, shear strains and compressive strains in the asphalt layer, than both area-based and pressure-based uniform contact stress distributions.
- (2) Applying average temperature profile in summer is a conservative approach for predicting fatigue cracking potential; however, it underestimates rutting or near-surface cracking potential in the airfield pavement.
- (3) The increase of tire loading caused greater change of maximum strain responses compared to the increase of tire inflation pressure. The tire loading behaves as a predominant factor affecting airfield pavement service life.
- (4) The predicted rutting depth in the asphalt layer increase due to high tire pressure is greater than the one obtained from the full-scale test by means of the MEPDG performance functions.

### *7.1.4 Aircraft Ground Maneuvering*

- (1) Airfield pavement responses at the near-surface were affected by the non-uniform distributions of 3-D tire-pavement contact stresses that varied depending on different tire rolling conditions under aircraft ground maneuvering operations.
- (2) The multi-axial stress state criterion can effectively evaluate the shear failure potential at airfield asphalt pavements under the combined loading of normal stresses and shear stresses.
- (3) Aircraft braking or turning significantly increased the shear failure potential in the bulk material and at the asphalt layer interface due to the tangential stresses applied on pavement surface.
- (4) The cohesion strength of asphalt concrete played an important role in preventing shear failure because aircraft ground maneuvering causes significant amounts of tangential stresses applied on pavement surface that increases the shear stress at the small confinement.

### *7.1.5 Aircraft Multi-Wheel Loading*

- (1) The six-wheel gear configuration caused the greater tensile strains at the bottom of asphalt layer and shear strains at pavement near-surface. The tensile and shear strains in the transverse direction were found greater than the ones in the longitudinal direction.
- (2) The shear strain increases more rapidly as the load level increases as compared to the tensile strain; while the thinner asphalt layer is more sensitive to the loading level as compared to the thicker asphalt layer.
- (3) The magnitudes of critical shear strain are greater than the ones of critical tensile strains at the same loading condition and pavement structure, especially for the thicker asphalt pavement. The effects of moving speed have significant effect on fatigue cracking potential of airfield pavement even the aircraft is taxiing at low speeds.
- (4) Fatigue life of airfield pavements decreases significantly as the number of aircraft wheel increases or the AC layer thickness decreases.

## **7.2 Recommendations for Future Study**

The following recommendations are recommended for future study:

- (1) With the proper development of axisymmetric FE models, further research will be conducted for backcalculation of layer moduli for concrete pavement and composite pavement.
- (2) The backcalculated moduli of existing pavement layers from the ANN-GA program can be further used to design pavement overlay using mechanistic-empirical design principle.
- (3) A broader synthetic database should be incorporated into the training process to enhance the interpolating capability of the ANN-GA program. Future study on the ANN-GA program should focused on thick asphalt pavement or perpetual pavement in airfield.

- (4) Visco-plastic model should be utilized to predict rutting depth in the asphalt layer more accurately.
- (5) Appropriate laboratory test setup should be used to simulate in-situ pavement stress states under critical loading conditions for evaluation of shear failure potential, such as triaxial test or hollow cylinder test with confinements.
- (6) Future research should be conducted to analyze fatigue life of airfield pavement using calibrated fatigue models that can better consider the interaction of multi-wheel loading and the strain pulse with multiple peaks.

## REFERENCES

- ABAQUS. *ABAQUS/Standard User's Manual*, Version 6.7, Hibbitt, Karlsson & Sorenson, Inc., Pawtucket, RI, 2007.
- ABAQUS. *ABAQUS/Standard User's Manual*, Version 6.10, Hibbitt, Karlsson & Sorenson, Inc., Pawtucket, RI, 2010.
- Airbus, *High Tire Pressure Test*, Technical Report, 2010.
- Alkasawneh, W. *Backcalculation of Pavement Moduli Using Genetic Algorithms*. Ph.D. Dissertation, The University of Akron, 2007.
- Al-Qadi, I. L., and H. Wang. Prediction of Tire-Pavement Contact Stresses and Analysis of Asphalt Pavement Responses: A Decoupled Approach. *The Journal of the Association of Asphalt Paving Technologists*, Vol. 80, 2011, pp. 289–316.
- Al-Qadi, I. L., H. Wang, and E. Tutumluer. Dynamic Analysis of Thin Asphalt Pavements by Using Cross-Anisotropic Stress-Dependent Properties for Granular Layer. *Transportation Research Record*, No. 2154, TRB, National Research Council, Washington, D.C., 2010, pp. 156–163.
- Al-Qadi, I. L., M. A. Elseifi, P. J. Yoo, S. H. Dessouky, N. Gibson, T. Harman, J. D'Angelo, and K. Petros. Accuracy of Current Complex Modulus Selection Procedure from Vehicular Load Pulse: NCHRP Project 1-37A Mechanistic-Empirical Pavement Design Guide. In *Transportation Research Record: Journal of the Transportation Research Board*, No. 2087, TRB, National Research Council, Washington, D.C., 2008, pp. 81–90.
- Al-Qadi, I.L., H. Wang, and E. Tutumluer. Dynamic Analysis of Thin Asphalt Pavements by Using Cross-Anisotropic Stress-Dependent Properties for Granular Layer. In *Transportation Research Record: Journal of the Transportation Research Board*, No. 2154, TRB, National Research Council, Washington, DC, 2010, pp. 156-163.
- ARA, Inc. ERES Division. *Guide for Mechanistic-Empirical Design of New and Rehabilitated Pavement Structures*, NCHRP 1-37A Final Report, TRB, Washington, DC, 2004.

- ARA, Inc. ERES Division. *Guide for Mechanistic-Empirical Design of New and Rehabilitated Pavement Structures*. NCHRP 1-37A Final Report, TRB, Washington, D.C., 2004.
- ARA. *Guide for Mechanistic-Empirical Design of New and Rehabilitated Pavement Structures*. NCHRP 1-37A Final Report. ARA, Inc., ERES Consultants Division, Champaign, Ill., 2004.
- Asphalt Institute. *Research and Development of the Asphalt Institute's Thickness Design Manual* (MS-1). Research report 82-1, 9th ed., College Park, Md, 1982.
- Bathe, K.J. *Finite Element Procedures in Engineering Analysis*, Prentice-Hall, NJ, 1982.
- Boeing. *Airplane Characteristics for Airport Planning*. The Boeing Company, 2013.
- Bognacki, C. J., A. Frisvold, T. Bennert. Investigation of Asphalt Pavement Slippage Failures on Runway 4r-22l, Newark International Airport. *Proceedings of International Conference on Highway Pavements and Airfield Technology 2017*, Philadelphia, PA, 2007.
- Brill, D. R. and I. Kawa. Advances in FAA Pavement Thickness Design Software: FAARFIELD 1.41. *Proceedings of 2007 FAA Worldwide Airport Technology Transfer Conference* (in CD), Atlantic City, NJ, 2007.
- BROUTIN, M. *Assessment of flexible airfield pavements using Heavy Weight Deflectometers*. Ph.D. Dissertation, LCPC Paris, 2010.
- Canestrari, F., G. Ferrott, M. N. Partl, and E. Santagata. Advanced Testing and Characterization of Interlayer Shear Resistance. In *Transportation Research Record*, No. 1929, Transportation Research Board of the National Academies, Washington, D.C., 2005, pp. 69-78.
- Ceylan, H., K. Gopalakrishnan, and A. Guclu. Advanced Approaches to Characterizing Nonlinear Pavement System Responses. In *Transportation Research Record: Journal of the Transportation Research Board*, No. 2005, TRB, National Research Council, Washington, D.C., 2007, pp. 86-94.
- Chatti, K., M.E. Kutay, N. Lajnef, I. Zaabar, S. Varma, and H.S. Lee. *Enhanced Analysis of Falling Weight Deflectometer Data for Use with Mechanistic-Empirical Flexible*

- Pavement Design and Analysis and Recommendations for Improvements to Falling Weight Deflectometer*, Final Report to FHWA, Washington, DC, 20590, 2003.
- Chen, J., and H. Wang, M. Li, and L. Li. Evaluation of pavement responses and performance with thermal modified asphalt mixture. *Materials & Design*, Volume 111, 2016., pp. 88-97.
- Chou, Y.T., and H.G. Larew. Stresses and Displacements in Viscoelastic Pavement Systems under a Moving Load. *Highway Research Record*, No. 282, HRB, Washington, D.C., 1969, pp. 24-40.
- Cook, K., N. Garg, A. Singh, and M. Flynn. Detection of Delamination in the HMA Layer of Runway Pavement Structure Using Asphalt Strain Gauges. *Journal of Transportation Engineering*, Volume 142, Issue 11, 2016.
- Cunliffe, C., Y. Mehta, D. Cleary, A. Alo, and T. Redles. Impact of dynamic loading on backcalculated stiffness of rigid airfield pavements. *International Journal of Pavement Engineering*, Vol. 17, Issue 6, 2016, pp 489-502.
- Dai, S. and J. Zollars. Resilient Modulus of Minnesota Road Research Project Subgrade Soil. *Transportation Research Record*, No. 1786, TRB, National Research Council, Washington, D.C., 2002, pp. 20-28.
- Daugherty, R. H. *A Study of the Mechanical Properties of Modern Radial Aircraft Tires*. NASA Langley Research Center, 2003.
- De Beer, M. C., C. Fisher and F. J. Jooste. Determination of Pneumatic Tire pavement Interface Contact Stresses Under Moving Loads and Some Effects on Pavements with Thin Asphalt Surfacing Layers. *Proceedings of 8th International Conference on Asphalt Pavements (Volume I)*, Seattle, Washington, 1997, pp 179-227.
- Deacon, J., J. Harvey, I. Guada, L. Pospescu, and C. Monismith. Analytically based approach to rutting prediction. In *Transportation Research Record: Journal of the Transportation Research Board*, No. 1806, TRB, National Research Council, Washington, D.C., 2002, pp. 9–18.
- Dowling, N.E. *Mechanical Behavior of Materials*, 2nd ed., Prentice Hall, Upper Saddle River, NJ, 1999.



- Fabre, C., J.M. Balay, and P. Lerat. Full-Scale Aircraft Tire Pressure Tests. *Proceedings of 2010 FAA Worldwide Airport Technology Transfer Conference* (in CD), Atlantic City, NJ, 2010.
- FAA. Airport Design, *Advisory Circular 150/5320-10F*, Federal Aviation Administration, Washington, D.C., 2013.
- FAA. Airport Design, *Advisory Circular 150/5300-13A*, Federal Aviation Administration, Washington, D.C., 2012.
- FAA. Airport Pavement Design and Evaluation, *Advisory Circular 150/5320-6E*, Federal Aviation Administration, Washington, D.C., 2009.
- FAA. Airport Pavement Design and Evaluation, *Advisory Circular 150/5370-10G*, Federal Aviation Administration, Washington, D.C., 2014.
- FAA. Airport Pavement Design and Evaluation, *Advisory Circular 150/6320-6F*, Federal Aviation Administration, Washington, D.C., 2016.
- FAA. FAA Airport Technology Research & Development Branch Home Page. FAA William J. Hughes Technical Center, Atlantic City Intl. Airport, New Jersey. <http://www.airporttech.tc.faa.gov>, 2015.
- Ferry J. D. *Viscoelastic Properties of Polymers*. John Wiley & Sons, Hoboken, N.J., 1980.
- FHWA. LTPP InfoPave. <https://infopave.fhwa.dot.gov/>, 2016.
- FHWA. *Temperature Predictions and Adjustment Factors for Asphalt Pavement*, No. FHWA-RD-98-085, Final Report to Federal Highway Administration (FHWA), McLean, VA, 2000.
- Fwa, T.F., C.Y. Tan, and W.T. Chan. Backcalculation Analysis of Pavement-Layer Moduli Using Genetic Algorithms. In *Transportation Research Record: Journal of the Transportation Research Board*, No. 1570, TRB, National Research Council, Washington, D.C., 1997, pp. 134–142.
- Garcia, G. and M. R. Thompson. Strain and Pulse Duration Considerations for Extended-Life Hot-Mix Asphalt Pavement Design. *Transportation Research Record*, No. 2087, TRB, National Research Council, Washington, D.C., 2008, pp. 3–11.

- Garg, N. *Post-traffic Testing at the National Airport Pavement Test Facility: Test Item MFC*, Technical Note, DOT/FAA/AR-TN01/49, Federal Aviation Administration, Washington, D.C., 2001.
- Garg, N., and G. F. Hayhoe. Asphalt Concrete Strain Responses at High Loads and Low Speeds at the National Airport Pavement Test Facility. *Proceedings, ASCE Airfield Pavement Specialty Conference – Advancing Airfield Pavements*, Chicago, 2001.
- Garg, N., J. Bilodeau, and G. Dore. Experimental Study of Asphalt Concrete Strain Distribution in Flexible Pavements at The National Airport Pavement Test Facility. *Proceedings of 2014 FAA Worldwide Airport Technology Transfer Conference* (in CD), Atlantic City, NJ, 2014.
- Garg, N., E. Tutumluer, and M. R. Thompson. Structural Modeling Concepts for the Design of Airport Pavements for Heavy Aircraft. *Proceedings, Fifth International Conference on the Bearing Capacity of Roads and Airfields*, Trondheim, Norway, 1998.
- Garg, N., Q. Li, and M. Haggag. High Aircraft Tire Pressure Effects on HMA Airfield Pavements. *8th RILEM International Symposium on Testing and Characterization of Sustainable and Innovative Bituminous Materials*, Ancona, Italy, 2015, pp. 825-836.
- Gedafa, D.S., M.Hossain, and S.A. Romanoschi. Prediction of Asphalt Pavement Temperature. *Proceedings Airfield and Highway Pavement*, Los Angeles, CA, 2013, pp. 373-382.
- George, K.P. *Prediction of Resilient Modulus from Soil Index Properties*, Final Report to Federal Highway Administration, Mississippi Department of Transportation Research Division, Jackson MS, 2004.
- Ghuzlan, K. *Fatigue Damage Analysis in Asphalt Concrete Mixtures Based Upon Dissipated Energy Concepts*, Ph.D. Thesis, University of Illinois at Urbana-Champaign, Urbana, IL, 2001.
- Carpenter, S. H., and M. Jansen. Fatigue Behavior under New Aircraft Loading Conditions, *Proceedings of Aircraft Pavement Technology in the Midst of Change*, Seattle, Washington, United States, 1997.

- Ghuzlan, K.A. and S.H. Carpenter. Energy-Derived, Damage-Based Failure Criterion for Fatigue Testing. In *Transportation Research Record: Journal of the Transportation Research Board*, No. 1723, TRB, National Research Council, Washington, DC, 2000, pp. 141-149.
- Goldberg, D.E. *Genetic algorithms in search, optimization, and machine learning*. Reading, MA: Addison-Wesley Pub. Co., 1989.
- Gokhale, S., D. Anderson, D. Christensen, and R. Bonaquist. Simplified Protocol for Triaxial Testing of Hot-Mix Asphalt Concrete. *Journal of the Association of Asphalt Paving Technologists*, Vol. 74E, 2005.
- Gomez-Ramirez, F.M. and M.R. Thompson. *Characterizing aircraft multiple wheel load interaction for airport flexible pavement design, Civil Engineering Studies*, COE Report, Center of Excellence for Airport Technology, University of Illinois at Urbana-Champaign, Urbana, IL, 2002.
- Gopalakrishnan, K., S. Kim, H. Ceylan, and O. Kaya. *Development of Asphalt Dynamic Modulus Master Curve Using Falling Weight Deflectometer Measurements*, Final Report to Iowa Highway Research Board, Iowa Department of Transportation, 800 Lincoln Way, Ames, IA 50010, 2014.
- Hajj, E.Y., R. V. Siddharthan, P. E. Sebaaly, and D. Weitzel. Hot-Mix Asphalt Mixtures for Nevada's Intersections. In *Transportation Research Record*, No. 2001, TRB, Washington, D.C., 2007, pp. 73-83.
- Hakim, B.A., L.W. Cheung, and R.J. Armitage. Use of FWD Data for Prediction of Bonding between Pavement Layers. *International Journal of Pavement Engineering*, Vol. 1(1), 2000, pp.49-59.
- Hammoum, F., A. Chabot, D. St-Laurent, H. Chollet, and B. Vulturescu. Effects of Accelerating and Decelerating Tramway Loads on Bituminous Pavement. *Materials and Structures*, Volume 43, Issue 9, 2009, pp. 1257-1269.
- Hayhoe, G.F. and N. Garg. Subgrade Strains Measured in Full-scale Traffic Tests with Four- and Six-wheel Landing Gears. *Proceedings of 2002 FAA Worldwide Airport Technology Transfer Conference* (in CD), Atlantic City, NJ, 2002.

- Heukelom, W. and A. J. G. Klomp. Dynamic Testing as a Means of Controlling Pavements During and After Construction, *Proceedings of International Conference on the Structural Design of Asphalt Pavements*, Ann Arbor, Michigan, United States, 1962.
- Howell, W. E., S. E. Perez, and W. A. Vogler. Aircraft Tire Footprint Forces. *ASTM Special Technical Publication (SPT) 929*, 1986, pp. 110-124.
- Huang, Y.H. *Pavement Analysis and Design*, 1st ed., Prentice Hall, Upper Saddle River, NJ, 1993.
- Hu, X., F. Zhou, and L.F. Walubita. Proposed Loading Waveforms and Loading Time Equations for Mechanistic-Empirical Pavement Design and Analysis. *Journal of Transportation Engineering*, Vol. 136, No. 6, 2010, pp. 518–527.
- Huber, G.A. Strategic Highway Research Program Report SHRP-A-648A: *Weather Database for the Superpave® Mix Design System*, Transportation Research Board, Washington, DC, 1994.
- ICAO. *Aerodrome Design Manual, Part 3, Pavements*, 2nd edition. Document 9157-AN/901, International Civil Aviation Organization, 1983.
- Jones, J.P., W.G. Stamper, A. Godiwalla, J. Hall, and D. Little. Rehabilitation George Bush International Airport, Houston, Texas. *Asset Manage*, Volume 99, 2013, pp. 42-49.
- Jordan, R., M. A. Ishutkina, and T. G. Reynolds. *A Statistical Learning Approach to the Modeling of Aircraft Taxi-Time*. Technical Paper to FAA, MIT Lincoln Laboratory, Lexington, MA, 2010.
- Khoury, N. N., and M. M. Zaman. Effect of Wet-Dry Cycles on Resilient Modulus of Class C Coal Fly Ash–Stabilized Aggregate Base. *Transportation Research Record*, No. 1787, TRB, National Research Council, Washington, D.C., 2002, pp. 13–21.
- Kim, I. T, and, E. Tutumluer. Predicting Rutting Performance of Pavement Granular Layers at the FAA’s National Airport Pavement Test Facility, *Proceeding of 2004 FAA Worldwide Airport Technology Transfer Conference*, Atlantic City, NJ, 2004.

- Kim, M., E. Tutumluer, and J. Kwon. Nonlinear Pavement Foundation Modeling for Three-Dimensional Finite-Element Analysis of Flexible Pavements. *International Journal of Geomechanics*, Vol. 9, No. 5, ASCE, 2009, pp. 195-208.
- Kim, M., E. Tutumluer, and J. Kwon. Nonlinear Pavement Foundation Modeling for Three-Dimensional Finite-Element Analysis of Flexible Pavements. *International Journal of Geomechanics*, Vol. 9, No. 5, ASCE, 2009, pp. 195-208.
- Kim, S., D. N. Little, E. Masad, and R. L. Lytton. Estimation of Level of Anisotropy in Unbound Granular Layers Considering Aggregate Physical Properties. *International Journal of Pavement Engineering*, Vol. 6, No. 4, 2005, pp. 217-227.
- Kim, Y.R., B. Underwood, M.S. Far, N. Jackson, and J. Puccinelli. *LTPP Computed Parameter: Dynamic Modulus*. McLean, VA: FHWA, FHWA-HRT-10-035 Final Report, 2011.
- Kwon, J. *Development of a Mechanistic Model for Geogrid Reinforced Flexible Pavements*. Ph.D. Dissertation, University of Illinois at Urbana-Champaign, 2007.
- Leahy, R. B. *Permanent Deformation Characteristics of Asphalt Concrete*. Ph.D. Dissertation. University of Maryland, College Park, MD, 1989.
- Lee, Y., Y. Kim, and S. Ranjithan. Dynamic Analysis-Based Approach To Determine Flexible Pavement Layer Moduli Using Deflection Basin Parameters. In *Transportation Research Record: Journal of the Transportation Research Board*, No. 1639, TRB, National Research Council, Washington, D.C., 1998, pp. 36-42.
- Leiva-Villacorta, F., D.H. Timm. Falling Weight Deflectometer Loading Pulse Duration and Its Effect on Predicted Pavement Responses. *TRB 92nd Annual Meeting Compendium of Papers*, National Research Council, Washington, D.C., 2013.
- Li, M. and H. Wang. Development of ANN-GA Program for Backcalculation of Pavement Moduli under FWD Testing with Viscoelastic and Nonlinear Parameters. *International Journal of Pavement Engineering*, Vol. 20, Issue 4, 2017, pp. 490-498.
- Li, M., H. Wang, G. Xu, and P. Xie. Finite Element Modeling and Parametric Analysis of Viscoelastic and Nonlinear Pavement Responses under Dynamic FWD Loading. *Construction and Building Materials*, Vol. 141, 2017, pp. 23-35.

- Li, Q., C. Cary, S. Combs, and N. Garg. Evaluation of Asphalt Concrete Layer Response Using Asphalt Strain Gauges and Fiber Optic Strain Gauges. *Proceedings of International Conference on Transportation and Development*, Houston, TX, 2016.
- Losa, M., R. Bacci, and P. Leandri. A Statistical Model for Prediction of Critical Strains in Pavements from Deflection Measurements. *Road Materials and Pavement Design*, Vol. 9, Sup. 1, 2008. pp. 373-396.
- Loulizi, A., I.L. Al-Qadi, S. Lahouar, and T.E. Freeman. Measurement of Vertical Compressive Stress Pulse in Flexible Pavements: Representation for Dynamic Loading Tests. *Transportation Research Record*, No. 1816, TRB, National Research Council, Washington, D.C., 2002. pp. 125–136.
- Lu, Y, P.J. Wright, and Y. Zhou. Effect of Temperature and Temperature Gradient on Asphalt Pavement Response. *Road & Transport Research: A Journal of Australian and New Zealand Research and Practice*, Vol. 18, No. 1, 2009, pp.19-30.
- Masad, S., D. Little, and E. Masad. Analysis of Flexible Pavement Response and Performance Using Isotropic and Anisotropic Material Properties. *Journal of Transportation Engineering*, Vol. 132, No. 4, ASCE, 2006, pp. 342-349.
- Mateos, A. and M.B. Snyder. Validation of Flexible Pavement Structural Response Models with Data from the Minnesota Road Research Project. In *Transportation Research Record: Journal of the Transportation Research Board*, No. 1806, TRB, National Research Council, Washington, D.C., 2002, pp. 19-29.
- Mehta, Y. Determine Viscoelastic Mechanical Properties of Warm Mix Asphalt (WMA)-Reclaimed Asphalt Pavement (RAP) Mixes under High Stresses in Airfield Flexible Pavements and Its Impacts on Design Life. *Proceedings of Transportation Research Board*, Washington, DC, 2015.
- Meier, R.W. *Backcalculation of Flexible Pavement Moduli from Falling Weight Deflectometer Data Using Artificial Neural Networks*. Final Report to U.S. Army Corps of Engineers, U.S. Army Corps of Engineers Waterways Experiment Station 3909 Halls Ferry Road Vicksburg, MS, 1995.

- Mera, F. *Dynamic Nondestructive Testing of Pavement*. Geotechnical Engineering Report GR95-4, Geotechnical Engineering Center, University of Texas at Austin, Austin, Texas, 1995.
- Mohammad, L. N., M. A. Elseifi, A. Bae, N. Patel, J. Button, and J. A. Scherocman. *Optimization of Tack Coat for HMA Placement*, NCHRP Report 712, Transportation Research Board of the National Academies, Washington, D.C., 2012.
- Mohammad, L., B. Huang, A. Puppala, and A. Allen. Regression Model for Resilient Modulus of Subgrade Soils. *Transportation Research Record*, No. 1442, TRB, National Research Council, Washington, D.C., 1999, pp. 47-54.
- Molenaar, A. A. A. and A. A. van Niekerk. Effects of Gradation, Composition, and Degree of Compaction on the Mechanical Characteristics of Recycled Unbound Materials. *Transportation Research Record*, No. 1787, TRB, National Research Council, Washington, D.C., 2002, pp. 73–82.
- Monismith, C. L. *Fatigue Response of Asphalt-Aggregate Mixes*. Strategic Highway Research Program, Project A-404, National Research Council, 1994
- Monismith, C. L., J. A. Deacon, and J. T. Harvey. *Westrack: Performance Models for Permanent Deformation and Fatigue*. Final Report to Nichols Consulting Engineers, Pavement Research Center Institute of Transportation Studies University of California, Berkeley, 2000.
- Mooren, F., M. Stet, and P. Hopman. Tire Induced Surface Cracking Due To Extreme Wheel Loads. *Proceedings of 2014 FAA Worldwide Airport Technology Transfer Conference* (in CD), Galloway, NJ, 2014.
- Mun, S. and Y.R. Kim. Backcalculation Of Subgrade Stiffness Under Rubblised Pcc Slabs Using Multilevel FWD Loads. *International Journal of Pavement Engineering*, Vol. 10, 2009, pp.9-18.
- Nazarian, S. and M. Mazari. *Modulus-Based Construction Specification for Compaction of Earthwork and Unbound Aggregate: Appendices*, Final Report Submitted to NCHRP 10-84, Transportation Research Board, 2014.

- Park, D.Y, N. Buch, and K. Chatti. Effective Layer Temperature Prediction Model and Temperature Correction via Falling-Weight Deflectometer Deflections. *Transportation Research Record*, No. 1764, TRB, National Research Council, Washington, DC, 2001. pp. 97-111.
- Park, H.M., Y.R. Kim, and S.W. Park. Assessment of Pavement Layer Condition with Use of Multiload-Level Falling Weight Deflectometer Deflections. In *Transportation Research Record*, No. 1905, TRB, National Research Council, Washington, D.C., 2005, pp. 107-116.
- Park, S. and R. L. Lytton. Effect of Stress-Dependent Modulus and Poisson's Ratio on Structural Responses in Thin Asphalt Pavements. *Journal of Transportation Engineering*, Vol. 130, No. 3, ASCE, 2004, pp. 387-394.
- Park, S.W. and R.A. Schapery. Methods of interconversion between linear viscoelastic material functions. Part I-a numerical method based on Prony series. *International Journal of Solids and Structures*, Vol. 36, 1999, pp.1653-1675.
- Park, S. W. and Y. R. Kim. Interconversion between Relaxation Modulus and Creep Compliance for Viscoelastic Solids. *Journal of Materials in Civil Engineering*, Vol. 11, No. 1, 1999, pp. 76–82.
- Qin, J.F. *Predicting Flexible Pavement Structural Responses Using Falling Weight Deflectometer Deflection*. Master Thesis, Ohio University, 2010.
- Roginski, M.J. Effects of Aircraft Tire Pressures on Flexible Pavement. *Proceedings of the International Conference on Advanced Characterization of Pavement and Soil Engineering*, Athens, Greece, 2007, pp 1473-1481.
- Rolland, E. Tire Pressure Test Effect on Pavement. *Airbus High Tire Pressure Workshop* (in CD), Toulouse, France, 2009.
- Romanoschi, S. A., and J.B. Metcalf. Characterization of Asphalt Concrete Layer Interfaces. *Transportation Research Record*, No. 1778, Transportation Research Board of the National Academies, Washington, D.C., 2001, pp. 123-131.



- Romanoschi, S.A. and J.B. Metcalf. Effects of Interface Condition and Horizontal Wheel Loads on the Life of Flexible Pavement Structures. *Transportation Research Record*, No. 1778, TRB, National Research Council, Washington D.C., 2001, pp. 123-131.
- Salem, H. M., F. M. Bayomy, M. G. Al-Taher, and I. H. Genc. Using Long-Term Pavement Performance Data to Predict Seasonal Variation in Asphalt Concrete Modulus. In *Transportation Research Record: Journal of the Transportation Research Board*, No. 1896, TRB, National Research Council, Washington, D.C., 2004, pp. 119-128.
- Santha, B. L. Resilient Modulus of Subgrade Soils: Comparison of Two Constitutive Equations. *Transportation Research Record*, No. 1462, TRB, National Research Council, Washington, D.C., 1994, pp. 79-90.
- Schwartz, C. W. Effect of Stress-Dependent Base Layer on the Superposition of Flexible Pavement Solutions. *International Journal of Geomechanics*, Vol. 2, No. 3, ASCE, 2002, pp. 331-352.
- Shen, S. and T. Carpenter. Development of an Asphalt Fatigue Model Based on Energy Principles, *Journal of the Association of Asphalt Paving Technologists: from the Proceedings of the Technical Sessions*, Vol. 76, 2007, pp. 525-573.
- Shoukry, S.N., D.R. Martinelli, and O.I. Selezneva. Dynamic Performance of Composite Pavements Under Impact. In *Transportation Research Record: Journal of the Transportation Research Board*, No. 1570, TRB, National Research Council, Washington, D.C., 1997, pp. 163-171.
- Song, I. *Full-Scale High Tire Pressure Tests on Heated Pavement*. Report to ICAO, FAA Airport Technology Research and Development Team, 2010.
- Song, J. and T. Pellinen. *Dilation Behavior of Hot Mix asphalt under triaxial loading-Mechanism of permanent deformation generation*, Road Materials and Pavement Design, Vol. 8, No. 1, 2007, pp. 103-125.
- Tarefder, R.A., M.U. Ahmed, M.R. Islam, and M.T. Rahman. Finite Element Model of Pavement Response under Load Considering Cross-Anisotropy in Unbound Layers. *Advances in Civil Engineering Materials*, Vol. 3. No. 1, ASTM Int'l, 2014, pp. 57-75.

- Theyse, H. L., M. De Beer, and F. C. Rust. Overview of the South African Mechanistic Pavement Design Analysis Method. *Transportation Research Record*, No. 1539, TRB, National Research Council, Washington, D.C., 1996, pp. 6-17.
- Thompson, M.R., and N. Garg. *Wheel Load Interaction: Critical Airport Pavement Responses*, Technical Report COE No. 7, Center of Excellence for Airport Pavement Research, Department of Civil and Environmental Engineering, University of Illinois at Urbana-Champaign, Urbana, Illinois, 1999.
- Tian, S., M. M. Zaman, and J. P. Laguros. Variation of Resilient Modulus of Aggregate Base and Its Influence on Pavement Performance. *Journal of Testing and Evaluation*, Vol. 26, No. 4, 1998. pp. 329-335.
- Tielking, J. T. *Tire/Pavement Pressure Distribution*. Final Report to Air Force Engineering and Service Center, Texas A&M University, 1989.
- Tielking, J. T., and M. A. Abraham. Measurement of Truck Tire Footprint Pressures. In *Transportation Research Record: Journal of the Transportation Research Board*, No. 1435, TRB, National Research Council, Washington, D.C., 1994, pp. 92-99.
- Tseng, K. and Lytton, R. Prediction of Permanent Deformation in Flexible Pavement Materials. *Implication of Aggregates in the Design, Construction, and Performance of Flexible Pavements*, ASTM STP 1016, ASTM, 1989, pp. 154-172.
- Tutumluer, E. and M.R. Thompson. Anisotropic Modeling of Granular Bases In Flexible Pavement. *Journal of the Transportation Research Board*, No. 1577, TRB, National Research Council, Washington, DC, 1997, pp. 18-26.
- Tutumluer, E. and T. Pan. Aggregate Morphology Affecting Strength and Permanent Deformation Behavior of Unbound Aggregate Materials. *Journal of Material in Civil Engineering*, Vol. 20, No. 9, ASCE, 2008, pp. 617-627.
- Tutumluer, E. *NCHRP Synthesis 445: Practices for Unbound Aggregate Pavement Layers*, TRB, National Research Council, Washington, D.C., 2013.
- Tutumluer, E., O. Pekcan, and J. Ghaboussi. *Nondestructive Pavement Evaluation Using Finite Element Analysis Based Soft Computing Models*, Final Report to USDOT

- Region V Regional University Transportation Center, 2700 Kent B-100, West Lafayette, IN 47906, 2009.
- Uddin, W. and S. Garza. 3D-FE Simulation Study of Structural Response Analysis for Pavement-Subgrade Systems Subjected to Dynamic Loads. *Proceedings Pavements and Materials*, Los Angeles, CA, 2010, pp. 170-181.
- Ullidtz, P. *Modeling Flexible Pavement Response and Performance*, Polyteknisk Forlag, Narayana Press. Gylling, Denmark, 1998.
- Uzan, J. Dynamic Linear Back Calculation of Pavement Material Properties. *Journal of Transportation Engineering*, Vol. 120, No.1, 1994.
- Varma, S. and E. Kutay. Backcalculation of Viscoelastic and Nonlinear Flexible Pavement Layer Properties from Falling Weight Deflections. *International Journal of Pavement Engineering*, Vol. 17, 2016, pp. 388-402.
- Vickers, T.K. The Rapid Runway Entry. *Airport Operations*, Volume 17, No. 3, 1991.
- Von Quintus, H. and B. Killingsworth. *Analyses Relating to Pavement Material Characterizations and Their Effects on Pavement Performance*. Final report to FAA, Mclean, VA 22101, 2012.
- Wang, H. *Analysis of Tire-Pavement Interaction and Pavement Responses using a Decoupled Modeling Approach*. Ph.D. Dissertation, University of Illinois at Urbana-Champaign, 2011.
- Wang, H. and I. L. Al-Qadi. Combined Effect of Moving Wheel Loading and Three-Dimensional Contact Stresses on Perpetual Pavement Responses. In *Transportation Research Record: Journal of the Transportation Research Board*, No. 2095, TRB, National Research Council, Washington, D.C., 2009, pp. 53–61.
- Wang, H. and I. L. Al-Qadi. Impact Quantification of Wide-Base Tire Loading on Secondary Road Flexible Pavements. *Journal of Transportation Engineering*, Vol. 137, No. 9, ASCE, 2011, pp. 630-639.
- Wang, H. and I. L. Al-Qadi. Importance of Nonlinear Anisotropic Modeling of Granular Base for Predicting Maximum Viscoelastic Pavement Responses under Moving

- Vehicular Loading. *Journal of Engineering Mechanics*, Vol. 139, No. 1, ASCE, 2013, pp. 29-38.
- Wang, H. and I.L. Al-Qadi. Impact Quantification of Wide-base Tire Loading on Secondary Road Flexible Pavements. *Journal of Transportation Engineering*, Vol. 137, No.9, ASCE, 2011, pp. 630-639.
- Wang, H. and I.L. Al-Qadi. Near-Surface Pavement Failure under Multiaxial Stress State in Thick Asphalt Pavement. In *Transportation Research Record*, No. 2154, Transportation Research Board of the National Academies, Washington, D.C., 2010, pp. 91-99.
- Wang, H. and I.L. Al-Qadi. The Importance of Nonlinear Anisotropic Modeling of Granular Base for Predicting Maximum Viscoelastic Pavement Responses under Moving Vehicular Loading. *Journal of Engineering Mechanics*, ASCE, Vol. 139, No. 1, 2013, pp. 29-38.
- Wang, H. and M. Li. Evaluation of Effects of Variations in Aggregate Base Layer Properties on Flexible Pavement Performance. In *Transportation Research Record: Journal of the Transportation Research Board*, No. 2524, TRB, National Research Council, Washington, D.C., 2015, pp. 119-129.
- Wang, H. and M. Li. Comparative Study of Asphalt Pavement Responses under FWD and Moving Vehicular Loading. *Journal of Transportation Engineering*, Vol. 142, Issue 12, 2016.
- Wang, H., and I. L. Al-Qadi. Impact Quantification of Wide-Base Tire Loading on Secondary Road Flexible Pavements. *Journal of Transportation Engineering*, 137(9), 2011, pp. 630–639.
- Wang, H., I.L. Al-Qadi, and I. Stanciulescu, Simulation of Tire-Pavement Interaction for Predicting Contact Stresses at Static and Rolling Conditions. *International Journal of Pavement Engineering*, Vol. 13, No.4, 2012, pp. 310-321.
- Wang, H., M. Li, and N. Garg. Airfield Flexible Pavement Responses under Heavy Aircraft and High Tire Pressure Loading. In *Transportation Research Record: Journal*

- of the Transportation Research Board*, No. 2501, TRB, National Research Council, Washington, D.C., 2015, pp. 31-39.
- Wang, H., M. Li., and N. Garg. Investigation of shear failure in airport asphalt pavements under aircraft ground manoeuvring. *Road Materials and Pavement Design*, Vol. 18, Issue 6, 2017, pp. 1288-1303.
- Wang, H., M. Li., and N. Garg. Simulation of NAPTF high tyre pressure tests with advanced finite element modeling. *Proceedings FAA Worldwide Airport Technology Transfer Conference*, Galloway, New Jersey, USA, 2014.
- Wang, H., N. Garg, and M. Li. Understanding airfield pavement responses under high tire pressure: full-scale testing and numerical modeling. *The Roles of Accelerated Pavement Testing in Pavement Sustainability*, Springer, Cham, 2016, pp. 539-553.
- Wang, H., M. Li., and N. Garg. Perpetual pavement responses under single and dual wheel aircraft gear loading. *Bearing Capacity of Roads, Railways and Airfields*, Taylor & Francis Group, 2017, pp. 1791-1798.
- Wang, H. and I.L. Al-Qadi, Evaluation of Surface-Related Pavement Damage due to Tire Braking. *Road Materials and Pavement Design*, Vol. 11, No. 1, 2010, pp. 101-122.
- Wang, H., S. Portas, M. Coni, and I. L. Al-Qadi. Three-Dimensional Finite Element Modeling of Instrumented Airport Runway Pavement Responses. In *Transportation Research Record: Journal of the Transportation Research Board*, No. 2367, TRB, National Research Council, Washington, D.C., 2013, pp. 76-83.
- WSDOT. EVERSERIES. [www.wsdot.wa.gov/Business/MaterialsLab](http://www.wsdot.wa.gov/Business/MaterialsLab), 2005.
- Xiao, Y. and E. Tutumluer. *Best Value Granular Material for Road Foundations*. Final report to Minnesota DOT, Minnesota DOT, Saint Paul, 2012.
- Xiao, Y., E. Tutumluer, and J. Siekmeier. Mechanistic–Empirical Evaluation of Aggregate Base and Granular Subbase Quality Affecting Flexible Pavement Performance in Minnesota. *Transportation Research Record*, No. 2227, TRB, National Research Council, Washington, D.C., 2011, pp. 97–106.
- Xiao, Y., E. Tutumluer, Y. Qian, and J. Siekmeier. Gradation Effects Influencing Mechanical Properties of Aggregate Base–Granular Subbase Materials in Minnesota.

- Transportation Research Record*, No. 2267, TRB, National Research Council, Washington, D.C., 2012, pp. 14–26.
- Xu, B., S.R. Ranjithan, and Y.R. Kim. New Condition Assessment Procedure for Asphalt Pavement Layers, Using Falling Weight Deflectometer Deflections. *Transportation Research Record*, No. 1806, TRB, National Research Council, Washington, D.C., 2002. pp. 57-69.
- Xu, Q. and J.A. Prozzi. Static versus viscoelastic wave propagation approach for simulating loading effects on flexible pavement structure. *Construction and Building Materials*, Vol. 53, 2013, pp. 584-595.
- Xu, Q., J. M. Ruiz, M. Moravec, and R. O. Rasmussen. Simulation of Unbound Material Resilient Modulus Effects on Mechanistic-Empirical Pavement Designs. *Materials and Structures*, Vol. 46, No. 7, 2013. pp. 1089-1100.
- Yau, A., and H. L. Von Quintus. Study of LTPP Laboratory Resilient Modulus Test Data and Response Characteristics. Report FHWA-RD-02-051. FHWA, U.S. Department of Transportation, 2002.
- Yau, A. and H.L. Von Quintus. Predicting Elastic Response Characteristics of Unbound Materials and Soils. *Transportation Research Record*, No. 1874, TRB, National Research Council, Washington, D.C., 2004, pp. 47-56.
- Yin, H, M. Solaimanian, T. Kumar, and S. Stoffels. The Effect of Loading Time on Flexible Pavement Dynamic Response: A Finite Element Analysis. *Mechanics of Time-Dependent Materials*, Vol. 11, No. 1, 2014, pp. 119–132.
- Yin, H. Full-scale test of thermally induced reflective cracking in airport pavements. *Road Materials and Pavement Design*, Vol. 16, No. 3-4, 2008, pp. 265–288.
- Zaabar, I., K. Chatti, H. Lee, and N. Lajnef. Backcalculation of asphalt concrete modulus master curve from field-measured falling weight reflectometer data: using a new time domain viscoelastic dynamic solution and genetic algorithm. *Transportation Research Record*, No. 2457. Washington, DC: TRB, National Research Council, 2014, pp. 80-92.

Zhong, X.Z., X. Zeng, and J.G. Rose. Shear Modulus and Damping Ratio of Rubber-modified Asphalt Mixes and Unsaturated Subgrade Soils. *Journal of Materials in Civil Engineering*, Vol. 14, No. 6, ASCE, 2002, pp. 496-502.